Toepassingen van geïntegreerde fotonische structuren
op membranen gefabriceerd door lokaal etsen van het siliciumsubstraat

Applications of Integrated Photonic Structures on Membranes Fabricated by Locally Etching the Silicon Substrate

Elewout Hallynck

Promotor: prof. dr. ir. P. Bienstman
Proefschrift ingediend tot het behalen van de graad van
Doctor in de Ingenieurswetenschappen: Fotonica

Vakgroep Informatietechnologie
Voorzitter: prof. dr. ir. D. De Zutter
Faculteit Ingenieurswetenschappen en Architectuur
Academiejaar 2012 - 2013

ISBN 978-90-8578-600-9
NUR 959
Wettelijk depot: D/2013/10.500/33

Promotor:

Prof. dr. ir. Peter Bienstman

Examencommissie:

Prof. dr. ir. Rik Van de Walle (voorzitter)	Universiteit Gent, ELIS
Prof. dr. ir. Peter Bienstman (promotor)	Universiteit Gent, INTEC
Prof. dr. ir. Wim Bogaerts	Universiteit Gent, INTEC
Dr. ir. Christophe Caucheteur	UMons, Electromagnetism and Telecommunications Department
Dr. ir. Paul Jacobs	Zelfstandig expert
Prof. dr. Nicolas Le Thomas	Universiteit Gent, INTEC
Prof. dr. ir. Jan Vanfleteren	Universiteit Gent, ELIS

Universiteit Gent
Faculteit Ingenieurswetenschappen en Architectuur

Vakgroep Informatietechnologie
Sint-Pietersnieuwstraat 41, B-9000 Gent, België

Tel.: +32-9-264.33.16
Fax.: +32-9-264.35.93

Dit werk kwam tot stand in het kader van een
aspirantenbeurs van imec.

Dankwoord

’t Is moeilijk bescheiden te blijven wanneer je zo goed bent als ik.
Bedankt, Elewout.

Tweede poging (op aandringen van Peter)

Δυσπραξίαν ἄειδε, θεὰ...

Samplebox Button *02-09-2011*

13:05 - 3 samples in 20% KOH 79°C
15:05 - samples nog steeds niet doorgeëtst
15:20 - Kristof komt online (waarschijnlijk net terug van lunch)
16:30 - samples te veel doorgeëtst

Het is maar één van de vele aantekeningen die het niet hebben gehaald in mijn notitieboekje wegens te gênant maar het toont perfect aan dat een doctoraat bezaaid is met plagen alsof de goden zelf er een stokje willen voor steken: of dat ene perfecte sample blaast plots uit je pincet weg, of er kent er weer eentje het verschil niet tussen aceton en water, of je maakt je opnieuw de bedenking dat je *manager* niet kan spellen met de letters van *professor*. Kort gezegd: een spelletje Scrabble met Aleksies De Vos kan minder frustrerend zijn. U kan bijgevolg begrijpen dat het werk dat hier nu voor u ligt geen staaltje toponderzoek is maar desalniettemin mooi in lijn ligt met wat soms het motto van onze groep lijkt te zijn: "Het kan altijd slechter".
Het zal u misschien verbazen maar Roel heeft ook zijn zwaktes en één daarvan is een expansiedrift die niet meer gezien is sinds Alexander De Grote (Roel laat zich echter niet zo gemakkelijk tegenhouden door de Indus) waardoor er binnenkort wel eens een VN-waarnemer in de groep zou kunnen geïnstalleerd worden. Ik ben benieuwd aan welke bureau ze die gaan zetten. Nadeel hiervan is dat het quasi onmogelijk is om iedereen binnen onze groep bij naam te kunnen noemen (ik heb er hem zelf ook nog op betrapt), laat staan goed te leren kennen. Voordeel hiervan is dat er, statistisch gezien, in zo'n grote groep mensen altijd wel leuke personen zitten waarmee je je kan amuseren in een aangename sfeer. Bijgevolg zijn er enkele personen die ik me toch nog enige tijd zal herinneren nadat ik straks de deuren van de Plateau achter mij heb toegetrokken en in sommige gevallen zelfs mensen waarvan ik denk dat ik ze na vandaag nog lange tijd zal zien. Benieuwd wat de tijd hiermee gaat aanvangen om het met de woorden van een vuile post-doc te zeggen. Kort gezegd, het minste dat ik kan zeggen over de voorbije 4 jaar is dat ze een impact hebben gehad die van mij ongetwijfeld een ander persoon heeft gemaakt; zowel op professioneel als persoonlijk vlak heb ik een boel herinneringen waar ik met een glimlach op kan terugkijken en die zijn grotendeels te danken aan de mensen in mijn omgeving.

Ik had eerst gedacht om een lijstje van de website te kopiëren waarbij iedereen kon controleren of ze er in voorkwamen maar helaas is Wout mij daar in voor geweest en bovendien zou het mijn reputatie allerminst eer aandoen. Ik had graag over iedereen kort iets geschreven maar daar kon ik de moed en inspiratie echter niet voor opbrengen dus ik heb mij beperkt tot enkelen. Een gewaagde keuze als je hoort wat voor een overschatte lading een dankwoord soms krijgt toebedeeld maar ik heb dus toch besloten het gladde ijs op te zoeken, in de wetenschap dat ik er waarschijnlijk toch minstens een keer met mijn klieken en mijn klakken door zal zakken. Maar vind je jezelf dus niet terug, vrees niet: de lijst is, in tegenstelling tot wat de lengte doet vermoeden, niet exhaustief dus afgezien van de noodzakelijke uitzondering op de regel die ik rijp acht voor de psychiatrie, is de kans heel groot dat ik je best wel nog OK vind. En in het slechtste geval kan ik het het best omschrijven met de woorden van de helaas reeds ter ziele gegane Kurt Cobain: “I need you around to remind me what not to become”. Mensen die zich desgevallend toch nog tekort voelen gedaan of enige bezwaren hebben nodig ik graag uit om voor een ander hol te gaan keffen. De toon is gezet: we kunnen beginnen. Omdat de ervaring mij geleerd heeft dat het gros van de mensen mijn mails niet volledig doorleest, heb ik er in dit geval allerminst een goed oog op. Ik ben zo vrij geweest om de persoon waarover een bepaald stuk gaat vetgedrukt te zetten zodat die gemakkelijk zijn of haar desbetreffend stuk kan terugvinden. Het is graag gedaan. Vámonos!

Vooreerst, de prominenten.

Roel, de officieuze leider van de onderzoeksgroep fotonica/datingbureau Baets. Ik weet nog goed hoe ik bij jou op gesprek kwam om te doctoreren. Je vroeg wat mijn motivatie was. Ik antwoordde dan eerlijk: “Het is hier wel een leuke groep en ik heb nog geen zin om in de industrie te gaan.”. Waarop ik als antwoord kreeg: “Dat zijn nu net de twee argumenten die ik niet wil horen. Je moet echt wel gedreven zijn door onderzoek. Denk er alleszins nog eens goed over na en laat dan iets weten.”. Eerlijk gezegd heb ik er verder niet meer over nagedacht en gewoon een paar dagen gewacht voor ik een mail stuurde om te zeggen dat ik echt wel zin had om te beginnen. Sorry daarvoor. Achteraf gezien heb ik geen spijt gehad van die beslissing (voor die ene keer dat mijn luiheid me geen windeieren legt) maar de eerlijkheid gebiedt mij te zeggen dat ik het in een andere groep waarschijnlijk zou opgegeven hebben na een bepaalde tijd. Dat ik toch ben blijven voortdoen in een groep die was zoals ze was, een vrije sfeer en een voedingsbodem voor vriendschap, is voor een groot stuk jouw verdienste denk ik. Enfin, bedankt daarvoor.
Dan is er mijn promotor, **Peter**. Eigenlijk zou een meer toepasselijk citaat in het begin van hoofdstuk 3 er een van jou moeten zijn: “Om het fabricagepro-

ces op punt te stellen zou ik op iets van een 3 maanden rekenen.". Daar heb je mij toch goed liggen gehad, hé? Potverdikke. Enfin, afgezien daarvan: het is waarschijnlijk al in menig doctoraat geschreven maar ik kon me echt geen betere promotor voorstellen (mede doordat de onderhandelingen met Günther zijn afgesprongen; Dries daarentegen heb ik zelf afgewezen hoewel hij dat altijd zal blijven ontkennen). Eerlijk gezegd heb ik je niet lang als mijn promotor of meerdere erkend maar ben ik je al gauw gaan beschouwen als die collega wiens handtekening ik nodig had voor de bestelbonnen. Waarmee ik wil zeggen: ik vond je een heel toegankelijk persoon en heb genoten van een heel gemoedelijke samenwerking. Je hebt me ook meer dan voldoende vrijheid gegeven om te stuiten op de zoveelste technologische landmijn in het niemandsland dat je de clean room noemt en je veilig gadeslaat vanuit je loopgraven in het Technicum. Tevens kon je er altijd begrip voor opbrengen dat ik mijn creativiteit liet botvieren op extra-curriculaire activiteiten zoals de vele afscheidscadeaus en de ePIXradio's . Bedankt om deze mooie tijd mogelijk te maken. Aan de andere kant is dat gebrek aan ontzag misschien wel een voedingsbodem geweest om al die vergaderingen met jou te missen.
Daniël, bedankt voor de koffietas.
Leden van de jury, proficiat en vooral bedankt voor het doorworstelen van dit werk (sommigen tot twee maal toe heb ik gehoord) en het stellen van kritische en gerichte vragen: **Rik**, bedankt om al die uren aanwezig te zijn op beide verdedigingen van een onderwerp dat niet echt in je eigen domein ligt (als alumnus van het bio-team weet ik hoe het voelt); dan is er **Wim**, die ik bedank om ~~geen~~ niet te veel woordspelingen te hebben gemaakt tijdens mijn verdediging; **Christophe** dank ik om zich in het hol van de leeuw te wagen; **Paul**, bedankt om het bio-aspect van de thesis eens op de rooster te leggen (met alle gevolgen vandien) en om op voorhand aan te tonen dat een druppel door een membraan trekken zo zot nog niet is; minitieuze narekening kwam er van **Nicolas**: laat het ons op afrondingsfouten houden; en tenslotte **Jan**, u weze bedankt om de technologische kant van de zaak wat te bediscussïeren.
In tegenstelling tot wat de eerste pagina van dit dankwoord doet vermoeden, kan je een doctoraat niet voltooien zonder de hulp van anderen. Vele handen en hersenen hebben geholpen maar ik licht er hier, *kwestie van het wat kort te houden*, enkele voorname uit: **Diedrik** is verantwoordelijk voor het leeuwendeel van hoofdstuk 6 (ik zorgde slechts voor de gaten, hij liet er zijn vezel op los; laten we deze zin als een vreemd soort hommage beschouwen) en zonder de designs van **Tom** (een man die tijdens een van zijn legendarische *rants* kan overkomen als de leeuw van Androclus die in een doornstruik is getuimeld) die toevallig op dezelfde chips stonden, zou dit doctoraat een nog triester boeltje geweest zijn. Advies uit externe hoek over fluïdica en die vervloekte oppervlaktespanning kwam er van **prof. Jan Vierendeels** waarvoor oprechte dank.

En dan is het tijd om mij te mengen onder het gepeupel: vooreerst is er de komische clean room-tandem Shahram en Stevan, waardig van een eigen televisieshow. Iemand waar ik net wat meer appreciatie kan voor opbrengen dan voor de gemiddelde fotonica-burger is **Stevan**, die ik cynischer heb weten te worden over de jaren en de bedenker is van termen als *tornado processing* en *master of disaster*. Hij kan het niet zo goed vinden met bepaalde Zwitsers (hij wou er eens een paar persoonlijk de nek gaan omwringen maar kreeg de reisaanvraag waarschijnlijk niet goedgekeurd door Dries) en trad een beetje op als de officieuze politie van de clean room. Ik moet zeggen dat mijn verbazing over de hoeveelheid kennis die jij kan tentoonspreiden, die misschien best omschreven kan worden als een vat der Danaïden qua algemene kennis (ik heb dus Grieks gestudeerd voor moest het u nog niet zijn opgevallen), nooit is geminderd en ik heb altijd geboeid kunnen luisteren naar wat je te vertellen had. Als er iemand weet wie er eerst was, de kip of het ei, dan zal jij het wel zijn.
Dan is er **Shahram** ofte de *Prince of Persia*, die mij geleerd heeft dat de vraag "how are you?" niet altijd een antwoord behoeft omdat hij je gewoon de tijd niet laat om er een te geven. Een ander persoon zou waarschijnlijk getrakteerd geweest zijn op een vernietigende blik wanneer Shahram, net toen het fout ging, vroeg "but why your processing didn't work?" maar zijn ontwapenende blik zorgt meteen voor een gevoel van zelfrelativering. "It happens" om het met zijn woorden te zeggen. Shahram, bye bye see you bye. Om het opnieuw met je eigen woorden te zeggen.
Een man die vaak zichtbaar te lijden had onder de onschuldige doch confronterende vragen van Shahram was **Den Tassaert**. Iemand die drijft op een vorm van cynisme waar Stevan zelfs voor terugdeinst en mislukte processing afreageert op deuren die zijn pad kruisen of een zoveelste offensief lanceert tegen zijn toetsenbord.
Thijs (*nee heb je; ja kun je vergeten*) **Spuesens**, iemand die op een serene manier gezelligheid bracht in de clean room, wil ik graag een hart onder de riem steken: bij mij heeft het ook lang geduurd eer mijn onderzoek min of meer gelukt is. De grafiek van die ene meting waarvan je denkt "mja, hier kan ik wel iets rond verzinnen" ziet er dan net wat mooier uit; de tegenslagen, die draag je echter voor de rest van je leven mee.
Liesbet, niet verlegen om af en toe eens te laat te komen of te vroeg te vertrekken (geen nood, Liesbet, je geheim is veilig bij mij) en altijd leuk om mee te kletsen aan de FIB en daarbuiten. Ik zal je natuurlijk altijd herinneren als mijn overbuur in de clean room bureaus en als iemand die het uitstekend volhield met mijn bij wijlen snedige opmerkingen.
Steven, een mobiele oase van rust in die helse fabriek van een clean room tot een machine het laat afweten waarna hij ze bestookt met vloeken waarbij de

grootste ketter naarstig notities aan het nemen zou zijn. Een Nestor (Grieks dus) qua processing hoewel hij er plezier in vindt om doctorandi (of mij toch) te zien knoeien: “Ik dacht wel dat het niet ging werken”. Ik heb je altijd wel een mysterieus iemand gevonden maar dat past uiteraard mooi bij je hobby van all-round artiest. Bedankt voor het schilderij trouwens.
Kasia, die ik altijd een beetje beschouwde als de moeder van alle processende doctorandi en ze ook van goedkope drank voorzag, was altijd bereid om suggesties te geven of een helpende hand te bieden. Zoals een student soms aan zijn moeder vraagt om een boekbespreking voor school te maken hielp ook Kasia als je even geen tijd had voor het zoveelste zijspoor.
De perfecte brug tussen clean room en Technicum wordt natuurlijk verzorgd door een duo dat een gecombineerd aantal uren in de clean room op hun actief heeft staan gelijk aan dat van een doctoraatsstudent halfweg de introductiedag: **Dries** & **Günther**, beide sympathieke kerels, hoewel de één al wat tactvoller is dan de ander.
Trouwens, nu ik toch over hoge omes bezig ben: ja, **Geert**, ik weet dat er appelsienen op overschot zijn in Spanje en dat die Oxfam fruitsapjes niet goed zijn voor het milieu maar ik wou gewoon op mijn gemak iets drinken om die droge saucissen van Sint-Jansvest door te spoelen. Dank u.
Als de wereld door Atlas wordt gedragen, rust het Technicum grotendeels op de schouders van de Ilses en Kristien. **Ilse Meersman**, die altijd bereid was om met een glimlach advies te geven zodat ik op optimale wijze de financiële spons die de universiteit is kon leegwringen. **Ilse Van Royen**, die de algemene administratie voor haar rekening nam en altijd te vinden was voor een leuke babbel. En dan, last but not least woman, **Kristien**, leverancier van computerhulp en -materiaal, no questions asked. Dan is er nog de mysterieuze **Mike** die mijn aaneenschakeling van vette hits en strakke beats zonder morren heeft aanhoord. Tenslotte wil ik **Peter Guns** en **Luc** bedanken voor hun handigheid en vooral waardevolle input en ervaring bij het betere freeswerk. Bedankt, ieder van jullie.
Nog te vinden in het Technicum is een zekere **Martin Fiers**, een man die zijn naam zeker en vast gestolen heeft. Mensen die zich verwachten aan een potige, Britse buitenwipper zullen verbaasd staan kijken als ze deze vrolijke spring-in-’t-veld zien dartelen door de gang. Naast Karel (over wie later meer), een van mijn bureaugenoten van het eerste uur (afgezien van enkele Chinezen) met wie ik heel fijne momenten heb beleefd.
Er is een bekende uitspraak dat we maar 20% van onze hersenen gebruiken; blijkbaar kan je dat niveau een beetje opkrikken door sloten geconcentreerde suikers naar binnen te kappen. Ik heb het hier natuurlijk over **Bart**. Hierdoor is hij in staat linken te leggen die een ander mens niet kan begrijpen, zelfs als hij ze uitlegt, waardoor het een beetje op het paranoïde af kan gaan. Kort samenge-

vat: het is altijd een beetje op eieren lopen in een gesprek met die man. Hoewel er soms onderhuidse steekspelen werden gevoerd en je er niet om verlegen was om af en toe eens een stok in het hoenderhok te smijten of altijd klaar stond met de spreekwoordelijke pek en veren, heb ik mij altijd wel goed geamuseerd met jou.
Yannick, alias *DJ Wheelie*, met wie ik tot driemaal toe de eer heb gehad om ePIXradio te hebben mogen presenteren, zal ik mij herinneren als iemand met de aandachtsspanne van een eekhoorn op speed maar vooral als iemand met wie ik ongelooflijk veel gelachen heb. Tevens is er voor hem en Bart ongetwijfeld een mooie job bij *The Sun* weggelegd. Jammer dat je van Mechelen bent.
Het geval **Dumon**. Voor de mensen die het genoegen nog niet hebben gekend om hem te ontmoeten: Pieter Dumon is de man die verantwoordelijk is voor het leveren van onze chips. Om één of andere reden, die ik maar aan jaloezie zal toeschrijven, heeft die man mij 4 jaar lang systematisch gesaboteerd (ik dacht eerst aan incompetentie maar het was té apert) door ofwel mijn wafer niet volledig door te etsen, er wat extra lagen op te smijten of hem gewoon in twee te breken. Wie weet was ik al klaar na 2 jaar? Het moet echter gezegd zijn dat de lange wachttijden het ideale excuus vormden om rustig in eerste versnelling voort te tuffen op de weg naar een doctoraat en de reden waarom ik enkele weken ben gestopt met op jou af te geven omdat er topoxide op mijn wafer lag was omdat ik er was achter gekomen dat ik het blijkbaar wel degelijk zelf besteld had. Best nog grappig achteraf.
Gunay: wordt door reeds bovengenoemde Bart ook wel eens het epitheton *stier van de Bosporus* toegedragen. Een ongelooflijk louche typ die je zelfs zijn geknipte teennagels zou proberen versjacheren. Te mijden als zakenpartner, te proberen als masseur.
Het moet geen geheim wezen dat ik het niet zo heb voor domme of naïeve mensen; daarom wens ik graag **Thomas** te vermelden omdat ik bewonder hoe hij er soms als Bambi uitziet die net ook zijn adoptiemoeder is verloren maar toch snel te kennen geeft dat ze niet met zijn voeten moeten spelen.
Voor het geval we een acuut gevoel van chauvinisme zouden doen opwellen voor ons kleine Belgenland wordt er een tegengewicht geleverd door **Aditya** die de grootste moeite moet opbrengen om te proberen begrijpen hoe we kunnen overleven op een broodje met wat toespijs dat, net zoals de rest van onze keuken, blijkbaar zo flets smaakt als een stapel krantenpapier. Hoewel er soms enig superioriteitsgevoel van hem uitstraalt ten opzichte van Westerlingen (inderdaad: de wereld op zijn kop) heeft hij een apart gevoel voor humor dat ik wel weet te appreciëren bij momenten.
Dan is er nog het Chinese spraakspervuur **Chen**. Ondanks het feit dat je soms wat tijd moet nemen om haar zinnen te analyseren, is het een vrolijke, sociale en hartelijke vrouw waarvan ik het jammer vind dat ze niet eerder in de groep

terecht is gekomen.
Een op zijn minst bizar persoon is **Nannicha**. Net wanneer je denkt in een goed blaadje te staan zegt ze iets als "I really hate you guys.". Maar, toegegeven, het is al een tijdje geleden dat ik dat gehoord heb en het overgrote deel van de tijd hebben we gewoon veel gelachen. Je zal die puppy-ogen moeten missen die je diep vanbinnen kunnen raken wanneer ik weer eens een situatie moet rechttrekken of je wil meekrijgen om iets te gaan drinken (wat uiteindelijk meestal toch op een sisser uitdraait).

Ik denk dat we ongeveer halfweg zijn...

The Departed.

Vooreerst zijn er twee ex-bureaugenoten met wie ik mij ook heel goed geamuseerd heb. Er is **Joost**, die onder meer bekend is omdat hij eens een spoor van bureaumateriaal heeft achtergelaten in de straten van Gent nadat hij moest lopen om zijn laatste trein te halen omdat *how, de laatsten* weer eens niet *de laatsten* was. Ik ga herhalen wat je zelf zei in je doctoraat: "Dat mountainbiken komt er heus wel nog eens van".
Met **Koen** heb ik ook leuke tijden beleefd, zowel op het werk als ernaast. Als iemand die veel belang hechtte aan het sociale aspect van de groep en vaak de trekker was om een te gaan drinken stond je altijd open om *de nieuwe*, waartoe ik ooit behoorde, op te nemen in de groep en het is ook dankzij jou dat ik uiteindelijk in mijn vaste bureau ben terecht gekomen. Tot ik er natuurlijk ben uitgegooid, 3 maanden voor het einde.
Iemand die mij ook nog steeds bijblijft (hoewel hij nog niet zo lang vertrokken is), is **Linghua**. Het is moeilijk te ontkennen dat er meestal wel sprake is van een niet te verwaarlozen cultuurkloof tussen Chinezen en ons. Het fijne aan Linghua was dat je die kloof altijd wel een beetje kon terugzien maar dat hij ook in staat was die soms te overstijgen.
Voorts is er nog grootmeester **Khai**, schier onverstaanbaar in de omgang maar een van de meest hilarische personen die ik ben tegengekomen in de groep. Het is misschien niet mooi om zeggen maar Khai kan je best omschrijven als een *klein klootzakske*: tijdens het badmintonnen probeert hij je de hele tijd te intimideren met wat lijkt op oorlogskreten en als je dan eens een fout maakt lacht hij je gewoon vierkant uit in je gezicht. Oprecht, dat wel.
Als laatste van de reeds lang heengegane is er **Lieven**. Een speciaal doch uiterst amusant karakter. Hoewel we maar een paar maanden tezamen in de groep hebben gezeten was de sfeer in het Technicum toch niet meer dezelfde zonder jouw gegiechel.

The League of Exclusieve Klootzakken.

De eindspurt zet ik in met twee vliegen in één klap: Wout&Marie®. **Wout** is iemand met wie ik een even grote afkeer voor Milow en Selah Sue deel (voor wie ze nog niet heeft horen zingen: denk aan een zeug met bronchitis) en is tevens de helft van de (binnenkort) succesvolle triphop-formatie *August and The Gun*. Een man die iedereen te vriend is en elk jaar een fikse dosis compassie opzij zet voor wanneer de lelijkste hond ter wereld weer wordt verkozen. En niet te vergeten, diegene die mij het literaire/grafische meesterwerk dat *Preacher* is heeft leren kennen.
Wie Wout zegt, zegt natuurlijk **Marie**, iemand die ik meer dan eens als reisgenote heb gehad en er mij vaak aan deed denken dat we uiteindelijk ook maar ambtenaren zijn. Zonder haar inspanningen zouden veel afscheidsfeestjes waarschijnlijk uitgedraaid zijn op "Ja, we waren echt wel iets leuks van plan maar ja... mask deadline enzo... kende da, Dumon weer hé... allez... dag hé...". Tevens heeft ze over de meeste zaken wel een gefundeerde mening en ze kan soms overkomen als een harde tante maar dat neemt niet dat er in de woonst die Wout in haar hart heeft nog plaats is voor anderen (in de bezemkast weliswaar).
Ja, **Karel**, die moet ik wel vermelden gezien hij mij ook heeft vermeld in zijn dankwoord dus bij deze staan we quitte.
De blonde god, **Joris**, die op onbegrijpelijke wijze de fotonica-sector heeft verlaten op het hoogtepunt van zijn carrière is ook een vermelding waard: als vaste waarde tijdens de koffiepauzes en stichtend lid van de fruitpauzes was hij iemand waarbij ik de boog kon ontspannen. Ook naast het werk is hij nog steeds een welkome vriend op sociale activiteiten (lees: tooghangen) en kortweg een gezellig persoon om bij te zijn en mee te praten, hoewel zijn gitzwart cynisme mij er soms doet aan denken dat ik zelf best wel nog een vrolijke jongen ben. Aan de andere kant weet hij alles over de liefde, geïllustreerd aan de hand van hartverwarmende citaten als "Liefde maakt niet blind... maar zorgt ervoor dat je de gebreken niet wil zien" wat, als je er twee seconden over nadenkt, eigenlijk nergens op slaat. In navolging van het dankwoord in jouw doctoraat zal ik je hier niet expliciet bedanken maar je kan waarschijnlijk wel de scheldtirade tussen de regels lezen.
Nog iemand die een waardevolle gezel vormt is **Dave**, al is het maar om de mensen bewust te maken van de fysieke gevolgen van alcohol. Hét bewijs dat mensen die maar een dik half jaar echt collega's zijn geweest, toch kunnen uitgroeien tot ex-collega's die het tot op zekere hoogte met mekaar kunnen vinden. Ondanks de voedselvergiftigingen (waar ging je nu weeral graag winkelen?) heb ik veel goede herinneringen aan talrijke gezellige avonden of middagen tezamen. En door en met jou heb ik, na vele jaren afwezigheid, terug stappen gezet

in de tenniswereld waardoor mijn verstorven snaren het meteen lieten afweten en ik nu opgescheept zit met die archilelijke rode snaren. Bedankt, Dave.
Karel, je dacht toch niet echt dat ik het bij die ene regel ging laten? Karel, Karel, Karel... De man zonder mening zolang de jouwe maar niet verschilt van de zijne en wiens verontwaardiging is geëvolueerd van “gaan jullie nu al weg?” naar “gaan jullie nu nog weg?”. Menig uur hebben we met mekaar gesleten waardoor er af en toe wel eens een gênante stilte viel die je dan meteen onklaar maakte door erop te wijzen dat we dag voordien nog maar hadden afgesproken en we dus logischerwijs niets nieuws te vertellen hadden. Het merendeel van de tijd kunnen we echter op een aangename manier praten of komt er een nuchtere analyse van jouw kant waar soms moeilijk een speld is tussen te krijgen en die soms ook niet behoeft (zoals over die bloedzuigers die na hun doctoraat een paar maanden “vrijaf” nemen). Dat er nog veel zulke momenten mogen volgen.
Het rijtje collega-vrienden sluit ik af met **Kristof**, alias *The Great Destroyer* op vlak van relaties. Ik zou die jongen hier ook op de korrel kunnen nemen maar het probleem met dat mannetje is dat hij het als een compliment zou interpreteren en met een grijns op die tronie van hem zou zitten van hier tot in Tokyo - twee plaatsen waar hij die bizarre indruk die de meeste mensen van hem hebben heeft achtergelaten. Aan de andere kant: als ik positief over hem ben, heb ik straks ook weer zo’n vervelende, metroseksuele knuffel aan mijn been. Is dit dan wat men een *Catch 22* pleegt te noemen; die term, afgeleid van het gelijknamige boek, waar ik al zoveel over gehoord heb en nu voor de zekerheid maar heb opgezocht op Wikipedia om zeker te zijn dat ik hem hier in de juiste context gebruik? Ik weet het eigenlijk nog niet. Maar wat ik hier wel zwart op wit kan zeggen is dat het iemand is waarmee het, simpel gezegd, gewoon heel erg goed klikt en waarmee ik heel vaak op dezelfde golflengte zit. Meer dan eens is het voorgekomen dat we tot een gat in de nacht/morgen op café zaten en nog niet uitgepraat waren. En ik denk dat we nog lang niet uitgepraat zijn.

Ik begin mijn tocht door het veld van de niet-collega’s bij de waard: **Danny**. In totaal heb ik er waarschijnlijk menig maandloon doorgejaagd bij jou in *De Ploeg* maar elke druppel was het waard. De glimlach waarmee je elke pint of Karmeliet serveerde (of kwam die eerder toen ik mijn portefeuille bovenhaalde) en het sporadisch gratis exemplaar waarmee ik zo gelukkig ben en waarbij jij denkt “jah, die hebben we weer vast voor een jaar” is onbeschrijflijk.
Ook een eervolle vermelding waardig voor het bewerkstelligen van de nodige uitlaatkleppen: **Pol**, van wie ik menig danspasje heb opgestoken, **John** die mij geleerd heeft niet te zuinig te zijn met amaretto in tiramisu en tenslotte **Carlo** van de gelijknamige pizzeria. Tevens gaat ook mijn dank uit naar die andere **Carlo** om een doctoraatsstudent een kans te geven zich echt nuttig te bewijzen.

Dan kom ik bij mijn 4 voornaamste studiegenoten. Er is ten eerste **Da Rik**: ik zal nooit die blik op je wezen vergeten toen ik zei dat ik voor een project al je code had weggeveegd omdat ze op niets trok en ik alles herschreven had. En **Boens**, waarvan ik die ene week dat je zonder lief zat nooit zal vergeten. Hoewel ik je maar één avond echt in volle actie heb gezien, kan ik mij goed inbeelden hoe de overige avonden er aan toe gingen, onder de vleugels van Stevie. **Stevie**, je moet weten dat ik nooit om jou maar altijd met jou heb gelachen en de keren dat ik om je heb gelachen had Mathieu mij opgestookt. Hopelijk vinden we ooit nog eens tijd voor de *Julien challenge*. Tenslotte is er nog de maffiosi van de groep, **Mathieu**, een arme stakker die van zodra hij maar een café binnenstapt misbruikt wordt door een vrouw. Bedankt iedereen.
Arnold Schwarzenegger zei ooit eens in de legendarische actieprent *Commando*: “Let off some steam, Bennett.” Op zich geen memorabele quote ware het niet dat in de film Bennett net doorboord is geweest door een pijp die op haar pad een stoomketel heeft getroffen die achter Bennett staat. Ach ja, je kan het je wel voorstellen zeker? Heel deze situatieschets om te zeggen dat het soms nodig is om wat stoom af te laten na de soms harde werkdagen. Hiervoor dank ik de *Vrienden van de Badminton*: **Diederick**, mijn broer, die later nog aan bod komt, **Céline**, zijn wederhelft, **Lore**, the one that got away, **Stefaan**, the one that got in the way, **Brecht**, een lotgenoot in deze harde stiel, de reeds vermelde **Wout** en **Marie** en de lieve zusjes Vanyzere, **Mieke** en **Tineke**.
Van stoom aflaten naar de druk opvoeren: *Club Guinard*, thuisbasis van enkele van de meest gevreesde zwijnen in de Gentse uitgaansscène en binnenwateren. Vooreerst bedank ik de uitbater **Fabian** voor de jaren onderdak die heb ik mogen genieten maar vooral voor alle jaren dat hij het al uithoudt in mijn vriendenkring. **Dr. Berwouts** die de volgende stap in de evolutie van studentenkot naar studio heeft uitgevonden, nl. de studentenlounge (twee TV’s waarvan één met Ambilight en een karaf Delhaize-whiskey zijn minimumvereistes). Bedankt om samen met mij de rechtse tegenbeweging te vormen in dat linkse bastion waar we vertoefden. Ook bedankt voor de leuke gesprekken en de filmavonden. De naam **Tone** zal u nu waarschijnlijk niet veel zeggen maar leest u er binnen een paar jaar *Forbes* maar eens op na en u weet meteen over wie ik het heb. Naast de rechtse tegenbeweging bestond er ook een kuisbeweging in de Guinard waar hij jammer genoeg enig lid van was. Bedankt niet alleen daarvoor maar om de boel wat op te vrolijken met je bij wijlen norse uitlatingen. Nu ik toch het onderwerp *politiek* heb aangeraakt, moet ik **Brecht** bedanken om mij duidelijk te maken dat links niet hoeft te stoppen bij socialisten maar veel verder kan gaan. Bedankt om in alle discretie toe te stuiken om 5 uur ’s morgens, de vaat te laten staan maar ook een heel klein beetje voor het gezelschap en al bij al vier heel fijne jaren. Oh... kom hier, dat ik u een hand geef! Alvorens ik mij waag aan het fenomeen Van Vaerdegem is er nog **Alex**, de vijfde Beatle van Club

Guinard waarmee ik tezamen met Didier op menig lunchdate ben gegaan. Dan richten we onze blik op Barcelona en komen we **Ons Freija** tegen: het is altijd een plezier en waar genoegen wanneer we mekaar eens treffen zoals die keer dat we jou kwamen bezoeken op de terugweg van Valencia... maar dat ben je waarschijnlijk ook al weer vergeten... Nog verder, ergens in Wortel, vinden we **Freddy** en zijn huis, thuis en keuken. Iemand waarmee ik om de onnozelste dingen in de slappe lach kan schieten; ofwel ligt het gewoon aan zijn gezicht. Ja, en tenslotte, **Koenie**, ook jij bedankt voor een lange en, kortweg, gebeurtenisvolle geschiedenis tezamen (het doet er mij aan denken: jij en Fabian, bedankt voor de hulp bij het 'Julien-incident'). Samenvattend: bedankt allemaal voor talloze mooie herinneringen waar ik mijn kleinkinderen mee kan vervelen op een dag in de verre toekomst waarin Freija hopelijk het woord *saus* correct kan uitspreken.

Al het voorgaande en komende zou mogen geschrapt worden zonder mijn familie. Bedankt **Kathelijn** en **Diederick** om tezamen met mij op te groeien en een leuke resp. zus en broer te zijn die ik altijd graag terugzie. Bijzondere dank gaat uit naar mijn **ouders** die kort gezegd zoveel mogelijk hebben gemaakt in mijn leven, niet alleen door financiële hulp maar veel belangrijker, mij continu te stimuleren mijzelf en mijn enorme intellect uit te dagen, mij onvoorwaardelijk (hoewel, onvoorwaardelijk is misschien veel gezegd) te steunen en mij zoveel warmte toe te dragen. Ik zal jullie daarvoor altijd dankbaar zijn en met veel plezier thuis blijven langskomen (zolang er eten geserveerd wordt). Het klinkt misschien raar voor buitenstaanders maar ik wil toch ook **Ursus**, de **Juno's** en **Zeno** vermelden: trouwe viervoeters die ik heb zien komen en, op Zeno na, jammer genoeg heb zien gaan maar de herinneringen aan hen zijn er enkel van blijdschap en geluk.
Ja, en nu is het (bijna) echt gedaan. Ik ga afsluiten met u te vertellen over een meisje; een meisje waarvoor je een paar minuten langer in bed blijft liggen en iets harder doorfietst/de trajectcontrole tot het uiterste drijft bij het naar huis komen. Een meisje dat met de lichtste aanraking de zorgen van je schouders kan wrijven. Zonder haar zou ik niet op Mark Lanegan afgestapt zijn om met hem een praatje te slaan over Gene Clark. Zonder haar zou ik nooit wegdromen in een bad op de tonen van Low. Zonder haar zat ik nu niet voor de zeventiende keer vandaag naar Country Feedback te luisteren. Zonder haar zou ik niet zo vrolijk zijn als Sioen die op een alweer veel te enthousiaste wijze een optreden geeft. Ik ken haar nog niet zo lang maar ze is mijn beste vriendin en een meisje waar ik, als het even kan, graag nog wat tijd zou mee willen doorbrengen.
Saps que puc parlar molt sobre les coses més estúpides però sobre coses realment importants, poques voltes sé que dir, i en realitat algunes coses parlen millor soles per mí mateixes. Una de elles és que has fet la meua vida millor.

Em considere molt afortunat per poder despertar-me cada dia al teu costat, anar al treball amb un somriure, tornar a casa amb altre somriure i estar en pau mentres els teus dits m'acaricien. T' agraïsc que, fins ara, m'has deixat somriure't, besar-te i voler-te i espere que continuaràs deixant-me fer-ho per molt de temps. No tinc molt que donar-te en compensació però junt amb la gran quantitat de diners en el meu conte bancari, m'oferisc a tu i t'oferisc tickets gratuïts per a escoltar-me tocant el piano, la guitarra, la mandolina o quin instrument siga que aprenga més a tocar. Tracte fet?
Pasar quatre anys investigant sobre fotònica deu ser el treball més avorrit que hi ha però crec que he obtés molt més d'aquest doctorat que qualsevol altra persona abans (diguent-ho una persona que té 2, potser, 3 publicacions). Te vull coseta: ahir, hui un poc més i demà moltísim més. Eres el meu cor i me fas sentir molt orgullós tindre una novia com tu. Citant-me a mi mateix: la vida és de sobte moltísim més, és algo pel que realment val la pena morir i tot açò li ho dec a tu, **la meua dolça princesa**.
En dan wens ik tenslotte nog **Jezus** te bedanken.
Aldus groet ik jullie, waarde vrienden en ex-collega's, vanuit een plaats waar het gras wel degelijk groener is maar de bloemen niet zo talrijk zijn. Om af te sluiten vermeld ik graag een citaat van een bekende Spanjaard met een wel heel opvallend Australisch accent: "What we do in life, echoes in eternity". Het zal toch niet dit doctoraat zijn.

Het pittoreske Ledeberg, juni 2013
Elewout Hallynck

Table of Contents

Dankwoord i

Nederlandse samenvatting xxxiii

English summary xxxix

1 Introduction 1
- 1.1 Labelled biosensing . . . 2
- 1.2 Label-free biosensing . . . 3
- 1.3 Lab-on-a-chip . . . 5
- 1.4 Objectives and applications . . . 6
- 1.5 Thesis outline . . . 11
- 1.6 Publications . . . 13
- References . . . 15

2 Label-free sensor types 19
- 2.1 Surface plasmon resonators . . . 19
- 2.2 Mach-Zehnder interferometers . . . 21
- 2.3 Ring resonators . . . 25
  - 2.3.1 Vernier ring resonators . . . 27
- 2.4 Photonic crystals . . . 30
  - 2.4.1 Band edge detection . . . 31
  - 2.4.2 Defect based devices . . . 34
  - 2.4.3 Resonant gratings . . . 35
  - 2.4.4 Angular spectrum sensing . . . 37
    - 2.4.4.1 Angular spectrum analysis sensor concept and simulation methods . . . 37
    - 2.4.4.2 Different cladding configurations . . . 40
    - 2.4.4.3 Excitation along the ΓK direction . . . 42
    - 2.4.4.4 Other parameters . . . 42
    - 2.4.4.5 Noise analysis and limit of detection . . . 43
  - 2.4.5 Superprism effect . . . 44

2.4.6 Conclusions 47
2.5 Other sensor types 47
2.5.1 Photonics 47
2.5.2 Electronics 49
2.5.3 Mechanics 50
2.6 Conclusions 51
References 51

3 Fabrication **59**
3.1 Silicon-on-insulator 59
3.2 Anisotropic silicon substrate etch 62
3.2.1 Masking materials 65
3.2.2 Sample preparation 69
3.2.3 Protection of the device layer 71
3.3 Isotropic silicon dioxide etch 73
3.4 Conclusions 80
References 81

4 Digital microfluidics with pressure-based actuation **85**
4.1 Theory 85
4.1.1 Surface tension 86
4.1.2 Equilibrium in an underetched membrane 89
4.1.3 Flow through an underetched membrane 94
4.2 Simulations 100
4.3 Experiments 101
4.3.1 Setup 101
4.3.2 Results 105
4.4 Conclusions 114
References 114

5 Differential pressure sensor **119**
5.1 Theory 120
5.2 Simulations 121
5.3 Measurements 128
5.4 Conclusions 135
References 135

6 Increased efficiency grating couplers **139**
6.1 Grating coupler theory 141
6.2 Simulations 145
6.3 Measurements 147
6.4 Conclusions 149

References 150

7 Conclusions and Perspectives **153**

7.1 Conclusions 153

7.2 Perspectives 155

A Silicon membrane fabrication process flow **157**

List of Figures

1 Schematische voorstelling van het principe om d.m.v. druk een druppel te transporteren door een membraan xxxiv
2 SEM foto van een stuk van een Mach-Zehnder interferometer . . xxxv
3 Eerste meetresultaten van de voorgestelde biosensor xxxvi
4 Meetresultaten van een optische druksensor op basis van een Vernier effect ring resonator xxxvii
5 Goudspiegel onder een roosterkoppelaar xxxvii

1 Schematic representation of the principle to transport a droplet through a membrane through means of pressure xl
2 SEM photograph of part of a Mach-Zehnder interferometer xli
3 First experimental results of the proposed biosensor xlii
4 Measurement results of an optical pressure sensor based on a Vernier effect ring resonator xlii
5 Gold mirror below a grating coupler xliii

1.1 The concept of labelled biosensing 3
1.2 Label-free biosensing principle 4
1.3 Schematic of a flow cell used in a Lab-on-a-chip 5
1.4 Progression of the depletion zone in diffusive transport 7
1.5 The convection- and diffusion-dominated regions in a laminar flow 8
1.6 Representation of a small biosensor in a flow cell 9
1.7 Comparison between flow over and flow through the sensor . . . 10
1.8 The principle of transporting a droplet through a membrane using pressure 12

2.1 Working principle of a surface plasmon resonance based sensor with coupling prism 20
2.2 Working principle of a Mach-Zehnder interferometer (MZI) 22
2.3 Representation of a spectral shift in a Mach-Zehnder interferometer 22
2.4 Wavelength vs. effective index in a nanophotonic silicon waveguide 23

2.5 Schematic of a ring resonator and its theoretical wavelength spectrum . . . 26
2.6 Vernier effect ring resonators and their theoretical wavelength spectrum . . . 28
2.7 Effect of the FSR on the wavelength spectrum of Vernier effect ring resonators . . . 29
2.8 Periodicity of photonic crystals . . . 30
2.9 Comparison between the band diagrams of a continuous and periodic medium . . . 32
2.10 An example of a 2D photonic crystal slab . . . 34
2.11 Simulated transmission spectrum of a photonic crystal slab . . . 35
2.12 Band diagrams of defect photonic crystals . . . 36
2.13 Spectrum of a resonant grating . . . 37
2.14 Concept and simulation domain of a photonic crystal for angular spectrum sensing . . . 38
2.15 Simulated fluxes in several directions for a photonic crystal slab . . . 39
2.16 Angular spectrum and cross-section of the Poynting vector for a photonic crystal slab . . . 40
2.17 Angular shift for a set of fixed frequencies and the three different cladding configurations in a photonic crystal slab . . . 41
2.18 Frequency shift at a fixed angle for three claddings in a photonic crystal slab . . . 41
2.19 Angular spectrum when exciting the photonic crystal slab in the ΓK direction . . . 42
2.20 Effect of noise on the peak detection in the angular spectrum of a photonic crystal slab . . . 43
2.21 Limit of detection for three cladding configurations in a photonic crystal slab . . . 44
2.22 Concept of using the superprism effect for biosensing . . . 45
2.23 Isofrequency contours of a photonic crystal . . . 45
2.24 Illustration of two types of optical fibre used for biosensing . . . 48
2.25 An electrical biosensor based on a MOSFET with silicon nanowire 49
2.26 Two mechanical biosensors . . . 50

3.1 SOITEC SmartCut^{TM} process for creating silicon-on-insulator wafers . . . 61
3.2 Different etch depths in SOI . . . 61
3.3 Post-processing steps for obtaining silicon membranes . . . 62
3.4 Dry etching, wet isotropic and wet anisotropic etching of silicon . 63
3.5 Crystal orientation in a silicon wafer . . . 64

3.6 Relevant crystal planes and etching profile for etching silicon with KOH . . . 64
3.7 Pinholes in top silicon layer due to poor silicon nitride quality . . 66
3.8 Redeposition of ProTEK® in etching pits . . . 68
3.9 Schematic overview of backside alignment . . . 69
3.10 Underetch of silicon nitride . . . 69
3.11 Large defect grooves due to poor sample preparation . . . 70
3.12 Surface roughness of an unprocessed, polished and shortly etched silicon substrate surface . . . 71
3.13 Picture of an etched die and microscopic image of an underetched Mach-Zehnder interferometer . . . 71
3.14 Final layer stack of the SOI die . . . 73
3.15 The effect of not protecting the top silicon nitride during dry etching of the hard mask . . . 74
3.16 Surface roughness of silicon due to buffered HF . . . 75
3.17 Stiction after wet HF etching of a large delay spiral . . . 76
3.18 SEM image of an underetched photonic crystal . . . 76
3.19 Picture of silicon tile redeposition on a photonic crystal membrane 77
3.20 Silicon nitride residue after vapour HF etching . . . 78
3.21 Delay spiral after vapour HF etching . . . 80
3.22 Buckling in silicon membranes . . . 81

4.1 Typical dimensions of a photonic crystal membrane and part of a delay spiral of a Mach-Zehnder interferometer . . . 86
4.2 Molecular representation of surface tension . . . 87
4.3 Hydrophilic vs. hydrophobic surfaces . . . 88
4.4 Capillary rise and a pendant droplet . . . 89
4.5 Surface non-uniformity and Cassie's law . . . 90
4.6 Effective contact angle due to the Cassie effect . . . 91
4.7 Pressure imbalance when applying a droplet . . . 92
4.8 Propagation of a droplet through the biosensor . . . 94
4.9 Bernoulli's principle for a thin membrane . . . 96
4.10 Hagen-Poiseuille flow and the electrical equivalent . . . 97
4.11 Development of a laminar flow . . . 99
4.12 Simulated velocity fields in a rectangular channel . . . 101
4.13 Simulated velocity fields in a cylindrical channel . . . 102
4.14 Schematic representation of grating couplers . . . 103
4.15 Chip holder that allows for a pressure difference to be applied over the membrane . . . 104
4.16 Measurement equipment used . . . 105
4.17 Movie stills of a droplet going up and down through a membrane 106

4.18 Picture of an underetched trench near a photonic crystal 107
4.19 Wavelength spectrum of a photonic crystal without analyte 108
4.20 Picture of the measured device 109
4.21 Time vs. wavelength shift for the cases with and without pumping 110
4.22 Zoom of the time vs. wavelength shift for the cases with and without pumping 111
4.23 Electric field magnitude of the TE and TM modes 113

5.1 Graphical representation of a clamped membrane 121
5.2 Microscopic image of part of a silicon ring resonator where the silicon substrate is locally etched away (seen from the substrate side). 124
5.3 COMSOL simulation domain for investigating the elasto-optic effect 124
5.4 Dependence of the sensor response on the position of the waveguide 125
5.5 The strain vectors for a waveguide located in the centre of a membrane (Δp = -80 kPa) 125
5.6 Horizontal strain in the complete membrane 126
5.7 Dependence of the sensor response on the buried oxide layer thickness 126
5.8 Sign of the horizontal strain for two buried oxide layer thicknesses 127
5.9 The effect of pre-stress on the sensor response 127
5.10 Schematic overview of the pressure set-up used in the measurements 128
5.11 Layer stack for the simple ring resonator sensor 129
5.12 Pressure difference vs. wavelength shift for a simple ring resonator 130
5.13 The elasto-optic effect in a ring resonator 130
5.14 Mach-Zehnder-interferometer-based pressure sensor 131
5.15 Sensor response of a Mach-Zehnder interferometer for pressure sensing 131
5.16 Pressure sensor based on a Vernier effect ring resonator 132
5.17 Optical spectrum of a Vernier effect ring resonator 132
5.18 Pressure difference vs. wavelength shift for a Vernier effect ring resonator 133

6.1 A nanophotonic waveguide and optical fibre depicted together on the same scale 140
6.2 3 commonly used coupling techniques 141
6.3 Diffraction directions of light in a grating coupler 141
6.4 Graphical representation of Bragg's law 143
6.5 1D and 2D grating couplers 144

6.6 Diffraction directions of light in a grating coupler with bottom mirror 145
6.7 Buried oxide layer thickness vs. simulated coupling efficiency in a focused grating coupler 146
6.8 Simulated coupling efficiency in function of wavelength for 1D and 2D grating couplers with and without bottom mirror 147
6.9 Picture of an actual gold-coated device and 1D and 2D grating couplers 148
6.10 Measurement results of mirror-coated 1D and 2D grating couplers 149

List of Tables

4.1 Parameters used for the measurements of MZI-based biosensors. 110

5.1 Constants used in COMSOL simulations. 123
5.2 Comparison of proposed devices to pressure sensors published in literature 134

List of Acronyms

A

AC	Alternating Current

B

BCB	Benzocyclobutene
BOX	Buried oxide
BSA	Bovine Serum Albumin

C

CMOS	Complementary Metal Oxide Semiconductor
CMP	Chemical Mechanical Polishing
CCD	Coupled Charge Device

D

DAQ	Data acquisition
DI	Deionised
DNA	Deoxyribonucleic acid

E

ELISA	Enzyme-linked immunosorbent assay
EM	Electro Magnetic

F

FDTD	Finite Difference Time Domain
FOM	Figure of Merit
FSR	Free spectral range
FWHM	Full Width at Half Maximum

H

HF	Hydrofluoric acid
HIV	Human Immunodeficiency Virus

I

IC	Integrated Circuit
IPA	Isopropyl alcohol, Isopropanol
ISFET	Ion-sensitive field-effect transistor

K

KOH	Potassium hydroxide

L

LED	Light emitting diode

LOD	Limit of Detection
LPCVD	Low-Pressure Chemical Vapour Deposition

M

MOSFET	Metal-oxide-semiconductor field-effect transistor
MZI	Mach-Zehnder Interferometer

N

NI	National Instruments

P

PBS	Phosphate Buffered Saline
PhC	Photonic Crystal
PIC	Photonic Integrated Circuit
PECVD	Plasma-Enhanced Chemical Vapour Deposition

R

RI	Refractive Index
RIU	Refractive Index Unit

S

SAW	Surface acoustic wave
SEM	Scanning Electron Microscope
SLED	Superluminescent LED
SMF	Single Mode Fibre

SNR	Signal-to-noise ratio
SOI	Silicon-On-Insulator
SP	Signal processing
SPR	Surface plasmon resonance

T

TE	Transverse Electric
TM	Transverse Magnetic

U

UV	Ultraviolet

Nederlandse samenvatting –Summary in Dutch–

Onderzoek naar medicatie en medische diagnose zijn twee multi-miljoen-dollar industrieën waar efficiënte biosensoren van groot nut kunnen zijn. Een van de kernfactoren die de performantie van zo een biosensor beïnvloeden is de snelheid waarmee biomoleculen het sensoroppervlak bereiken. Indien we simpelweg de vloeistof met daarin de biomoleculen op de sensor aanbrengen, moeten we wachten totdat de moleculen naar het sensoroppervlak diffunderen: in theorie kan het soms weken duren eer genoeg biomoleculen het sensoroppervlak hebben bereikt om een significant signaal te produceren. Door microkanaaltjes aan te brengen boven het sensoroppervlak waarin we een laminaire stroom introduceren, kunnen we de snelheid waarmee moleculen het oppervlak bereiken verbeteren gezien de moleculen nu getransporteerd worden door convectie in de stromende vloeistof. De snelheid dichtbij de kanaalwanden is in een laminair stromingsregime echter zo klein dat er een regio ontstaat waar biomoleculen nog steeds door middel van diffusie het sensoroppervlak moeten bereiken. In gevallen waar de concentratie aan biomoleculen in de buffervloeistof relatief laag is, kan dit een probleem vormen gezien een fractie van de reeds weinige biomoleculen gewoonweg de sensor zal passeren zonder de kans te krijgen de diffusiezone te overbruggen.

Om dit probleem op te lossen stellen we een methode voor die geïllustreerd is in Figuur 1: een kleine druppel vloeistof met daarin biomoleculen wordt aangebracht op een speciaal type biosensor dat bestaat uit een dun membraan met gaten erin. Aanvankelijk zullen reeds enkele biomoleculen binden in de gaten, waar we willen dat ze binden. Als we vervolgens een onderdruk aanleggen onder de druppel, kunnen we ervoor zorgen dat de druppel door de gaten in het membraan wordt getrokken tezamen met de biomoleculen, waardoor die een kans krijgen om te binden in de gaten. Eens de druppel door de gaten is gepasseerd, kunnen we een overdruk aanleggen die de druppel terug door de gaten duwt. Op dat moment krijgen de biomoleculen opnieuw een kans om te binden in de gaten. Door deze cyclus een paar keren te herhalen, kunnen we ervoor zorgen dat een groot deel van de biomoleculen zal binden in de gaten over een

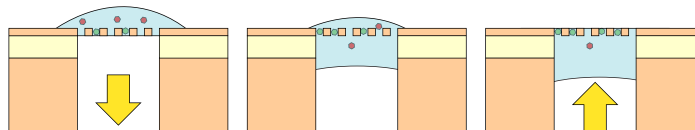

Figuur 1: Door onderdruk aan te leggen aan de onderkant van de druppel vloeistof, kunnen de biomoleculen getransporteerd worden door het membraan. De druppel kan terug door het membraan geduwd worden door overdruk aan te leggen. Deze cyclus kan verscheidene keren herhaald worden zodat men er zich van kan vergewissen dat de meeste biomoleculen gebonden zullen zijn in de gaten.

relatief korte tijdspanne.

Om de effectiviteit van deze methode te kwantificeren hebben we een *transducer* nodig die de bindingsgraad, of een andere eigenschap, vertaalt in een meetbaar signaal. Gezien de grote markt voor biosensoren zal het niet verbazen dat er reeds behoorlijk wat onderzoek naar is gedaan en er zijn dan ook verschillende technieken om een meetbaar signaal te bekomen. In dit werk zullen we gebruik maken van fotonica. Hoewel we het misschien niet altijd beseffen, is het praktisch onmogelijk om ons een wereld voor te stellen zonder fotonica: van de optische vezels die op de zeebodem liggen en praktisch alle continenten met elkaar verbinden tot de zonne-energie die geoogst wordt en omgezet in elektriciteit; het zijn allemaal toepassingen waarvan het kernelement licht is. Gezien dit domein zo breed is, zullen we ons focussen op een trend die de voorbije jaren sterk aan het groeien is en reeds gezien is in de elektronica: integratie. Met behulp van verschillende technologieplatformen (waarvan sommige hun wortels hebben in de elektronica) kunnen we relatief kleine (in sommige gevallen enkele grootteordes kleiner dan de diameter van een menselijk haar) structuren maken die licht kunnen transporteren of geleiden op een gelijkaardige manier als koperbaantjes op een printplaat in elektronica dat doen voor elektrische signalen. Hoewel het aantal potentiële toepassingen (gaande van optische interconnects tot optische lichtbundelsturing) enorm is, zijn er tot op heden slechts enkele toepassingen die de markt hebben bereikt. Een van die toepassingen is een optische biosensor.

Het doel van dit doctoraat was bovenvernoemde methode om een druppel door een membraan te transporteren te implementeren in een optische biosensor, op basis van een Silicium-op-Isolator platform. Gebruik makende van deze mature technologie die ons toelaat kleine sensoren op grote schaal te produceren, kunnen we licht transporteren in golfgeleiders, gedefinieerd in een kleine 220 nm dunne siliciumlaag, zodat het de aanwezigheid van biomoleculen kan

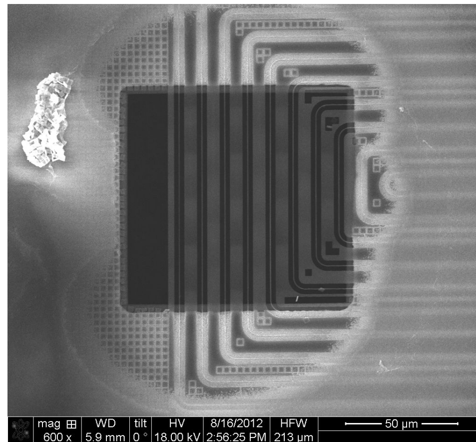

Figuur 2: Foto gemaakt met een *scanning electron microscope* van een stuk van een Mach-Zehnder interferometer: een fotonische structuur die gebruikt kan worden om de binding van biomoleculen te vertalen in een optisch signaal.

voelen in de nabijheid van het golfgeleideroppervlak. Gezien het fabricageproces om deze silicium chips te produceren gestandardiseerd is, kan het niet gemakkelijk aangepast worden om te voldoen aan individuele behoeften. Om die reden moesten we nog extra processtappen uitvoeren op de chips die we ontvingen van de chipfabrikant in onze eigen stofvrije ruimtes. Dat fabricageproces bestaat kortweg uit twee stappen: eerst moet een 250 µm dik silicium substraat lokaal verwijderd worden en vervolgens moet een 2 µm dunne silicium dioxide laag weggeëtst worden. Wat dan overblijft is een dunne lichtgeleidende silicium laag die het *transducer* gedeelte van de sensor bevat. De silicium substraatets werd uitgevoerd met een anisotroop nat etsproces met KOH. Het tweede gedeelte werd gedaan met HF om het silcium dioxide weg te etsen. Figuur 2 toont een deel van een fotonische structuur waar zowel het substraat als de silicium dioxide laag lokaal zijn verwijderd. Een vloeistof is dan in staat om rond de kleine silicium golfgeleiders te vloeien.

Na fabricage van deze componenten, hebben we ze gekarakteriseerd in een experiment waar *Bovine Serum Albumin* bindt met silicium. We konden aantonen dat de snelheid waarmee biomoleculen het sensoroppervlak bereiken met een factor 3 kan verbeterd worden (zie Figuur 3). Op het moment van de experimenten was er geen geschikte oppervlaktechemie beschikbaar en toekomstige experimenten, waarbij lage concentraties biomoleculen worden gebruikt, zullen het ware potentieel van deze nieuwe techniek moeten onthullen.

Het fabricageproces dat ontwikkeld werd om bovenvermelde biosensoren

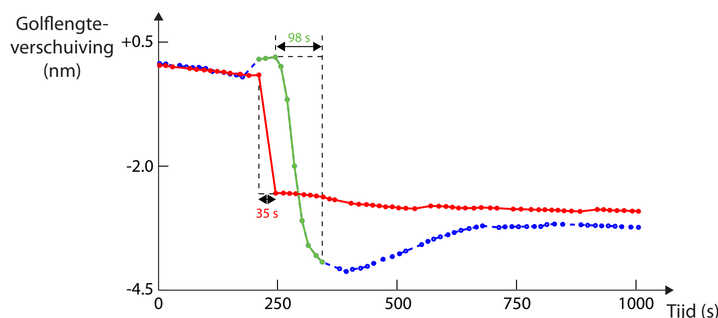

Figuur 3: Door de vloeistof die biomoleculen bevat door de sensor te laten stromen in plaats van erlangs, kunnen we de snelheid waarmee moleculen het sensoroppervlak bereiken verhogen met een factor 3. Verdere experimenten moeten het ware potentieel van deze nieuwe methode onthullen.

te produceren kan ook gebruikt worden in andere toepassingen. Een daarvan is een geïntegreerde optische druksensor: door een bepaalde fotonische component op een dun membraan te plaatsen en een drukverschil aan te leggen over dit membraan (i.e. de druk boven en onder het membraan zijn niet gelijk), zal de sensor een signaal produceren dat ons toelaat de exacte waarde van dat drukverschil te bepalen. We hebben verschillende typische fotonische componenten onderzocht (een ring resonator, een Mach-Zehnder interferometer en een Vernier effect ring resonator) door ze te fabriceren en karakteriseren. Figuur 4 toont hoe de best werkende sensor reageert in functie van de aangelegde druk. Zoals intuïtief kan verwacht worden, zal een fotonische structuur op een dunner membraan resulteren in een meer gevoelige sensor. Onze druksensoren staan aan de top van geïntegreerde druksensoren op het moment van schrijven.

Een laatste toepassing die onderzocht wordt in dit werk is het verhogen van de efficiëntie van roosterkoppelaars. Deze componenten vormen een interface tussen een geïntegreerde optische chip en de buitenwereld door licht te koppelen tussen een optische vezel en een golfgeleider die soms een paar grootteordes kleiner is. Een bekend probleem is dat deze structuren in hun meest eenvoudige vorm een zwakke koppelefficiëntie bezitten, vergeleken met andere technieken. De reden hierachter is dat er, onvermijdelijk, altijd een deel van het licht naar het substraat wordt gekoppeld waar het verloren gaat. Door lokaal het substraat te verwijderen en op de silicium dioxide laag een dunne metallische spiegel aan te brengen (in ons geval goud), kunnen we dit licht terug reflecteren naar de roosterkoppelaar waar het constructief kan toegevoegd worden aan het reeds gekoppelde deel van het licht. Figuur 5 toont zo een roosterkoppelaar waar het

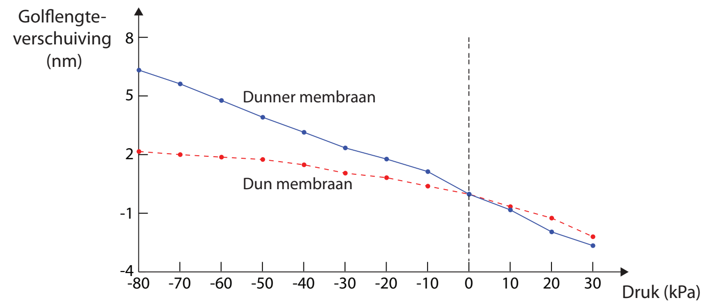

Figuur 4: Door een Vernier effect ring resonator op een dun drukgevoelig membraan te plaatsen, kunnen we heel gevoelige geïntegreerde optische druksensoren bekomen. De sensoren die we gekarakteriseerd hebben presteren tot 10 keer beter dan andere geïntegreerde optische druksensoren, gepubliceerd in de literatuur.

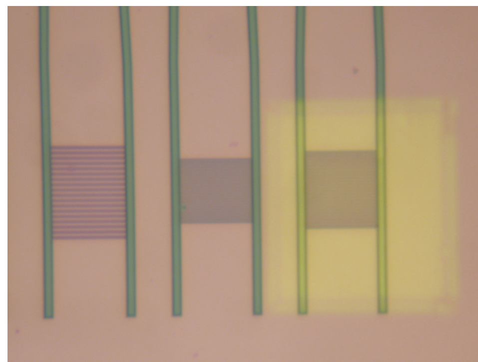

Figuur 5: Door het substraat onder roosterkoppelaars lokaal te verwijderen en een goudspiegel te deponeren wordt de koppelefficiëntie ruwweg verdubbeld.

substraat lokaal is verwijderd en waar een goudspiegel is aangebracht op de silicium dioxide laag. We hebben een koppelefficiëntie verhoging met een factor 2 aangetoond voor zowel een 1D als 2D roosterkoppelaar (die laatste structuur wordt gebruikt om simultaan licht van twee orthogonale polarisaties te koppelen). Hoewel dit concept al eerder is aangetoond in de literatuur, met gelijkaardige resultaten, hebben we dezelfde structuur bekomen met een eenvoudiger fabricageproces.

English summary

Drug discovery and diagnostics are two multi-million-dollar industries where effective biosensors can be of great use. One of the key factors that influences the performance of such a biosensor is analyte delivery: the rate at which biomolecules floating in a buffer liquid are delivered to the sensor surface. When we simply apply the analyte containing the biomolecules on the sensor, we have to wait until the molecules diffuse towards the sensor surface: in some cases it could take up to weeks until enough molecules have reached the sensor surface to produce a significant signal. By creating microchannels over the sensor surface in which we introduce a laminar flow, we can improve analyte delivery since the biomolecules are transported through convection in the moving fluid. However, the velocity near the microchannel walls in a laminar flow regime is so small that there is still a region through which the biomolecules have to diffuse. In cases where the concentration of biomolecules in the buffer liquid is relatively low, this can pose a problem since part of the already few biomolecules will simply pass the sensor before they get a chance at traversing this diffusion region.

To overcome this problem, we propose a flow scheme as illustrated in Figure 1: a small droplet of analyte is applied on a special type of biosensor that is basically a thin membrane with holes in it. Initially, some biomolecules will bind inside the holes, where we want them to. If we then apply underpressure at the bottom of the droplet, we pull the droplet through these holes along with the biomolecules, giving them a chance at binding in the holes. Once the droplet has passed completely through the membrane, we apply an overpressure to push it back through at which point the biomolecules pass again through the holes, giving them another chance at binding. By repeating this cycle a number of times, we can ensure that a large fraction of biomolecules will have bound in the holes in a relatively short period of time.

In order to quantify the performance of this flow scheme we need a *transducer* that is able to translate the amount of binding, or another property, into a measurable signal. Keeping in mind the big market for biosensors, it comes as no surprise that already quite some research has been performed on these devices. Therefore, there are several techniques to obtain a measurable signal.

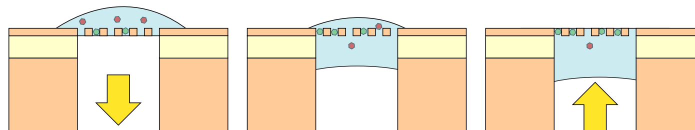

Figure 1: By applying underpressure at the bottom of the liquid droplet, the biomolecules are transported through the sensor membrane. The droplet can be pushed back by applying overpressure. This cycle can be repeated several times to ensure most biomolecules have bound in the membrane holes.

In this work we will make use of photonics. Although we might not always realise it, it is hard to imagine a world without photonics: from the optical fibres lying on the seabed, connecting virtually all continents through the internet, to solar energy that is harvested to create electricity; they are all applications of which the core element is light. Since this field is quite broad we will focus on a trend that has been growing over the couple of years and has been seen in the past in electronics: integration. Using several technology platforms (some of which have their roots in electronics) we can create relatively small (down to a few orders of magnitude smaller than the diameter of a human hair) structures that can transport or guide light much like the copper tracks on a printed circuit board in electronics can do so for eletrical signals. Although the number of potential applications (ranging from optical interconnects to optical beamsteering) is vast, as of yet only a few applications have reached the market. One of these applications is an optical biosensor.

The goal of this PhD was to implement the above-mentioned novel flow scheme in an optical biosensor on a Silicon-on-Insulator platform. Using this mature technology that allows for small sensors to be produced on a large scale, we can transport light in waveguides, defined in a small 220-nm-thin silicon layer, so that it can sense the presence of biomolecules close to the waveguide surface. Since the fabrication process of these silicon chips is standardised, it cannot easily be adjusted to suit individual needs. Therefore, we had to perform post-processing steps on the received devices in our own clean room facilities. Basically, the fabrication process we devised comprises two steps: first a 250-µm-thick silicon substrate has to be locally removed and second, a 2-µm-thin silicon dioxide layer needs to be etched. What remains then is thin light-guiding silicon layer which contains the transducer. The silicon substrate etch was executed using an anisotropic wet etching process with KOH. The second part was done using HF to etch the silicon dioxide layer. Figure 2 shows a part of a photonic structure where both the substrate and silicon dioxide layer are locally re-

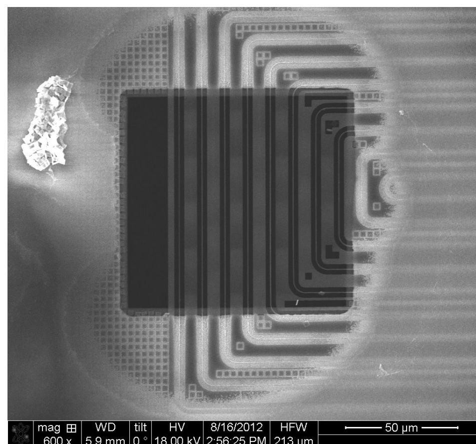

Figure 2: A picture made using a scanning electron microscope of a part of a Mach-Zehnder interferometer: a photonic structure that can be used to translate the binding of biomolecules into an optical signal.

moved. Liquid is then able to flow around these small silicon waveguides.

After fabrication of these devices, we characterised them in an experiment where Bovine Serum Albumin binds to bare silicon. We were able to show that the analyte delivery rate can be improved by at least a factor of 3 (see Figure 3). At the time of the experiments, no appropriate surface chemistry was available and further experiments with low-concentration analyte have to reveal the true potential of this new flow scheme.

The fabrication process developed to produce the above-mentioned biosensors can also be used for other applications. One of these is an integrated optical pressure sensor: by placing a certain photonic structure on a thin membrane and applying a pressure difference over this membrane (i.e. the pressure above and below the membrane are not equal), the sensor will produce a signal that allows us to determine the value of this pressure difference. We have investigated several typical photonic structures (ring resonator, Mach-Zehnder interferometer and a Vernier effect ring resonator) by fabricating and characterising them. Figure 4 shows the response of the best performing sensor in function of the applied pressure difference. As can be intuitively expected, a photonic structure on a thinner membrane produces a more sensitive structure. Our pressure sensors rank at the top of integrated optical pressure sensors at the time of writing.

A final application that is discussed in this work is that of increasing the efficiency in grating couplers. These components basically form an interface between a integrated optical chip and the outside world by coupling light between an optical fibre and a waveguide that can be more than an order of magnitude

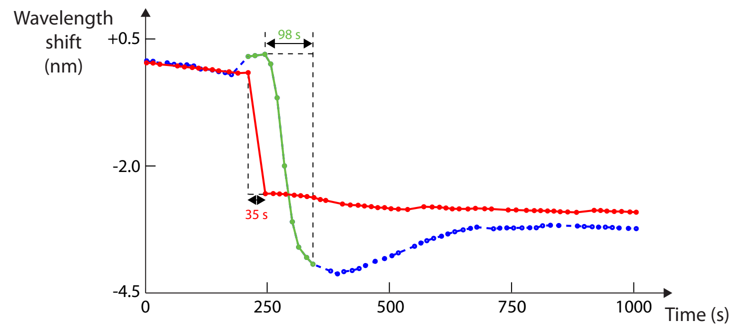

Figure 3: Letting the analyte flow through the sensor instead of past it, increases the target delivery rate by at least a factor of 3. Further experiments using low-concentration analyte could uncover an even greater increase.

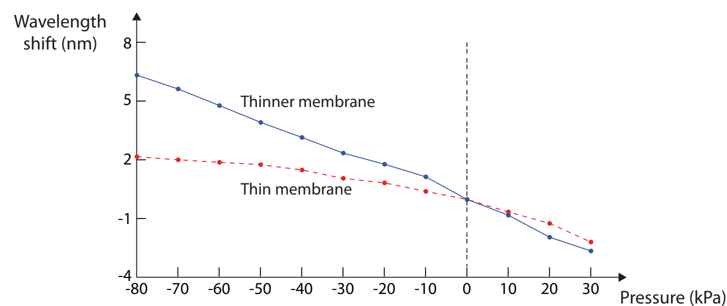

Figure 4: By placing a Vernier effect ring resonator on a thin pressure-sensitive membrane, we can produce highly sensitive integrated optical pressure sensors. As can be seen, decreasing the membrane thickness enhances the sensitivity. The devices we characterised outperform other integrated optical pressure sensors published in literature by more than a factor of 10.

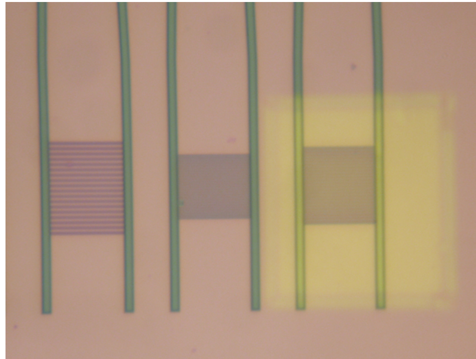

Figure 5: Locally removing the substrate and applying a gold mirror coating underneath grating couplers roughly doubles the coupling efficiency.

smaller. A common problem in these basic structures is their relatively poor coupling efficiency, compared to other techniques. The reason behind this is that, unavoidably, part of the light is also coupled towards the substrate where it is lost. By locally removing the substrate and coating the thin silicon dioxide layer with a metallic mirror (in our case gold), we can reflect this light directed towards the substrate back in the grating coupler where it can constructively add to the already coupled portion of the light. Figure 5 shows such a grating coupler where the substrate has been locally removed and the silicon dioxide layer has been coated with a gold mirror. We were able to increase the coupling efficiency of both 1D and 2D grating couplers (used to simultaneously couple light of perpendicular polarisations) by a factor of 2. Although this concept has been demonstrated before in literature, with similar results, we were able to obtain the same device using a simpler fabrication process.

"Far better is it to dare mighty things, to win glorious triumphs, even though checkered by failure... than to rank with those poor spirits who neither enjoy nor suffer much, because they live in a grey twilight that knows not victory nor defeat."

Theodore Roosevelt, 26th American President, 1858-1919

1 Introduction

Before a drug is allowed on the consumer market, a process that takes up to tens of years can precede it [1]. At the start of this process, before testing on live subjects takes place, the potential drug has to be tested for several important criteria: is it stable, is it effective, is it toxic to some cells? Extensive studies take place to give a well-founded answer to all of these questions and one of the elements that help answering those questions are biosensors. A label-free biosensor basically translates molecular dynamics (e.g. binding levels and binding rates) into a signal that can be monitored, in general in real-time, by a computer. After data analysis, the user can gain insight in important characteristics such as specificity, kinetics and affinity of the biomolecular interactions [2]. Based on these experiments, a decision of whether drug development can continue or not can be made before testing on live subjects has taken place.

Another field that requires knowledge of biomolecular behaviour is that of diagnostics [3]: a diagnosis based merely on the symptoms is often not sufficient and additional testing is required on e.g. bodily fluids. Although nowadays they are not yet commonly employed, biosensors have the potential to make this process more efficient and cost effective (in certain cases, they have been able to detect a single virus in a blood sample [4]). It would also be possible to use biosensors for disease prevention: certain hereditary diseases can be detected by deoxyribonucleic acid (DNA) sequencing [5]. However, not everything is visible or understood yet on a genetic level: sometimes, abnormalities occur

during the expression of proteins. The study of this dynamic protein behaviour is commonly referred to as proteomics [6] and is often more complex than genomics: while genes do not change significantly over time, proteins do evolve which makes proteomics a much more complex field.

In order to compare several biosensors, a few figures of merit (FOM) are available which can be, depending on a specific application, more or less important. The limit of detection (LOD) is usually an important measure and basically refers to the minimum amount of biomolecules or other analyte that can be detected. E.g. a biosensor based on surface plasmon resonance (see Chapter 2) is able to detect 1 pg/mm^2 surface coverage of biomolecules [7]. Selectivity is also crucial in many cases and refers to the property of the sensor to allow only the desired molecules to be detected and reject other molecules. A property that will be later addressed in this work is throughput. This is basically a combination of speed (e.g. sample preparation, calibration, detection) and multiplexing capabilities: analysing one sample for several targets in parallel is more efficient than carrying out this task in series. Other FOMs include cost (of both a single chip and read-out equipment) and portability (e.g. a general physician is able to use the equipment at a patient's home). Note that not all these FOMs can be quantitatively determined and it is therefore not always straightforward to compare several biosensors.

There are numerous ways to do biosensing [2, 8–10] but they can, in general, be divided into two categories: labelled and label-free biosensing. In the following, we will review the basic principle of both methods, identify a commonly encountered problem in some types of biosensors and propose a solution which will be investigated in the course of this thesis.

1.1 Labelled biosensing

The most commonly employed biosensing technique nowadays makes use of luminescent molecules that attach to the target molecules and produce a signal once illuminated [2]. The luminescent molecules are also referred to as label molecules hence the name labelled biosensing. The principle of a labelled biosensor is similar to the already well-established ELISA [10], which is short for enzyme-linked immunosorbent assay (a term used to describe an analytic procedure where the amount or functional activity of an analyte in an organic sample is qualitatively or quantitatively measured), which is used e.g. to detect the human immunodeficiency virus (HIV) [11] and produces a visible colour signal. The working principle is as follows (see also Figure 1.1): the target molecules (i.e. analyte) bind to a substrate, either directly or through receptor molecules (in which case we speak of a sandwiched assay [12] since the analyte is sandwiched between receptor and marker molecules). After that, the marker molecules are

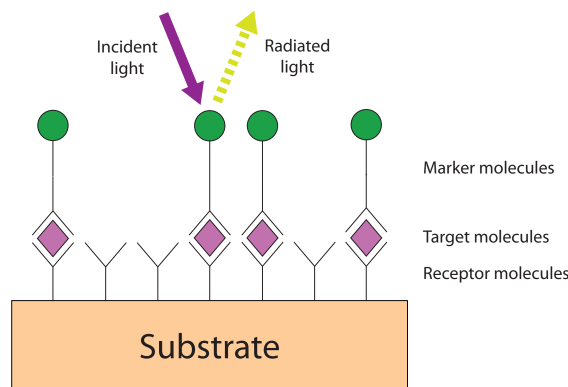

Figure 1.1: In labelled biosensing, the target molecules bind to receptor molecules on a substrate so they become immobilised. After that, marker molecules bind to another site of the target molecules. Excess marker molecules are removed and the substrate is illuminated. The intensity of the light is then measured, providing information on the target molecule concentration.

able to bind to another site of the analyte (in some cases, intermediary molecules are used to bind between the analyte and the marker molecules). The excess marker molecules (that have not bound to the target molecules) are then washed away (note that in practice a washing step is performed after each introduction of a new molecule) and the substrate gets illuminated. The intensity of the perceived colour is then a measure for the amount of target molecules that are present in the sample. This can be measured qualitatively (i.e. with the naked eye) or quantitatively using a camera or optical power meter. In practice, ELISAs take place in reaction tubes or microtitre plates [13] (a large matrix of small reaction tubes).

1.2 Label-free biosensing

While labelled detection can be very sensitive (up to a single virus [4]), there are some disadvantages. The entire assay is often time-consuming: in practice, the marker molecules do not always bind directly to the target molecules and intermediary molecules are required [14]. Taking into account that between each step, a washing step takes place and that binding of molecules does not occur instantaneously, we can understand the laborious nature of this process. Another disadvantage in some cases is that the emission efficiency of certain label molecules can degrade over time. Third, quantitative analysis can be hindered

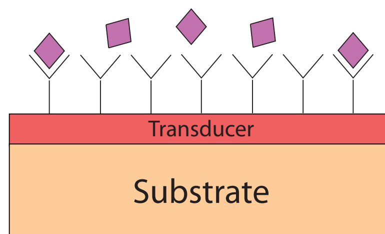

Figure 1.2: A transducer is coated with receptor molecules. When target molecules bind to these receptor molecules, the physical properties of the analyte generate an altered state of the transducer which translates this into a measurable signal.

by the fact that it is sometimes not possible to precisely control the amount of marker molecules that bind to one target molecule. Furthermore, marker molecules might interfere with the function of a biomolecule [8]. Lastly, it is not possible to monitor the signal in real-time: only after the complete labelling process is finished, the signal is interrogated. Because of this, it is impossible to extract binding kinetics data (i.e. a binding curve, showing the amount of binding of target to receptor molecules as a function of time), which is desired in some applications (e.g. drug research).

Label-free biosensors, in general, do not suffer from these drawbacks: biomolecules are measured in real-time in an unaltered form. As illustrated in Figure 1.2, a transducer is coated with receptor molecules which can be continuously interrogated. The target molecules will bind to the receptor molecules and their physical properties (e.g. optical, mechanical or electrical) will have an effect on the transducer which translates these properties into a measurable signal.

Due to the continuous measurement, it is possible to receive information on binding kinetics or affinity which was not possible in the labelled sensing scheme. Multiple parameters can be monitored simultaneously by applying different receptor molecules to several transducers on the same substrate, providing multiplexing functionality [7]. In the following, we will only consider label-free biosensors. For a state-of-the-art overview of optical label-free biosensors, we refer to Chapter 2 where the most common types are discussed alongside key publications.

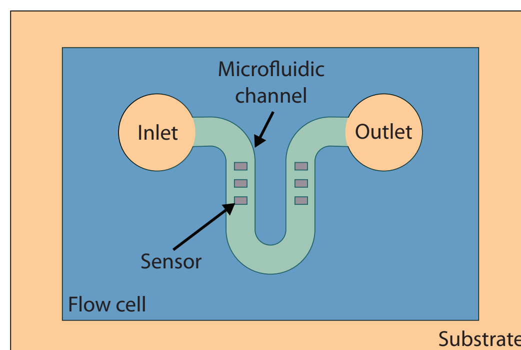

Figure 1.3: A flow cell is attached to the substrate containing the chemically functionalised biosensors. The flow cell is closed at the top except for an opening for flow inlet and outlet.

1.3 Lab-on-a-chip

Label-free biosensing already provides an improvement cost wise since it is faster (since an assay typically requires less man-hours) than labelled techniques. In some cases however, relatively expensive equipment is still required that is, furthermore, designed to operate in a very controlled environment [15]. For reducing the cost even further, increasing portability and relaxing the operating conditions for both labelled and label-free techniques, the concept of a Lab-on-a-chip has been conceived. Although the term is quite general, in this case we can use it to describe the integration of microfluidics and the transducer [16]. Using microfluidics on a chip, sample preparation steps like mixing or centrifugation can be incorporated in the sensor so there is no longer a need for, often expensive, external laboratory equipment to perform these tasks. There are many implementations of microfluidics or methods of transporting the analyte to the sensor but in its most standard form, a microfluidic section, often referred to as a flow cell, is glued onto the sensor surface [17] (see Figure 1.3) and the analyte is flown over the coated sensor surface, bringing the target molecules in close contact with the receptor molecules. Since we are working in a closed system, the Lab-on-a-chip is less susceptible to contamination and we also require less analyte volumes (nothing is wasted between preparatory steps and application to the sensor). Besides these advantages and the reduced cost, other advantages include compactness and increased ease of use.

1.4 Objectives and applications

Biosensors are becoming increasingly more sensitive up to the point where single molecules and femto-molar concentrations can be detected [18, 19]. However, some authors suggest that the fundamental detection limit of some of these sensors has not yet been reached or the time it takes to detect a single molecule can be greatly improved by optimising the transport mechanism of the target molecules dissolved in the analyte [20, 21]. The binding rate of target molecules to their respective receptor molecules on the sensor surface is either limited by mass transport or reaction kinetics. In the following, we will only focus on the former. There are several ways to transport the target molecules to the sensor surface with the simplest form being pure diffusion: due to thermally induced random motion of particles, such as Brownian motion [22], biomolecules will diffuse towards the sensor surface where they bind to the receptor molecules. A diffusion process is governed by Fick's first law [23]:

$$J = -D\nabla c \tag{1.1}$$

where J is the particle flux in $\frac{kg}{m^2 s}$, D is the diffusion constant in $\frac{m^2}{s}$ and c the particle concentration in $\frac{kg}{m^3}$. This means that the amount of diffusion is directly proportional to the concentration gradient of target molecules in the analyte. Consider a biosensor in a long channel that is closed at the top as in Figure 1.4 with a stationary fluid. At t=0, the concentration in the analyte is uniform over the channel. When molecules close to the sensor surface bind with the receptor molecules, a concentration gradient is created and diffusion starts. As more molecules diffuse towards the sensor, a concentration depletion zone is created. It can be shown that the thickness δ of this depletion zone is given by $\sqrt{Dt}$. This depletion zone will grow radially over time until it reaches the channel's top wall after which it will continue expanding into the channel. The flux J can be approximated as $\frac{Dc_0}{\delta}$, where c_0 is the initial target molecule concentration. This implies that the diffusion flux will decrease over time as the depletion zone grows. For bovine serum albumin (BSA), with a diffusion constant D of $6.29 \times 10^{-11} \frac{m^2}{s}$ [24], already after 40 s the depletion layer will have reached the top of a 50-µm-high channel and diffusion becomes extremely slow. Indeed, in some cases, where the amount of target molecules in the analyte is in the order of hundreds of molecules, it can take up to months until enough molecules have reached the sensor through diffusion [20].

A way to improve target molecule transport is not to use a stationary fluid, but to introduce a laminar flow in the channel (note that turbulent flow would be more effective at mixing molecules in the analyte, but since such a flow is hard to achieve in a microfluidic channel at practical flow rates, we will disregard it henceforth). Depending on the flow rate, the delivery of new target

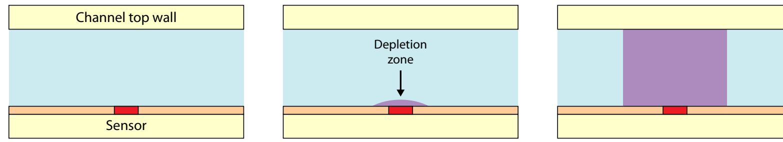

Figure 1.4: Schematic overview of the growing depletion zone in diffusion controlled mass transport: initially, no concentration gradient is present (left). Target molecules bind to receptor molecules on the sensor, creating a concentration gradient which induces a small depletion zone (middle). Over time, the depletion zone will grow radially until it reaches the top of the channel and extends further in the horizontal direction.

molecules can counteract the growth of the depletion zone. A laminar flow in a standard microfluidic channel is always bound by the condition that the velocity at the channel walls has to equal zero (the no-slip condition). It can be shown that a fully developed laminar flow in a channel consisting of two parallel plates has a parabolic velocity profile $v_z(x)$ meaning that the fluid speed near the walls is much smaller than in the centre of the channel. In the centre of the channel, the flow velocity is high enough to counter the depletion zone created through diffusion, whereas near the channel walls diffusion will remain the dominant effect (see Figure 1.5). A permanent depletion zone directly above the sensor will always remain, even when increasing the flow rate significantly [21]. To quantify this effect, the Peclet number is used, which is defined as the ratio of the diffusive time to the convective time for a molecule to travel the same distance. It can be approximated as follows:

$$Pe \approx \frac{Q}{DW_{channel}} \tag{1.2}$$

where Q is the flow rate, D the diffusion constant and $W_{channel}$ the width of the microfluidic channel. In case of high Peclet numbers (Pe $\gg$ 1), convective effects are dominant and the depletion layer thickness δ can be approximated by $L(6\frac{L^2}{H^2}Pe)^{-1/3}$ [21] where H is the channel height and L is the sensor length (see Figure 1.6). For the diffusion constant of BSA, a flow rate of 5 µl/min and typical dimensions of a flow cell and ring resonator [7] (H = 50 µm, L = 15 µm and $W_{channel}$ = 200 µm), the Peclet number becomes 6624 and we can use the above-mentioned approximation for the depletion zone which then turns out to be around 1 µm thick. From the formula for the depletion zone thickness, it is also clear that an increase of the flow rate by a factor 1000 will only decrease δ by a factor 10. Diffusion of BSA molecules over this region of at most a few µm can take place in a matter of seconds, greatly improving the overall mass transport

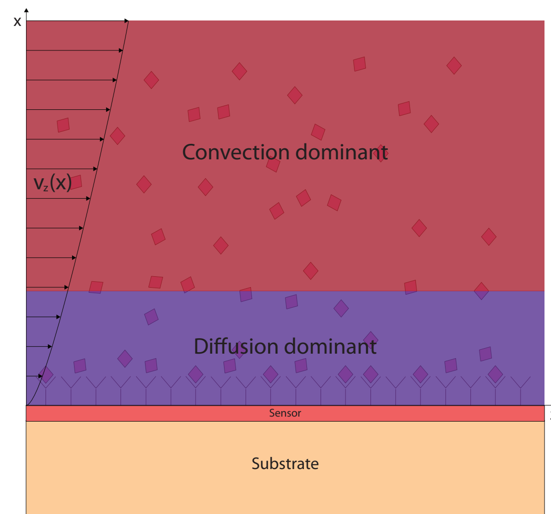

Figure 1.5: A developed, laminar flow between two parallel plates has a parabolic velocity profile. This implies that the velocity near the sensor surface is very small, compared to its maximum in the centre of the channel. A diffusion-dominated region develops near the sensor surface and a, much larger, convection-dominated region encompasses the rest of the channel. Note that not the entire channel is portrayed in the vertical direction so the convection dominated region is even larger.

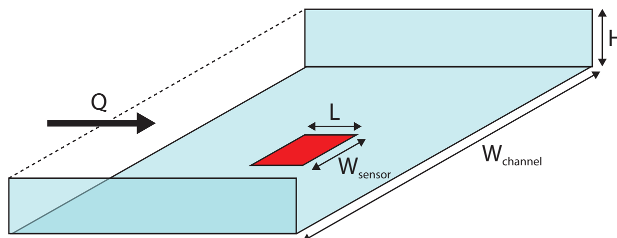

Figure 1.6: A biosensor of $W_{sensor} \times L$ is placed in a microfluidic channel of $W_{channel} \times H$. Although not visible in the figure, the top of the channel is also closed. A flow with rate Q containing target molecules is coming from the left, passing the sensor and exiting at the right.

compared to a case where only diffusion is responsible for mass transport.

However, up until now we have not made a distinction between high and low concentration analyte. Currently, there is a high demand for low concentration analyte detection [25] e.g. in early cancer detection [26]. For Pe $\gg$ 1, target molecules far from the sensor surface move too fast (due to convective effects) to get a chance at diffusing towards the sensor surface and they simply flow by without noticing the sensor. Only when the flow rate is sufficiently low (Pe = 1), the so-called *full collection* case can be achieved (i.e. convective and diffusive effects are balanced). Naturally, in a scheme where the flow is recycled, the molecules that pass the sensor without diffusing towards it are not wasted and get another chance at reaching the sensor in the next flow cycle. The total flux of target molecules reaching the sensor can be approximated as $J \approx Dc_0 W_{sensor}\mathfrak{F}$ where W_{sensor} is the sensor width and $\mathfrak{F}$ is the Sherwood number, a dimensionless flux, which can be approximated by L/δ [21]. To illustrate: the flux for a concentration c_0 = 10 fM gives a flux of 0.071 molecules/s. In other words, the time it takes between two molecules that reach the sensor is 14 s. In general, biosensors need several molecules to produce a detectable signal: for 100 biomolecules to bind to the sensor surface, we would have to wait over 23 minutes. Furthermore, when making these approximative calculations, we assumed that the laminar flow was able to replenish the target molecules that diffuse away towards the sensor. If in practice no mixing of biomolecules occurs in the direction normal to the sensor surface after recycling the flow, a situation might arise where there are no biomolecules present in the flow close to the sensor while there are still left near the top of channel. Due to the resulting concentration gradient, diffusion will occur but in view of the sometimes large channel dimensions, the biomolecules will take some time to diffuse towards the other side of the channel (i.e. the sensor side).

To overcome this problem for low-concentration analytes, several improved

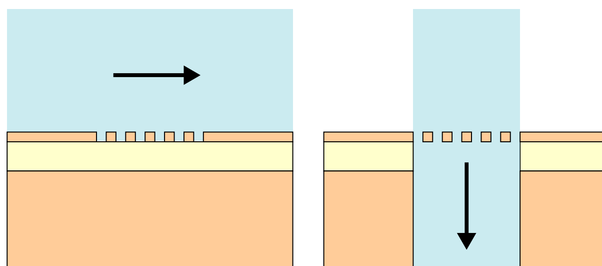

Figure 1.7: In conventional label-free biosensors, a microfluidic channel on top of the sensor guides the flow parallel to the sensor surface (left). In order to achieve more efficient mass transport, the flow can be directed through the biosensor, providing the biomolecules a better chance at binding with the receptor molecules on the sensor surface (right).

microfluidics configurations have been investigated [20]. Hofmann [27] proposes the introduction of a secondary flow that does not contain any target molecules and simply compresses the primary analyte flow. This is a more elegant solution than simply reducing the dimensions of the microfluidic channel since the required pressure to achieve a certain flow rate scales with H^3 where H is the channel height. Another technique, which we will focus on, is to direct the flow through the sensor by making use of a porous membrane. Lee and Yanavich [28] have filed a patent for a nanoporous membrane with pore diameter in the order of nanometres. The function of the membrane is twofold: on the one hand, the membrane is able to filter out certain molecules, based on size; on the other hand, the membrane acts as a substrate for receptor molecules to allow target molecules passing through the pores to bind. Although the patent only describes use in labelled biosensing, a similar technique can be used for label-free biosensing. Huang et al. [29] published their work on an optical label-free biosensor based on a photonic crystal (see Chapter 2). A photonic crystal basically denotes a broad family of optically periodic structures. By creating holes (the diameter of these holes depends on the optical characteristics of the materials used but is typically in the order of hundreds of nanometres; therefore, we refrain from using the term pores) in a light-guiding membrane, Huang obtained a similar structure to that of Lee and Yanavich: the photonic crystal can be employed as a label-free biosensor and the analyte flow is directed through its holes. A comparison between the conventional flow *over* the sensor and the flow *through* the sensor is illustrated in Figure 1.7.

Several months before Huang et al. [29] published their results, we started

working on a similar concept for optical biosensors. In Chapter 2 we will see that it is possible to design other optical label-free biosensors, that can have openings in close proximity to the sensitive surface through which fluid can flow, without compromising the sensor's functionality. Not only will we see that photonic crystals are not the only optical components that can be used to have a flow through the sensor, but the implementation of the flow is different in our case: consider a droplet of analyte on a biosensor with holes where we want the target molecules to bind at the walls of the holes (see Figure 1.8). In Chapter 4, we will see that gravity will not be able to sustain a flow by itself but that it is counteracted by surface tension of the liquid. However, it is possible to initiate a flow by creating a pressure gradient over the droplet: creating an underpressure at the bottom of the droplet will cause the analyte containing the target molecules to be sucked through the openings. In the case of a sufficiently low flow rate, the target molecules will have a chance at binding with the receptor molecules inside the holes. For high flow rates, the target molecules will pass too quickly and merely mix in the analyte. If we remove the pressure gradient, the droplet will be pending on the other side of the membrane (i.e. the bottom). Now, we can push the droplet back through the openings by applying an overpressure at the bottom and again, binding or mixing can occur. If we stop the pressure gradient after a certain time, the droplet will be on top of the membrane once again. We can repeat this cycle several times until we have sufficient bound target molecules or proper mixing has occurred. This concept has been demonstrated before by PamGene [30] in an application using different materials and length scales. The advantages over the work of Huang [29] is that there is no need to encapsulate the sensor in a flow cell, saving on packaging costs and improving reliability (due to the high pressures in microfluidics, some flow cells tend to leak after some time), and that small volumes can easily be used since they are applied directly on the sensor and don't need to be transported through channels where in some cases target molecules can stick to the walls. One drawback of this approach is that some information on binding kinetics, that is normally obtained through diffusion, is lost.

1.5 Thesis outline

In Chapter 2 we will give a state-of-the-art overview of available biosensors where we will focus on photonic sensors, and assess whether they are suitable for being used as a membrane with holes. This overview includes a more in-depth review of a novel sensing method using photonic crystals that was published in the course of this PhD work. Chapter 3 describes the fabrication process that we developed in our clean rooms to develop the above-mentioned membranes in a Silicon-on-Insulator (SOI) platform. A thorough explanation

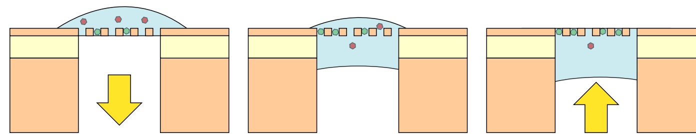

Figure 1.8: By applying underpressure at the bottom of the liquid droplet, the biomolecules are transported through the sensor membrane. The droplet can be pushed back by applying overpressure. This cycle can be repeated several times to ensure most biomolecules have bound in the membrane holes.

on each step in the process is given along with pitfalls and other possible options. A theoretical investigation of the microfluidics involved in transporting a droplet through a membrane with holes is given in Chapter 4 first. Then theory is compared to numerical simulations in order to determine the amount of pressure needed to obtain a certain flow rate. After that, measurement data is presented and discussed of a proof-of-principle experiment of a biosensor with a flow through a membrane. The fabrication process described in Chapter 3 can also be used to develop other components that can be useful in a complete biosensor or in a separate application. A first example is an optical pressure sensor described in Chapter 5: if we do not fully etch the silicon dioxide layer, we can create a thin, sealed membrane. Numerical and experimental data is given for a variety of photonic structures that can be employed as a pressure sensor. This component can be useful in an all-optical biosensor to obtain feedback on the amount of pressure that is exerted on a liquid droplet on a neighbouring sensor. Chapter 6 describes a second application: improving the coupling efficiency of fibre grating couplers. In conventional grating couplers, part of the coupled light is radiated towards the substrate. By etching away the silicon substrate locally and applying a metallic mirror on the silicon dioxide layer, the coupling efficiency can be improved. Conclusions of the work in this PhD and perspectives of this work are finally given in Chapter 7. Appendix A contains a summarised version of the process flow described in Chapter 3, along with all relevant parameters.

1.6 Publications

Patent applications

1. P. Bienstman, C. Lerma Arce and E. Hallynck. *Biosensing device.* US Provisional.

2. R. Baets, D. Vermeulen, D. Delbeke and E. Hallynck. *Method and system for coupling radiation.* US Patent 20110103743.

Publications in international journals

1. E. Hallynck and P. Bienstman. *Digital microfluidics with pressure-based actuation.* IEEE Photonics Technology Letters, submitted.

2. E. Hallynck and P. Bienstman. *Integrated optical pressure sensors in silicon-on-insulator.* IEEE Photonics Journal, 4(2):443–450, 2012.

3. E. Hallynck and P. Bienstman. *Photonic crystal biosensor based on angular spectrum analysis.* Optics Express, 18(17):18164–18170, 2010.

Publications in magazines

1. C. Lerma Arce, A. Goes, E. Hallynck, P. Dubruel, K. Komorowska, S. Van Put and P. Bienstman. *Reaktionsgefäße als neue Plattform für Sensoren mit nanophotonischen Silizium-Ringresonatoren.* BioPhotonik, 2, 2013.

Publications in international conferences

1. P. Bienstman, S. Werquin, C. Lerma Arce, D. Witters, R. Puers, J. Lammertyn, T. Claes, E. Hallynck, J.-W. Hoste and D. Martens. *Silicon Nanophotonics On-chip Sensing (invited).* PIERS 2013, to be published, Stockholm, Sweden, August 2013.

2. C. Lerma Arce, A. Goes, E. Hallynck, P. Dubruel, K. Komorowska, S. Van Put and P. Bienstman. *Reaction tubes as a platform for silicon nanophotonic ring resonator biosensors.* Integrated Photonics Research, Silicon and Nano-Photonics (IPR) OSA 2013, to be published, Rio Grande, Puerto Rico, July 2013.

3. P. Bienstman, S. Werquin, C. Lerma Arce, D. Witters, R. Puers, J. Lammertyn, T. Claes, E. Hallynck, J.-W. Hoste and D. Martens. *Nanophotonic biosensors in silicon-on-insulator (invited).* Transducers 2013, to be published, Barcelona, Spain, June 2013.

4. C. Lerma Arce, A. Goes, E. Hallynck, P. Dubruel, K. Komorowska, S. Van Put and P. Bienstman. *Silicon nanophotonic ring resonator sensors integrated in reaction tubes.* Photonics West 2013, 859801, San Francisco, CA, USA, February 2013.

5. P. Bienstman, S. Werquin, C. Lerma Arce, D. Witters, R. Puers, J. Lammertyn, T. Claes, E. Hallynck, J.-W. Hoste and D. Martens. *Ring resonator based SOI biosensors.* Photonics West 2013, 862905, San Francisco, CA, USA, February 2013.

6. E. Hallynck and P. Bienstman. *Integrated Differential Pressure Sensor in Silicon-on-Insulator.* IEEE Photonics Conference 2012, pages 445–446, Burlingame, CA, USA, September 2012.

7. E. Hallynck and P. Bienstman. *Photonic Crystal biosensor in spatial Fourier domain.* IEEE Photonics Conference 2011, pages 328–329, Arlington, VA, USA, October 2011.

8. E. Hallynck and P. Bienstman. *Photonic crystal biosensor based on angular spectrum analysis.* Annual Symposium of the IEEE Photonics Benelux Chapter, WeP16, Delft, The Netherlands, November 2010.

9. D. Vermeulen, K. Van Acoleyen, S. Ghosh, S. Selvaraja, W.A.D. De Cort, N.A. Yebo, E. Hallynck, K. De Vos, P.P.P. Debackere, P. Dumon, W. Bogaerts, G. Roelkens, D. Van Thourhout and R. Baets. *Efficient Tapering to the Fundamental Quasi-TM Mode in Asymmetrical Waveguides.* ECIO 2010, pages 161–164, Cambridge, United Kingdom, April 2010.

Publications in national conferences

1. E. Hallynck and P. Bienstman. *Photonic biosensor in the angular spectrum.* 11e UGent - FirW Doctoraatssymposium, page 128, Gent, Belgium, December 2010.

2. E. Hallynck and P. Bienstman. *Photonic crystal biosensing.* 10e UGent - FirW Doctoraatssymposium, Gent, Belgium, December 2009.

References

[1] PhRMA, *http://www.phrma.org/*.

[2] M. A. Cooper. *Optical biosensors in drug discovery.* Nature Reviews: Drug Discovery, 1(7):515–28, July 2002.

[3] M. Holgado, R. Casquel, and M.-F. Lagunas. *Label-free optical biosensor on a single chip.* SPIE Newsroom, pages 1–3, 2008.

[4] F. Patolsky, G. Zheng, O. Hayden, M. Lakadamyali, X. Zhuang, and C. M. Lieber. *Electrical detection of single viruses.* Proceedings of the National Academy of Sciences of the United States of America, 101(39):14017–22, September 2004.

[5] F. Barany. *Genetic disease detection and DNA amplification using cloned thermostable ligase.* Proceedings of the National Academy of Sciences of the United States of America, 88:189–93, January 1991.

[6] S. Hanash. *Disease proteomics.* Nature, 422:226–32, March 2003.

[7] K. De Vos. *Label-free Silicon Photonics Biosensor Platform with Microring Resonators.* PhD thesis, Ghent University, Ghent, 2010.

[8] X. Fan, I. M. White, S. I. Shopova, H. Zhu, J. D. Suter, and Y. Sun. *Sensitive optical biosensors for unlabeled targets: A review.* Analytica Chimica, 620:8–26, 2008.

[9] K. Länge, B. E. Rapp, and M. Rapp. *Surface acoustic wave biosensors: a review.* Analytical and Bioanalytical Chemistry, 391(5):1509–19, July 2008.

[10] R. M. Lequin. *Enzyme immunoassay (EIA)/Enzyme-linked immunosorbent assay (ELISA).* Clinical Chemistry, 51(12):2415–8, December 2005.

[11] E. Mylonakis, M. Paliou, M. Lally, T. P. Flanigan, and J. D. Rich. *Laboratory testing for infection with the human immunodeficiency virus: established and novel approaches.* The American Journal of Medicine, 109(7):568–76, November 2000.

[12] U. B. Nielsen and B. H. Geierstanger. *Multiplexed sandwich assays in microarray format.* Journal of Immunological Methods, 290(1-2):107–20, July 2004.

[13] V. Spiehler, D. S. Isenschmid, P. Matthews, P. Kemp, and T. Kupiec. *Performance of a microtiter plate ELISA for screening of postmortem blood for cocaine and metabolites.* Journal of Analytical Toxicology, 27:587–91, 2003.

[14] M. L. Phelan and S. Nock. *Generation of bioreagents for protein chips.* Proteomics, 3:2123–34, November 2003.

[15] P. Yager, T. Edwards, E. Fu, K. Helton, K. Nelson, M. R. Tam, and B. H. Weigl. *Microfluidic diagnostic technologies for global public health.* Nature, 442:412–8, July 2006.

[16] D. Psaltis, S. R. Quake, and C. Yang. *Developing optofluidic technology through the fusion of microfluidics and optics.* Nature, 442:381–6, July 2006.

[17] Elveflow, *http://www.elveflow.com/microfluidic-reviews-and-tutorials/review-microfluidic-for-cell-biology.*

[18] J. A. Ferguson, F. J. Steemers, and D. R. Walt. *High-density fiber-optic DNA random microsphere array.* Analytical Chemistry, 72:5618–24, November 2000.

[19] A. M. Armani, R. P. Kulkarni, S. E. Fraser, R. C. Flagan, and K. J. Vahala. *Label-free, single-molecule detection with optical microcavities.* Science, 317:783–7, August 2007.

[20] P. E. Sheehan and L. J. Whitman. *Detection Limits for Nanoscale Biosensors.* Nano Letters, 5(4):803–807, 2005.

[21] T. M. Squires, R. J. Messinger, and S. R. Manalis. *Making it stick: convection, reaction and diffusion in surface-based biosensors.* Nature Biotechnology, 26(4):417–26, April 2008.

[22] H. Bruus. *Theoretical Microfluidics.* Oxford University Press, 2008.

[23] A. Fick. *Über Diffusion.* Annalen der Physik, 170(1):59–86, 1855.

[24] R. R. Walters, J. F. Graham, R. M. Moore, and D. J. Anderson. *Protein diffusion coefficient measurements by laminar flow analysis: method and applications.* Analytical Biochemistry, 140:190–5, July 1984.

[25] L. M. Bellan, D. Wu, and R. S. Langer. *Current trends in nanobiosensor technology.* Wiley interdisciplinary reviews: Nanomedicine and nanobiotechnology, 3(3):229–46, 2011.

[26] S. Shah, Y. Liu, and W. Hu. *Characterization of Biosensor Detection Process at Ultra-Low Concentration Through a Stochastic Particle Model.* In ASME Conference Proceedings, pages 13–14, 2010.

[27] O. Hofmann, G. Voirin, P. Niedermann, and A. Manz. *Three-Dimensional Microfluidic Confinement for Efficient Sample Delivery to Biosensor Surfaces. Application to Immunoassays on Planar Optical Waveguides.* Analytical Chemistry, 74:5243–5250, 2002.

[28] G. U. Lee and C. Yanavich, *Nanoporous membrane immunosensor.* US Patent 20040126899.

[29] M. Huang, A. A. Yanik, T.-Y. Chang, and H. Altug. *Sub-wavelength nanofluidics in photonic crystal sensors.* Optics Express, 17(26):24224–24233, December 2009.

[30] PamGene, *http://www.pamgene.com/*.

"No, it isn't strange: after changes upon changes we are more or less the same."

Paul Simon in The Boxer, Musician, 1941-present

2

Sensor types

As mentioned in Chapter 1, we would like to design a biosensor where the amount of molecules bound to the sensor surface is translated into a change in the optical properties of the medium close to the centre, specifically the refractive index (RI), which we then can measure. In this chapter, we will focus on the photonic structures that are able to measure such a change in refractive index and assess whether they are suitable for being used as a membrane with holes. We will not go in-depth on all varieties of a certain type of sensor but instead refer to [1] for a more complete overview.

2.1 Surface plasmon resonators

After being demonstrated first by Liedberg [2], surface plasmon resonance (SPR) based sensors have been extensively investigated in literature [3–6] and also find applications in industry [7–13]. Surface plasmon polaritons are electromagnetic waves that travel along the interface between a metal and a dielectric. They can propagate on condition that the real part of the dielectric constant of the metal is negative and that its absolute value is greater than the real part of the dielectric constant of the dielectric, which has to be positive (this follows from the surface plasmon polariton condition in equation (2.1)).

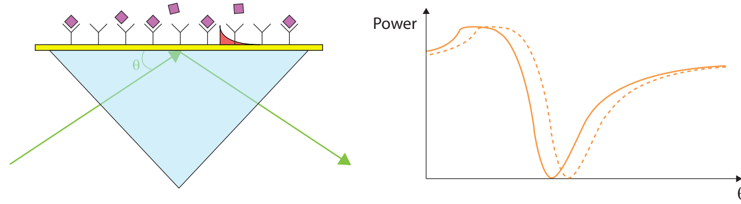

Figure 2.1: Working principle of a surface plasmon resonance based sensor with coupling prism in the Kretschmann configuration. Light at a certain wavelength is coupled in while scanning the angle of incidence. For a certain angle, light will couple to the surface plasmon wave and will not be reflected (solid line in right figure). The angle at which this occurs will change once biomolecules have attached to the metallic surface (dashed line).

$$\begin{aligned} \Re(\epsilon_{dielectric}) \cdot \Re(\epsilon_{metal}) &< 0 \\ |\Re(\epsilon_{dielectric})| &< |\Re(\epsilon_{metal})| \end{aligned} \tag{2.1}$$

Most commonly, a configuration as shown in Figure 2.1 is used: over a certain range of angles, monochromatic light is sent to the metallic layer through a coupling prism. For a certain angle of incidence, surface plasmon resonance will occur. Since the incident power is then coupled to the surface plasmon wave, no output intensity is observed for that angle. When biomolecules bind to receptor molecules on the metallic layer, the refractive index near the metallic-bio-interface will change, along with the resonance condition. In practice, this means that the intensity drop will occur for a different angle. This shift in resonant angle can be used to quantify the amount of refractive index change and the binding of biomolecule can be quantitatively deduced from this. It is also possible to work at a fixed angle and scan a range of wavelengths to see a resonance dip.

When looking at industrial applications, it is clear that surface plasmon resonance is, at the time of writing, the preferred sensing scheme, with the first commercialised SPR-based sensor developed by Biacore [7]. While the general principle remains the same, manufacturers try to differentiate themselves by working on better multiplexing capabilities, improved flow mechanisms, better chemistry or other parameters. In academia, on the other hand, improvements are also still proposed; an interesting example that is relevant to this work, is described in an article on surface plasmon resonance sensing by Brolo [14]: nanoholes are created in the metallic layer to improve the flow characteristics of the sensor.

Surface plasmons can also be excited without a coupling prism as e.g. demonstrated by Debackere [3] who integrated a SPR sensor in a Silicon-on-Insulator (SOI) chip with a limit of detection (LOD) of 10^{-3} refractive index unit (RIU). He et al. [15] demonstrated a detection of 10 pM DNA using SPR with signal amplification using gold particles. A SPR sensor excited using two light emitting diodes (LEDs) achieved a LOD of 2×10^{-5} RIU according to Suzuki [16]. Multiplexed detection has been demonstrated by e.g. Dostalek [17] with a LOD of 5×10^{-7} RIU in 120 channels. It is also possible to integrate a SPR sensor on an optical fibre where e.g. the fibre cladding is locally removed and a thin metallic layer is deposited on the fibre core, allowing for interaction between the evanescent tail of the light and the metallic surface [18].

Based on [14], we could investigate whether creating nanoholes in the metallic layer of an integrated SPR based sensor in SOI can increase the flow efficiency at little performance cost. However, we have chosen to focus on devices that are more easily mass fabricated and are more performant (see following).

2.2 Mach-Zehnder interferometers

The working principle of a Mach-Zehnder interferometer (MZI) is based on the interference between two lightwaves of equal wavelength where one of the waves has undergone a phase delay $\Delta\phi$ as given by equation (2.2):

$$\Delta\phi(\lambda) = \frac{2\pi}{\lambda}\left(\int^{arm_2} n_{eff}(r,\lambda)\mathrm{dr} - \int^{arm_1} n_{eff}(r,\lambda)\mathrm{dr}\right) \tag{2.2}$$

Here, λ is the wavelength of the incident light and $n_{eff}(r,\lambda)$ is the local effective index. Depending on the amount of phase delay (induced by e.g. a different refractive index medium or optical path length), the waves will (partially or completely) interfere constructively or destructively. This is illustrated in Figure 2.2. When used in biosensing applications, generally one arm of the MZI is shielded from the biomolecules as binding of biomolecules to both arms would induce no net phase change (provided that the physical length of the arms is the same). In applications, the phase change can be quite small and at a phase delay where the output intensity is maximal (and the derivative is very small), a small phase change is not easily detected. It is therefore more practical to scan a certain wavelength range since in equation (2.2) we see that the phase change $\Delta\phi$ depends on the wavelength λ. From Figure 2.3 it is clear that, since we have more information, it will be easier to determine small phase changes. Mach-Zehnder interferometers can be constructed in bulk optics, using mirrors and beam splitters, but can also be easily integrated in SOI with a very small footprint. This will be highlighted further in Chapter 4.

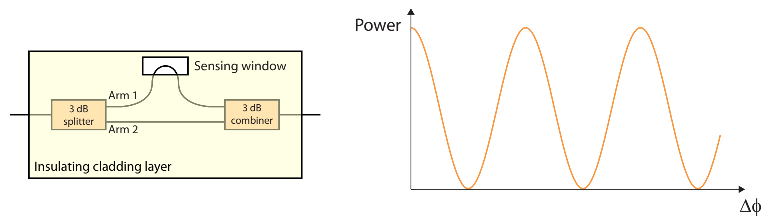

Figure 2.2: Working principle of a Mach-Zehnder interferometer (MZI). A lightwave is split into two paths. The output intensity after combining both lightwaves again depends on the phase difference $\Delta\phi$ between the two waves. When used in biosensing applications, generally one arm of the MZI is shielded from the biomolecules as binding of biomolecules to both arms would induce no net phase change.

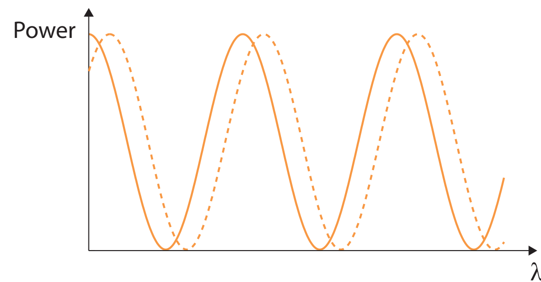

Figure 2.3: When scanning a certain wavelength range, more information is obtained. A mathematical fit can partially filter out measurement noise and as a consequence increase accuracy. Due to binding of biomolecules to one sensing arm, the output spectrum will change (solid to dashed line).

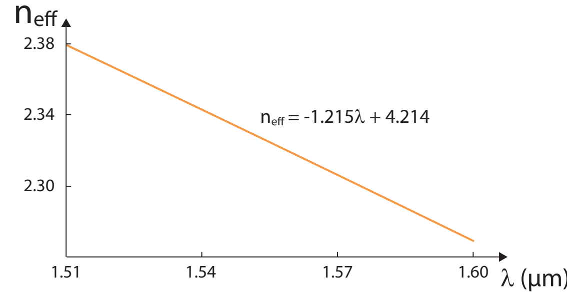

Figure 2.4: Effective index of the first order TE mode of a 450-nm-wide SOI strip waveguide with top water cladding. Going from 1.51 μm to 1.60 μm, the effective index changes by 10^{-1} RIU. Neglecting second order dispersion, we can fit a linear curve with the formula n_{eff} = -1.215λ [μm] + 4.214.

In order to partially filter out noise and increase accuracy during measurements, it is advised to fit a mathematical model to the measurement data. In the following, we will derive a formula that links the output intensity to the wavelength of the incident light. Furthermore, we will derive a formula for the sensitivity of such a sensor (the amount of wavelength shift due to a marginal increase in effective index due to biomolecule binding).

Before we derive a formula for sensitivity we should note that, as we will see later, we have to take into account the group index as defined here:

$$n_g = n_{eff} - \lambda \frac{\partial n_{eff}}{\partial \lambda} \tag{2.3}$$

Figure 2.4 shows an effective index calculation using *COMSOL Multiphysics* [19] for the first order transverse electric (TE) mode of a 450-nm-wide SOI strip waveguide with top water cladding. We see that SOI waveguides are highly dispersive and this effect can not be neglected. Neglecting second order dispersion, we can fit a linear curve to the simulation results, yielding $\frac{\partial n_{eff}}{\partial \lambda}$ = -1.215 $\frac{1}{\mu m}$.

Assuming the refractive index in the neighborhood of the first arm is changed, we get the equations from (2.4) when differentiating the phase in both arms.

$$\begin{aligned}
\mathrm{d}\phi_1 &= \tfrac{\partial\phi_1}{\partial\lambda}\mathrm{d}\lambda + \tfrac{\partial\phi_1}{\partial n_{bio}}\mathrm{d}n_{bio} \\
&= \tfrac{-2\pi}{\lambda^2}\left(n_{eff,bio}(\lambda)L_{1,bio} + n_{eff,clad}(\lambda)L_{1,clad}\right)\mathrm{d}\lambda + \\
&\quad \tfrac{2\pi}{\lambda}\left(\tfrac{\partial n_{eff,bio}(\lambda)}{\partial\lambda}L_{1,bio} + \tfrac{\partial n_{eff,clad}(\lambda)}{\partial\lambda}L_{1,clad}\right)\mathrm{d}\lambda + \\
&\quad \tfrac{2\pi}{\lambda}L_{1,bio}\tfrac{\partial n_{eff,bio}}{\partial n_{bio}}\mathrm{d}n_{bio} \\
&= -\tfrac{2\pi}{\lambda^2}L_{1,clad}n_{g,clad}\mathrm{d}\lambda - \tfrac{2\pi}{\lambda^2}L_{1,bio}n_{g,bio}\mathrm{d}\lambda + \tfrac{2\pi}{\lambda}L_{1,bio}\tfrac{\partial n_{eff,bio}}{\partial n_{bio}}\mathrm{d}n_{bio} \\
\mathrm{d}\phi_2 &= \tfrac{\partial\phi_2}{\partial\lambda}\mathrm{d}\lambda \\
&= \tfrac{-2\pi}{\lambda^2}\left(n_{eff,clad}(\lambda)L_{2,clad}\right)\mathrm{d}\lambda + \tfrac{2\pi}{\lambda}\left(\tfrac{\partial n_{eff,clad}(\lambda)}{\partial\lambda}L_{2,clad}\right)\mathrm{d}\lambda \\
&= -\tfrac{2\pi}{\lambda^2}L_{2,clad}n_{g,clad}\mathrm{d}\lambda
\end{aligned} \tag{2.4}$$

where $L_{1,bio}$ is the length of the MZI arm that is exposed to the biomolecules and $L_{x,clad}$ is the length that is covered by a cladding layer.

During measurements, we monitor the shift of e.g. a minimum or maximum meaning that we track a point in the spectrum for which the phase difference is unchanged. This gives us the condition $\mathrm{d}\Delta\phi = 0$ or $\mathrm{d}\phi_1 = \mathrm{d}\phi_2$. Inserting equation (2.4) into this condition yields equation (2.5) for the sensitivity S.

$$S = \frac{\mathrm{d}\lambda}{\mathrm{d}n_{bio}} = -\frac{\lambda\frac{\partial n_{eff,bio}}{\partial n_{bio}}L_{1,bio}}{n_{g,clad}(L_{2,clad} - L_{1,clad}) - n_{g,bio}L_{1,bio}} \tag{2.5}$$

It can be shown [20] that the free spectral range (FSR), which is the spacing between consequent minima or maxima, of an MZI can be approximated by the following equation:

$$FSR = \frac{\lambda^2}{n_{g,clad}(L_{2,clad} - L_{1,clad}) - n_{g,bio}L_{1,bio}} \tag{2.6}$$

Inserting this into (2.5) gives equation (2.7) for the sensitivity.

$$S = -\frac{FSR\frac{\partial n_{eff,bio}}{\partial n_{bio}}L_{1,bio}}{\lambda} \tag{2.7}$$

From the above formula, it is clear that increasing the free spectral range of the interferometer or increasing the window where biomolecules can bind the sensitivity will increase. Also note that the sensitivity is inversely proportional to the wavelength.

We will now derive a formula for the intensity in function of the wavelength. We start with a guided mode with intensity I_0 and excite the two arms of the MZI using a 3 dB-splitter. After both resulting waves have travelled their optical paths, they reach a 3 dB-combiner. The resulting intensity formula can be calculated:

$$
\begin{aligned}
I_{out}(\lambda) &= \left| \frac{1}{\sqrt{2}}\sqrt{\frac{I_{in}}{2}} e^{-jk\phi_1(\lambda)} + \frac{1}{\sqrt{2}}\sqrt{\frac{I_{in}}{2}} e^{-jk\phi_2(\lambda)} \right|^2 \\
&= \frac{I_{in}}{2}\left(1+\cos(\Delta\phi(\lambda))\right)
\end{aligned}
\quad (2.8)
$$

Note that $\Delta\phi(\lambda)$ is not only wavelength-dependent through the factor $\frac{2\pi}{\lambda}$ but also through the effective index $n_{eff_{1,2}}(\lambda)$. If the data fit is performed over a large wavelength range, first order dispersion can again not be neglected. In that case, the effective index can be approximated by a linear function as in Figure 2.4. In case higher order dispersion has to be taken into account, a Taylor series around the wavelength where a minimum occurs can be used.

If we want to create a sensitive MZI based biosensor, according to equation (2.7), we need a long waveguide that is able to capture biomolecules. To implement this, we can make use of so-called delay spirals: folded up waveguides in a spiral pattern that exhibit a long optical waveguide length in a relatively small footprint. In the case of strip waveguides, a number of waveguides next to each other are separated by a silicon dioxide trench. If we etch this silicon dioxide, we create a membrane with trenches through which we can have a flow. This is further discussed in Chapter 4.

Mach-Zehnder interferometers have been shown to be able to detect refractive index changes of 10^{-7} RIU [21]. Prieto [22] has achieved a LOD of 2×10^{-5} RIU using an anti-resonant reflecting optical waveguide (ARROW) in silicon dioxide. In silicon nitride Schipper [23] reported a LOD of 10^{-4} RIU using a standard Mach-Zehnder interferometer.

2.3 Ring resonators

A ring resonator is a resonant structure frequently used in integrated photonics [24]. Its working principle can be intuitively explained by stating that resonance occurs when the wavelength of the coupled light fits an integer number of times in the optical path length of the ring; a standing wave is then created giving rise to resonance. This is illustrated by equation (2.9) where λ_{res} is the resonant wavelength, $n_{eff}L$ is the optical path length of the mode in the ring and m is a strictly positive integer.

$$\lambda_{res} = \frac{n_{eff}L}{m} \quad (2.9)$$

A more physical explanation is illustrated in Figure 2.5: part of an incident wave is coupled to the ring through the cross-coupling coefficient κ. The other part passes through after been multiplied by the self-coupling coefficient r. Both coefficients obey (in an ideal, lossless case) the condition $\kappa^2 + r^2 = 1$. Inside the ring, the wave amplitude is multiplied by a factor $a = \exp(-\frac{\alpha}{2}L)$ where L

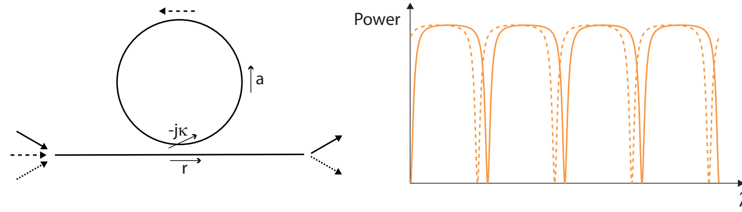

Figure 2.5: In a ring resonator, the amplitude of the wave at the output port can be considered as an infinite sum of waves that have passed through the ring once up to an infinite number of times. The output spectrum seen in the right can shift when the refractive index near the ring changes (e.g. due to biomolecules binding; solid to dashed line).

is the ring length and α the power attenuation coefficient. Initially, rE_{in} will be transmitted to the output, $(-j\kappa)E_{in}$ is coupled to the ring. After a round trip in the ring, part of this wave will couple back to the output waveguide but part will pass another time through the ring. It is clear that the amplitude of the wave at the output port can be considered as an infinite sum of waves that have passed through the ring once up to an infinite number of times. This is mathematically formulated in (2.10) where ϕ is the phase shift βL obtained after one round trip.

$$\begin{aligned}
E_{out} &= rE_{in} + (-j\kappa)ae^{-j\phi}(-j\kappa)E_{in} + (-j\kappa)ae^{-j\phi}rae^{-j\phi}(-j\kappa)E_{in} + \\
&\quad (-j\kappa)ae^{-j\phi}rae^{-j\phi}rae^{-j\phi}(-j\kappa)E_{in} + \ldots \\
&= rE_{in} - \kappa^2 ae^{-j\phi}\left(1 + \left(rae^{-j\phi}\right) + \left(rae^{-j\phi}\right)^2 + \ldots\right)E_{in} \\
&= rE_{in} + \frac{(r^2-1)ae^{-j\phi}}{1-rae^{-j\phi}}E_{in} \\
&= \frac{r-ae^{-j\phi}}{1-rae^{-j\phi}}E_{in} \\
&\Downarrow \\
\frac{I_{out}}{I_{in}} &= \frac{a^2+r^2-2ar\cos\phi}{1+(ra)^2-2ar\cos\phi}
\end{aligned} \tag{2.10}$$

It can be shown that the resonant dips in the transmission spectrum (defined as the ratio $\frac{I_{out}}{I_{in}}$) can be approximated by Lorentzian peaks according to formula (2.11), where R_{min} is the transmission at resonance, $FWHM$ is the full-width at half-maximum and λ_{res} is the resonant wavelength [25]. We will use this approximation when fitting a model to our measurement data.

$$T_{dip}(\lambda) \approx \frac{R_{min}\left(\frac{FWHM}{2}\right)^2 + (\lambda - \lambda_{res})^2}{\left(\frac{FWHM}{2}\right)^2 + (\lambda - \lambda_{res})^2} \tag{2.11}$$

It is also useful to determine the sensitivity of this sensor, as we did for the

MZI based biosensor. For this, we start from equation (2.9) and differentiate it. We obtain:

$$d\lambda = \frac{dn_{eff}L}{m} \tag{2.12}$$

When the refractive index of the environment surrounding the ring changes, the effective index will change and as a consequence the resonance wavelength. However, since we are working in dispersive waveguides, a change in resonance wavelength will also change the effective index. This is illustrated in equation (2.13).

$$d\lambda = \frac{\left(\frac{\partial n_{eff}}{\partial n_{bio}} dn_{bio} + \frac{\partial n_{eff}}{\partial \lambda} d\lambda\right) L}{m} \tag{2.13}$$

Inserting (2.9) and (2.3) into this equation yields equation (2.14).

$$S = \frac{d\lambda}{dn_{bio}} = \frac{\frac{\partial n_{eff}}{\partial n_{bio}} \lambda}{n_g} \tag{2.14}$$

As is the case for MZI based biosensors, it is also possible to make use of folded waveguide structures in the case of ring resonators so this type of sensors is also suitable for underetching and using as a silicon membrane with openings for a vertical flow.

Ramachandran [26] has demonstrated a ring resonator based sensor in glass that was able to detect 500 nM of a sequence of 25 base pairs of the genome of the bovine viral diarrhea virus. A polymer-based ring resonator was fabricated by Chao [27] and had a detection limit of 10^{-7} RIU. In our group, Katrien De Vos [28] has designed a SOI ring resonator with a detection limit of 10^{-5} RIU. She was later able to show multiplexed detection with these sensors using an infrared camera [29]. In the industry, currently, Genalyte [30] is the only company that makes use of ring resonators as transducers. More detailed information on ring resonators can be found in the PhD works of Tom Claes [25] and Katrien De Vos [31].

2.3.1 Vernier ring resonators

The ring resonator discussed above is the component used in its simplest form. Many other configurations containing multiple rings in e.g. a cascade or in combination with an MZI are possible and have been demonstrated [32, 33]. One of these configurations that will be discussed shortly in Chapter 5 is two rings in a Vernier configuration. The principle is very similar to the Vernier scale found on e.g. micrometers or a calliper: by using two scales with a slightly different spacing (i.e. FSR), increased precision can be achieved. For ring resonators,

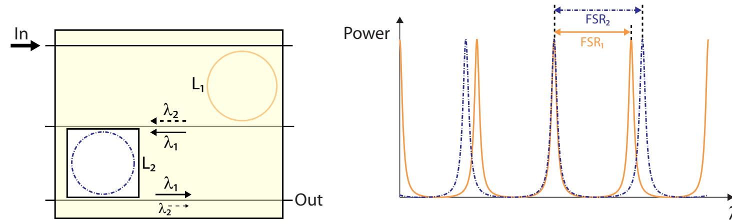

Figure 2.6: Broadband light is coupled in the top waveguide. When overlapping both transmission spectra of the slightly different rings, it is clear that one peak will, in theory, be completely transmitted while others will be attenuated. For a small shift in one of the ring spectra, a larger shift in the overall transmission spectrum can be obtained.

this is illustrated in Figure 2.6. In the previous section, we observed the so-called pass spectrum: a uniform spectrum with transmission dips on wavelength positions where resonance occurs. It is also possible to extract a so-called drop port spectrum from a ring resonator by adding a coupled waveguide elsewhere close to the ring. This spectrum will consist of a zero transmission spectrum save for places where resonance occurs in the form of Lorentzian peaks. Coupling broadband light (i.e. larger than the FSR of the smallest ring) into the first ring results in a drop port transmission spectrum. Consider now two wavelengths λ_1 and λ_2 (represented by a solid and dashed arrow in Figure 2.6 (left)), one of which is also a resonant wavelength for the second ring (here the solid arrow, λ_1). Because the FSR of the second ring is different than that of the first one, the other resonant wavelength (dashed arrow, λ_2) will be off resonance (with only small overlap between the two peaks), resulting in overall lower transmission. Consider that the sensing ring shifts by an amount $FSR_2 - FSR_1$ to the left due to a change in refractive index in its surroundings: the overall transmitted peak (after passing the two ring resonators) will have shifted by FSR_1 to the right, meaning an amplification of the shift. Another added benefit is that, if both rings are subject to common noise (e.g. thermal variations), this effect is not amplified because both their spectra will shift equally. In a similar way, bulk refractive index changes in biosensing can be filtered out when only one of the rings is chemically functionalised [25].

The explanation above is for Vernier sensors used in the discrete regime. It is clear that the LOD of the sensor is limited by the FSR of the reference ring. This case occurs when the difference in FSR between the two rings is larger than the FWHM of the resonance peaks. A Vernier sensor can also be used in a continuous regime where we do not simply look at the hopping of a peak but looking at the overlap between several peaks. This regime occurs when the FWHM of the

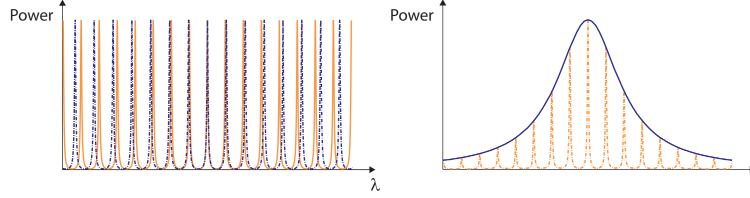

Figure 2.7: When the FWHM is larger than the difference in FSR between the two rings, we use the Vernier sensor in the continuous regime where we monitor the shift of an envelope signal. Although not visible in this figure, peak splitting will occur in the resulting spectrum where the two constituent peaks only overlap weakly.

peaks is larger than the difference in FSR. In this case, the shift of an envelope function is monitored as is illustrated in Figure 2.7. For two peaks with weak overlap, peak splitting will occur in the resulting spectrum.

Since we can achieve a better LOD in the continuous regime, we will use Vernier sensors in this configuration in the following chapters. It can be shown that the envelope function from Figure 2.7 can be fit to formula (2.15) [25].

$$T_{envelope}(\lambda) = \left(\frac{\sqrt{T_{max}} \left(\frac{FWHM_{envelope}}{2\sqrt{\sqrt{2}-1}} \right)^2}{\left(\frac{FWHM_{envelope}}{2\sqrt{\sqrt{2}-1}} \right)^2 + (\lambda - \lambda_{central})^2} \right)^2 \tag{2.15}$$

The enhanced sensitivity can be formulated by equation (2.16) where $P_{envelope}$ is the period of the envelope signal, given by the ratio of the product of the two FSRs to their difference.

$$S = \frac{\mathrm{d}\lambda}{\mathrm{d}n_{bio}} = \frac{\frac{\partial n_{eff,sensor}}{\partial n_{bio}} \lambda}{n_{g,sensor}} \frac{P_{envelope}}{FSR_{sensor}} \tag{2.16}$$

The PhD work of Tom Claes [25] provides more in-depth information about Vernier ring resonators, as well as experimental data on such sensors, fabricated in SOI. It is shown that a sensitivity of 2170 nm/RIU can be achieved, compared to 76 nm/RIU for a regular ring resonator. Furthermore, it is interesting to note that Vernier-cascade sensors exhibit an improved LOD over ring resonators [25]. Jin [34] has also published a Vernier-based sensor with a sensitivity of 1300 nm/RIU, below that of Claes [25]. In a recent article published by La Notte [35], a Vernier-configuration with a ring resonator and Mach-Zehnder interferometer is presented with a sensitivity of over 1000 µm/RIU.

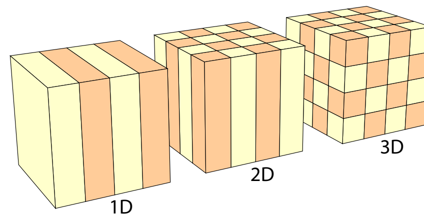

Figure 2.8: Photonic crystals can have periodicity in 1, 2 or 3 dimensions.

At the time of writing, no commercial applications make use of this improved sensing scheme using ring resonators.

2.4 Photonic crystals

An interesting photonic structure that is also a candidate for being used as a biosensor is a photonic crystal (PhC) [36, 37]. Photonic crystals are basically structures that exhibit a periodic variation of the refractive index. This periodicity can occur in 1D, 2D or 3D as illustrated in Figure 2.8. Since 3-dimensional photonic crystals are in general quite difficult to fabricate and do not fit in our rationale to integrate the biosensor with other photonic components, we will not investigate this type of photonic crystals further.

Photonic crystals are interesting structures in the sense that they can, on the one hand, be implemented for many applications (e.g. sensing [38–40], lasing [41–43], filtering [44–46]) but are, on the other hand, notoriously sensitive to fabrication errors. They exhibit their interesting properties due to their periodic structuring. However, small errors or variations in this periodicity are sometimes detrimental for their quality. Since the features of a photonic crystal are commonly sub-wavelength scale, it comes as no surprise that Deep UV lithography is not the most suitable option for fabricating very small PhCs and most of them are fabricated using e-beam lithography, a process not suitable for mass fabrication. With the advance of Extreme UV lithography, it would be possible to create higher quality photonic crystals in the future, although e.g. grating couplers, an example of more fabrication tolerant photonic crystals, can already be made using current technology.

In the following, we will provide a short overview of different types of photonic crystal based biosensors found in literature. In section 2.4.4, we propose a novel, hybrid sensing method using photonic crystals by monitoring light in the angular spectrum. Section 2.4.5 describes part of the master thesis work done by Oliver Willekens about the superprism effect in photonic crystals [47]. We will only shortly touch upon the theory of photonic crystals and refer the

reader to the excellent book of Joannopoulos [48] on this matter. For a review on photonic crystal based biosensors, we refer to Zhao [49].

2.4.1 Band edge detection

Undoubtedly, one of the most interesting properties of photonic crystals is the band gap. Consider a uniform medium through which light is traveling in the z-direction so that $k_z = k$. Light will obey the dispersion relation as given in equation (2.17) and will have a waveform e^{-jkz}.

$$\omega(k) = \frac{ck}{n} \tag{2.17}$$

If we now perturb this uniform medium with a refractive index variation, the wavefunction will have to obey Bloch's theorem which basically states that the waveform in a periodic medium, with period a, is also periodic with the same periodicity, save for a phase factor. Mathematically formulated this gives:

$$\vec{E}(z+a) = e^{-jka}\vec{E}(z) \tag{2.18}$$

It can be proven [48] that the only relevant wavenumbers k are located in the so-called first Brillouin zone ranging from $-\frac{\pi}{a} \leq k \leq \frac{\pi}{a}$. The information of other wavenumbers can be deduced from this range due to the periodic nature of the medium. Consider a mode with $k = \frac{\pi}{a}$: the wavelength will be $\lambda = \frac{2\pi}{k} = 2a$. Note that, due to Bloch's theorem, the phase shift after one period a will be -1. Looking at Figure 2.9, in the uniform medium there are no conditions on the position of the waveform since the medium is invariant. There is one solution for ω, given by equation (2.17) and the plotted band diagram is continuous (although folded back, according to a 'virtual' period a in order to compare to the periodic medium). However, looking at the right part of Figure 2.9, we see that for that wavenumber, two solutions for ω can be found and a gap with forbidden frequencies arises, the so-called band gap. The reason for this can be explained as follows: due to symmetry arguments, the peaks of the electric field have to be situated in either the centre of the low refractive index or high refractive index part of the medium. It can be shown [48] that modes concentrated in a region with high refractive index have a lower frequency than modes concentrated in a low refractive index. Since here we are dealing with this discontinuity between possible positions of the waveform, we also have a discontinuity in the possible frequencies. The gap here is relatively large since the index contrast is high. For a low index contrast, the gap would be smaller.

Going back to the field of biosensing we could argue that it is possible to make a biosensor out of photonic crystals by allowing one of the refractive indices to change due to either a bulk change in refractive index or due to binding

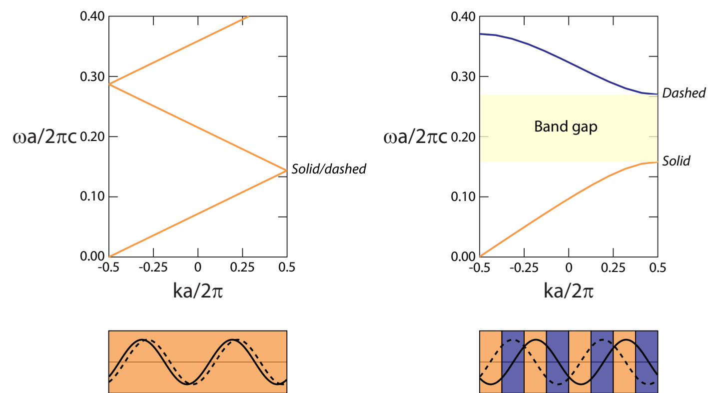

Figure 2.9: On the left we see the band diagram for a uniform medium with $n = 3.476$. Wavenumbers higher than 0.5 have been folded back in order to compare to the periodic medium on the right where $a = 0.5$ and n alternates between 1 and 3.476. For $\frac{ka}{2\pi} = 0.5$ ω can only take one value in the uniform medium due to continuous translational invariance. In the periodic medium, due to symmetry arguments, the peaks of the electric field have to be located in either the centre of the low refractive index or high refractive index part of the medium. Due to this discontinuity, two possible solutions for ω are possible.

of biomolecules where only a thin layer near the sensor surface changes refractive index. By measuring the amount of shift of the band edges (i.e. the edges of the band gap), we know the amount of change in refractive index. In an article by Xiao [50], this idea is discussed for 2D photonic crystals. We have looked further into this for the case of a 2D photonic crystal slab (a structure where the mode in-plane is determined by the photonic crystal and is in the vertical direction confined through index guiding, i.e. determined by the light line; see Figure 2.10) and have found out that there are three general ways to increase the sensitivity for a 2D photonic crystal:

- **Monitor the high frequency band**
  From the above discussion we know that the lower frequency mode is concentrated in the high refractive index region and the higher frequency mode in the low refractive index medium. Only the low refractive index medium changes in our case (the high refractive index medium is silicon ($n = 3.476$)). It is therefore clear that a mode should be chosen that is concentrated in the low refractive index medium, i.e. the higher frequency mode.

- **Increase the hole radius**
  This is intuitively quite clear since expanding the fraction of the low refractive index medium will increase interaction between the mode and the varying refractive index. In practice, the diameter can not be increased indefinitely since fabrication limitations have to be taken into account.

- **Excite along the ΓM direction**
  In a 2D photonic crystal slab with triangular lattice, the irreducible Brillouin zone is defined by Γ, K and M. The two most interesting directions are therefore the ΓM and ΓK directions (see Figure 2.10). Why exactly the ΓM direction is more sensitive than the ΓK direction is not fully understood but the difference is only small compared to the difference between e.g. sensing with the low and high frequency mode.

Figure 2.11 shows the transmission spectra of a photonic crystal slab (with thickness $0.4a$ and hole diameter $0.6a$) excited along the ΓM direction, once with a refractive index of 1.3 in the holes and as cladding layers and once with an index of 1.4. These results were obtained through a widely used 3D Finite Difference Time Domain (FDTD) simulation tool called *MEEP* [51]. These results have been confirmed by calculating the band diagram of the photonic crystal using *MPB* [52]. We can transform the normalised frequency $\frac{\omega a}{2\pi c} = x$ to a wavelength λ through $\frac{a}{x} = \lambda$. The shift when only the refractive index in the holes changes is

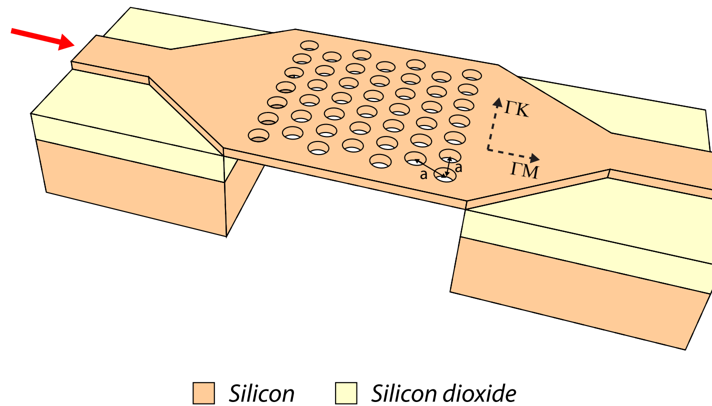

Figure 2.10: An example of a 2D photonic crystal slab. The mode is confined in the vertical direction through index guiding and is in the horizontal direction determined by the photonic crystal. The air holes are arranged in a triangular lattice with lattice constant a. All other parameters (e.g. slab thickness, hole diameter) are usually described relative to this constant.

25.1 nm; when also the refractive index of the cladding layers changes, the shift amounts to 40 nm.

A drawback of this approach, as will become apparent in Chapter 4, is that in practice, band edges are seldom very well defined (i.e. infinite slope) and they are not always easy to detect with great precision.

2.4.2 Defect based devices

Up until now, we have always spoken of bulk photonic crystals: a uniform, periodic refractive index variation. It is possible to introduce a defect in a photonic crystal by e.g. removing one row of holes in a matrix of holes [53, 54] or reducing the diameter of one or several holes [40, 55, 56]. In the former type, generally a waveguide mode is created inside the band gap of which the evanescent tail overlaps slightly with the bulk PhC. The latter type, where a localised defect is introduced, can support modes that, in theory, cannot escape from the defect cavity thus creating a powerful resonator. In the transmission spectrum, this will show up as a Lorentzian peak inside the band gap of the bulk photonic crystal. Changing the refractive index near the defect causes the resonance peak to shift which is normally easier to detect than e.g. the shift of a band edge.

Two examples of 2D photonic crystal slabs with defects (top view) are shown

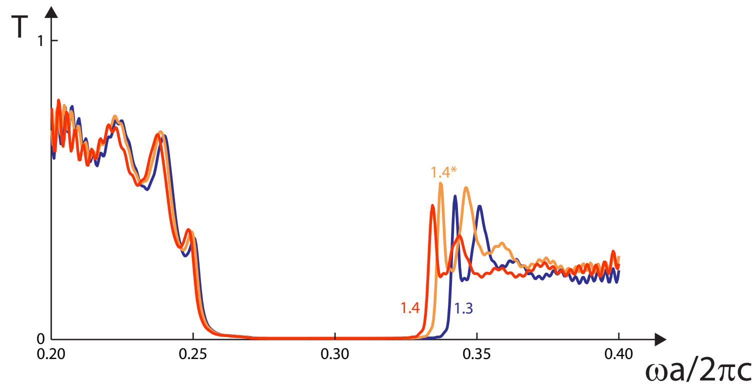

Figure 2.11: A triangular lattice 2D photonic crystal slab with thickness 0.4a and hole diameter 0.6a is excited along the ΓM direction. When changing the refractive index in the holes and cladding layers (i.e. above and below the photonic crystal) from 1.3 to 1.4, we see a 40-nm shift of the upper band edge. The graph 1.4* is a calculation where only the refractive index in the holes changes from 1.3 to 1.4. The shift in this case is 25.1 nm.

in Figure 2.12. Note that in the illustrating band diagrams, the light cone is plotted since it accounts for the vertical light confinement in the photonic crystal slab. One of the first sensors published was one by Chow [57] with a structure similar to the one seen at the top of Figure 2.12, that was able to detect a RI shift of 2×10^{-3} RIU. Skivesen [58] presented a PhC with a W1 waveguide defect (W1 denotes a waveguide defect where one row of holes is removed; see bottom of Figure 2.12) where the cut-off wavelength of the waveguide mode was used as a spectral feature that was monitored. The reported sensitivity was 66 nm/RIU and they were able to detect a concentration of 10 μg/ml Bovine Serum Albumin (BSA).

2.4.3 Resonant gratings

The previous two sections, where we elaborated on both bulk and defect PhCs, always dealt with light modes mainly outside of the light cone. There are other modes that extend considerably more in the light cone so light guided by the PhC can couple to the continuous spectrum of free space modes; these are called guided-mode resonances [59]. A commonly used configuration is illuminating a 2D PhC slab with light under an angle θ. For a certain combina-

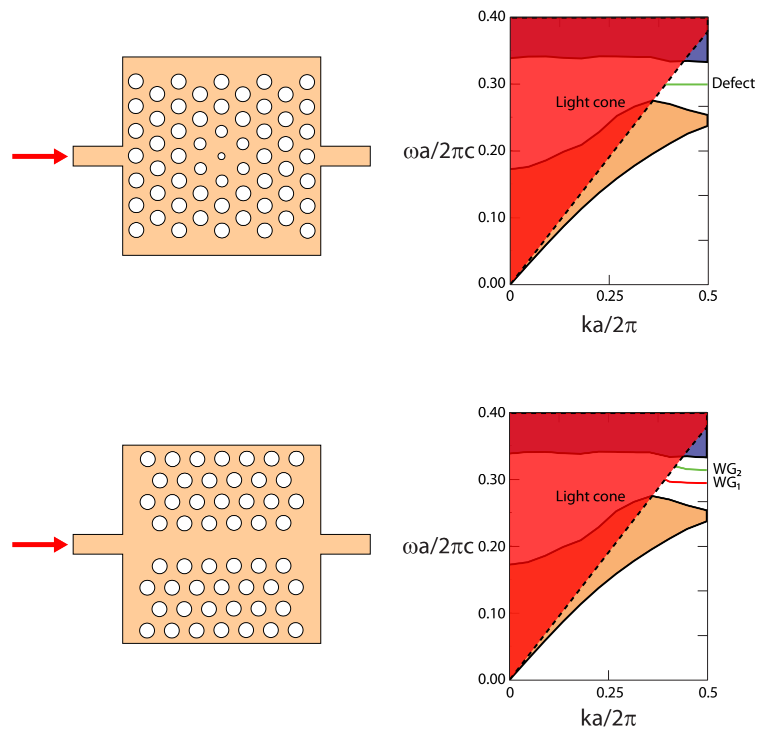

Figure 2.12: At the top is a PhC with a point defect, similar to a structure used by Chow [57]. The bottom structure shows a PhC with a waveguide defect (W1; where the one denotes that one row of holes has been removed), as demonstrated by Skivesen [58].

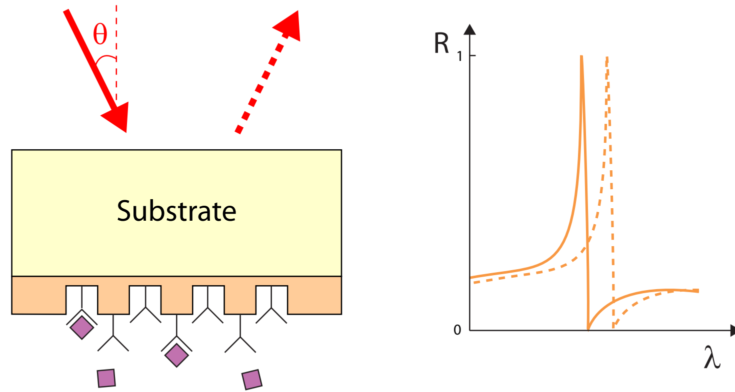

Figure 2.13: Incident light on a photonic crystal can couple to guided resonance modes. This will show up as a peak in the wavelength spectrum and is called a Fano resonance.

tion of wavelength λ and angle θ, a guided resonance will be excited in the PhC slab. This will show up in the reflection spectrum as a sharp asymmetric resonance with a Fano shape. Changing the refractive index properties of the PhC will cause a shift of this resonance peak.

Huang [38] has demonstrated a sensitivity of 510 nm/RIU for a photonic crystal slab where the flow is passed through the photonic crystal holes, in similar way to what we will try to prove in this work. El Beheiry [60] has done extensive simulation work on these types of sensors. Cunningham [61] has demonstrated a reflective grating where the shift of a narrowband wavelength spectrum is monitored with which it is possible to detect 0.0167 nM of BSA. Due to the fact that light is coupled in and out off the chip, it is very easy to create this kind of sensor for multiplexed detection [62].

2.4.4 Angular spectrum sensing

The previous overview of biosensor types shows that a lot of research has been done over the years. Here we present a novel sensing method, that also makes use of the above mentioned guided resonances: incident light comes in in the plane of the PhC and is then coupled out of the plane, much like a grating coupler (see Figure 2.14). The results of this have been published [63].

2.4.4.1 Angular spectrum analysis sensor concept and simulation methods

As was the case for resonant gratings, the proposed structure makes use of guided resonances. Figure 2.15 shows the transmission, reflection and radiated

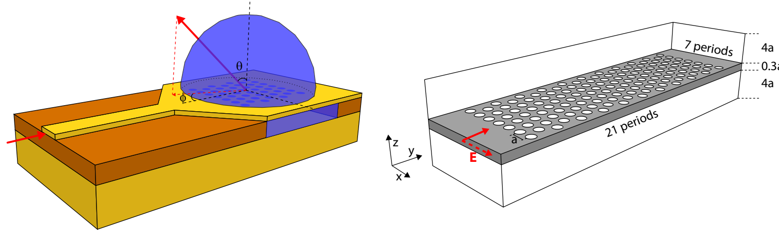

Figure 2.14: Light enters the PhC biosensor by means of a waveguide and is coupled to free space as a beam with inclination θ and azimuth ϕ (left). The simulated structure used for FDTD simulations is shown in the right figure. All sizes are normalised to the lattice constant a. The grid resolution used is 56 pixels per unit of distance.

(either upwards or downwards since the structure is symmetric) flux spectra of a $0.3a$ thick bulk silicon PhC slab comprising holes of diameter $0.8a$ in a triangular lattice (where a is the lattice constant), excited with TE- or x-polarised light in the ΓM direction (see Fig. 2.14 (right)). The refractive index in the holes as well as that of the cladding layers above and below the PhC slab is 1.33, the refractive index of water. The resolution is set to 56 pixels per unit of distance. Simulations are carried out using the already mentioned FDTD software *MEEP*. Instead of performing several simulations, each at a different frequency, we did one simulation with a Gaussian pulse profile in the time domain and Fourier transformed the results afterwards in order to obtain a Gaussian profile in the frequency spectrum. Note that the sum of the flux spectra does not equal 1 as the flux planes defined in our simulations do not constitute a closed volume (the flux plane for out-of-plane radiation is located at a relatively large distance from the slab and the flux planes for reflection and transmission only cover the input waveguide).

In Figure 2.15 we see a clearly marked frequency region of interest bound by dips in the out-of-plane radiated flux. In order to determine what exactly is happening in this region, we must examine the fields themselves. Fig. 2.16 shows the calculated angular spectrum of the Poynting vector (defined in equation (2.19)) projected on the vertical direction for a certain frequency in the region of interest.

$$P_z = \Re(E_x H_y^* - E_y H_x^*) \tag{2.19}$$

We can distinguish the Lorentzian shape which we would expect to see due to the resonant coupling of guided modes to free space modes [64]. As with other diffraction gratings, the angle at which a beam with a certain frequency is radiated, is determined by the momentum matching condition. The angular posi-

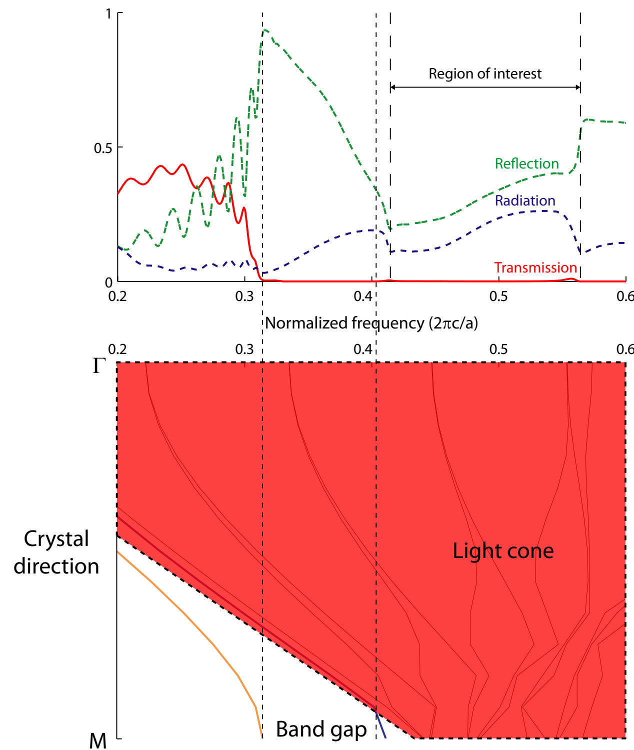

Figure 2.15: In a certain frequency region, above the light line, guided modes can couple to free space modes. The fluxes shown in this figure are calculated for a triangular silicon PhC slab with hole diameter 0.8a, thickness 0.3a, excited in the ΓM direction. The radiation flux represents either the down- or upward direction since the structure is symmetric. Below is a band diagram, calculated using MPB, showing that the calculated band gap is the same for both simulation methods.

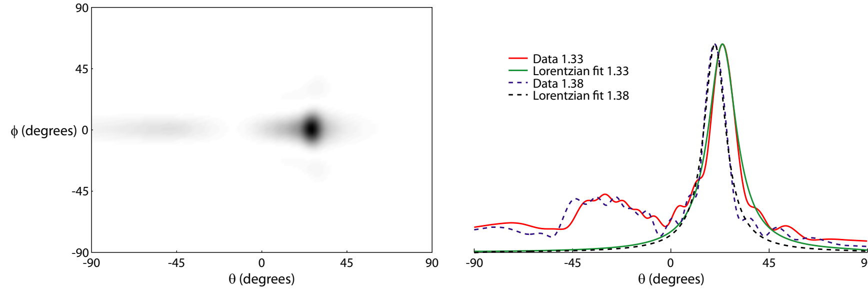

Figure 2.16: The angular spectrum (left) and cross-section at ϕ=0° (right) of the vertically projected Poynting vector of the proposed structure with a symmetric cladding (i.e. refractive index above and below PhC slab equals that of the holes) at normalised frequency 0.53488. A Lorentzian resonance shape is clearly visible.

tion of the peak shifts not only in function of frequency but also due to changes in refractive index which makes it interesting for sensing applications.

There are a lot of parameters that can be tuned when designing this structure. In the following, we will discuss some of the most important of these parameters: the type of cladding configuration and the direction of light excitation.

2.4.4.2 Different cladding configurations

Depending on fabrication and implementation of microfluidics [5, 38], one can wonder how the refractive index in the neighbourhood of the PhC membrane will change. Therefore, we have studied the three main situations that can arise:

- only the refractive index in the PhC holes changes and above and below the membrane, there is air (henceforth called the *no cladding* type)
- one cladding layer consists of air while the other has the same refractive index as that of the holes (*asymmetric cladding*)
- both cladding layers and holes experience a change in refractive index (*symmetric cladding*)

For each of these situations, simulations have been carried out for several refractive indices which allows us to determine a shift per RIU.

There are two ways to see a kind of shift: we can look at the angular spectrum for a fixed frequency by using a spatial Fourier measurement setup [65, 66] or we measure the power for a given angle while scanning the frequency range. Both methods have been investigated and the results for the different cladding

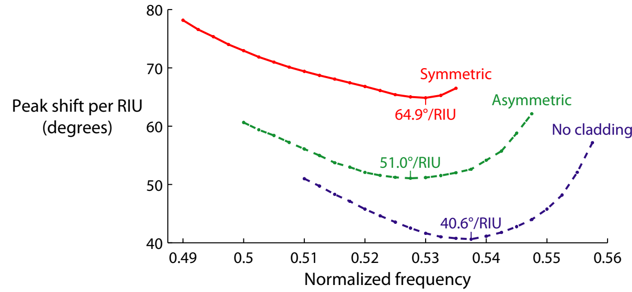

Figure 2.17: The angular shift in °/RIU is given for a set of fixed frequencies and the three different cladding configurations. The shift is highest for the configuration where the refractive index changes everywhere (i.e. *symmetric cladding*).

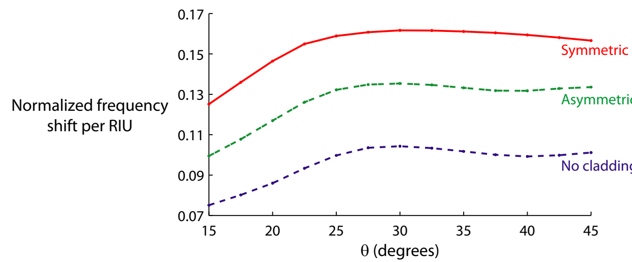

Figure 2.18: It is also possible to use this sensor at a fixed angle, while scanning a range of frequencies. Again, the shift for the *symmetric cladding* configuration is the highest.

configurations are presented in Figures 2.17 and 2.18 respectively. It should however be noted that the major advantage of the first method is that the light source in a fabricated device only needs to be single frequency.

Like we would intuitively expect, for both measurement methods, the *symmetric cladding* type is more sensitive than the *asymmetric cladding* configuration which is in turn more sensitive than the *no cladding* type. When measuring using the Fourier setup, it is advised to measure at a high frequency because a) the light is coupled out at an angle close to the normal and is therefore easier to capture using a lens and b) as will become apparent in what follows, the width of the resonance peak decreases with increasing frequency.

Using the other measurement method, we see for the three types a gradual increase in sensitivity with increasing angle until it becomes stable at about 25° and onwards.

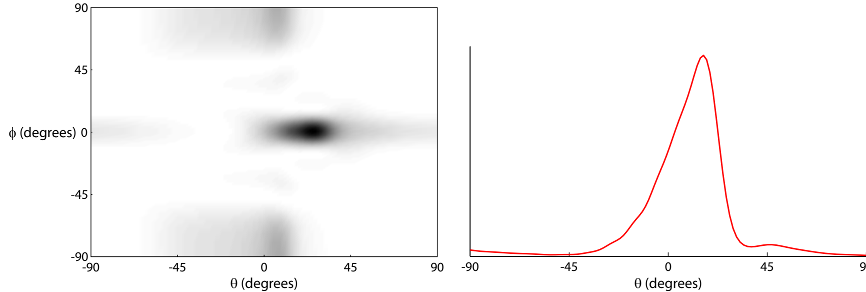

Figure 2.19: The angular spectrum at normalised frequency 0.53488 (left) and cross-section at ϕ=0° and normalised frequency 0.569 (right) of the proposed structure with a symmetric cladding. A portion of the light is scattered under an angle ϕ=90° and the Lorentzian shape is distorted (this is more clearly visible in the right figure).

2.4.4.3 Excitation along the ΓK direction

Up until now, we have always excited light in the PhC along the ΓM direction. Exciting it along the perpendicular ΓK direction gives a slightly different angular spectrum as shown in Figure 2.19.

We can see that the Lorentzian shape is distorted (more clearly visible in the right part of Figure 2.19) and that now also light is scattered at an angle ϕ=90°.

As it is difficult to fit a proper Lorentzian to the ΓK spectra we can make an estimation of the shift by simply observing the maxima of the peaks. It turns out that the sensitivity is roughly equal to that of the structure excited in the ΓM direction.

2.4.4.4 Other parameters

It is clear that there are still a lot of other properties that can be optimised (e.g. the shape of the unit cell, slab thickness, polarization of incident light, the periodic lattice). We have investigated the effect of the number of periods in the direction of light propagation but have found that it is of little influence. The hole diameter has been chosen sufficiently large as to maximise the light-matter interaction keeping in mind technological limitations for eventual fabrication of the device (i.e. minimal distance between adjacent holes). The influence of the slab thickness has been investigated briefly and we have found that with decreasing thickness, the frequency region in which the Lorentzian shape appears widens and shifts to higher frequencies and the sensitivity also slightly increases.

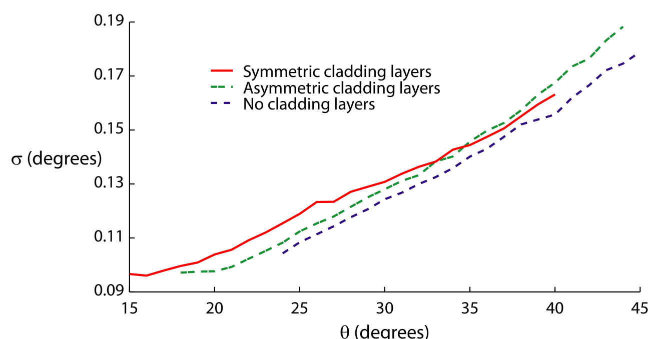

Figure 2.20: Adding noise in Monte Carlo simulations causes the spread σ on correct peak detection (left). Since the spread increases with the angle θ, it is advised to work at small angle θ.

2.4.4.5 Noise analysis and limit of detection

In simulations, it is virtually impossible to take into account all noise factors that will influence measurements (e.g. temperature variations, fabrication errors). In order to already make some predictions on how the structure will react due to this noise, we can add Gaussian noise to the simulated signal. By performing a Monte Carlo simulation, i.e. repeatedly determining the peak position of a noise-ridden signal, it is possible to determine the spread on the calculated peak position: by fitting a Gaussian distribution to the determined peak positions we extract the spread σ. This spread is in turn a measure for the LOD. Measurements of other structures using our Fourier measurement setup have shown, on average, a signal-to-noise ratio (SNR) of 22 dB. The amplitude of the added noise in the Monte Carlo simulation is therefore chosen as to reach the same SNR.

Figure 2.20 leads us to conclude that the spread σ is practically independent of the cladding configuration (variations are due to numerical and statistical errors) but above all, we can say that the spread increases with the angle θ. As already mentioned above, it is therefore interesting to work at a high frequency, which is at small angle θ, close to the normal to the PhC membrane.

Instead of looking at the sensitivity, a more commonly used figure of merit is the LOD which is defined here as $\sigma/shift$. Figure 2.21 shows the LOD in function of the frequency for the Fourier setup measurement method. As expected, the LOD is lowest for high frequencies due to the small peak width at these frequencies. If we would be able to increase the SNR of the measurement setup, the LOD could also improve. Simulations have shown that the LOD is linearly related to the noise amplitude.

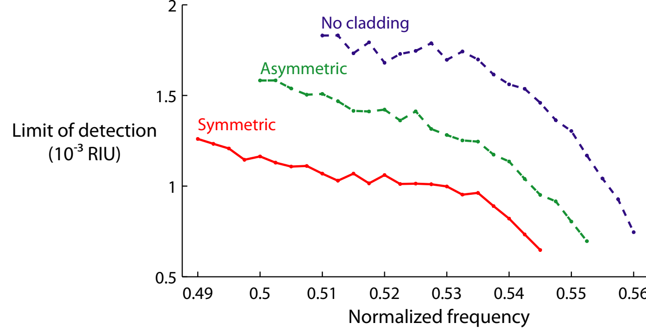

Figure 2.21: Using the calculated spread σ in function of the angle θ, we can calculate the LOD (considering the worst case/largest σ of the shifted peaks). The LOD is smallest at a high frequency as this is where the angle θ is smallest.

2.4.5 Superprism effect

The superprism effect [48] is a phenomenon that can be observed in certain photonic crystals where an incident beam of light is refracted under an angle that can be far greater than what is expected by e.g. Snell's law. Kosaka [67] has demonstrated a beam refracted by the superprism effect going from -70°to +70°by changing the angle of incidence from -7°to +7°. The angle of refraction is dependent on both the photonic crystal properties and properties of the incident light (i.e. angle, polarisation and wavelength). Changing the refractive index in the photonic crystal holes therefore changes the angle of refraction. This effect can be used to create a biosensor [47, 68] (see also Figure 2.22). To determine the angle under which refraction occurs, we make use of the fact that the direction in which energy propagates is determined by the group velocity, $\nabla_{\vec{k}}\omega$. Assuming k_z=0 (i.e. in-plane propagation), we can construct a 3D space with axes (k_x,k_y,ω). Since 2D diagrams are easier to study, usually a cross-section at one frequency is taken (a so-called isofrequency contour; see Figure 2.23).

To find the band gap in a photonic crystal, it is only necessary to calculate the eigenmodes at the edge of the irreducible Brillouin zone (which is in the case of a 2D photonic crystal slab with triangular lattice defined by Γ, K and M); in order to construct isofrequency contours, it is necessary to discretise this entire zone which increases simulation time significantly. Instead of using a uniformly discretised grid, it is advised to make use of a non-uniform grid that is denser at the edges of the irreducible Brillouin zone since variations in the band diagrams are largest there. Once the 3D space with all combinations of (k_x,k_y,ω) is calculated, we can determine the angle of refraction in the photonic crystal as follows (see also Figure 2.23):

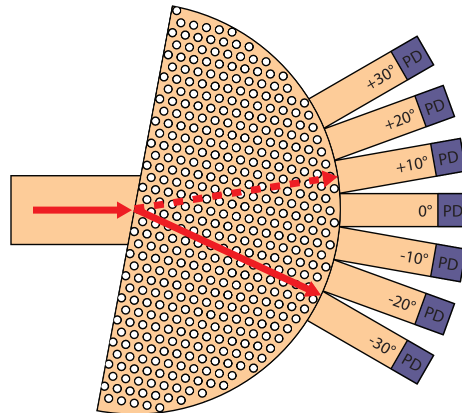

Figure 2.22: The concept of using the superprism effect for biosensing is illustrated here. For a small change in refractive index, large refraction angle differences can arise.

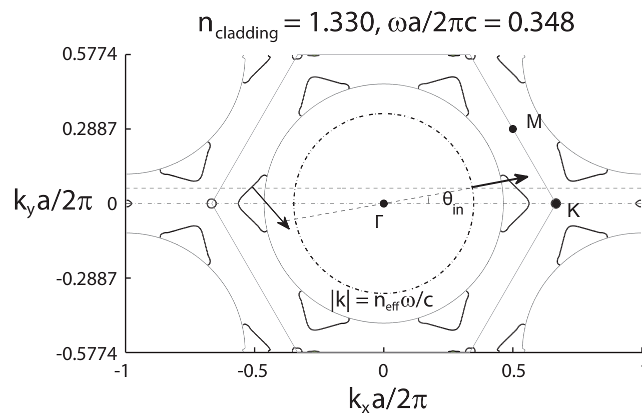

Figure 2.23: An example of an isofrequency contour is shown from [47] where the incident medium is assumed to be air ($n_{eff} = 1$). On horizontal lines, the wavevector parallel to the photonic crystal interface is conserved.

1. Consider an incident wave coming form a uniform medium with effective index n_{eff}. In this case, the dispersion relation in function of (k_x,k_y,ω) is given by a conical shape with its length axis along the direction of ω so a cross-section for a given frequency produces a circle. Therefore, we construct a circle with radius $n_{eff}\omega/c$ where c is the speed of light in vacuum. The angle of the incident light with respect to the photonic crystal can then be visualised as shown in Figure 2.23 by drawing a diameter through the centre of the circle at the correct angle (in this case an angle θ with respect to the ΓK direction of the photonic crystal).

2. Since we are assuming linear behaviour, the refracted light will be defined by the same isofrequency contour as the incident light. Due to conservation of the wave vector, parallel to the photonic crystal interface (in this case $\vec{k}_{||} = k_y$), we can construct a horizontal line through the intersection point of the incident angle diameter and the incident light cone mentioned in the previous step. The intersections of this line with the isofrequency contour are points of interest. It should be noted that, since we are working with a waveguide slab structure, we have to take into account the light cone defined by the highest refractive index of the cladding layers. Eigenmodes inside the light cone are not confined and are therefore not considered further.

3. By calculating the group index $\nabla_{\vec{k}}\omega$, which is perpendicular to the isofrequency contour in the direction of increasing ω [48], we can determine the angles of the refracted waves. Note that some points of interest do not represent valid refracted waves: waves directed towards the incident light source are not valid (unless they are reflected waves) since we have assumed that there are no light sources in the photonic crystal.

Interesting regions in isofrequency contours are usually those with sharp angles since there, a small change in refractive index, incident angle or wavelength is translated into a relatively large shift of the angle of refraction. Due to the shape of these contours, the angular shift in function of the refractive index is not always linear and it is difficult to define a sensitivity as we have done for e.g. MZI based sensors or ring resonators. However, it is possible to define linear subregions in a function that shows the refraction angle in function of the refractive index with theoretical sensitivities up to 6566°/RIU [47].

In practice, it is necessary to make use of a broad access waveguide in order to minimise the angular spread of the incident beam. Combined with the fact that the longer the beam can propagate, the higher the detection resolution will be, this implies the need for a large photonic crystal: Kosaka [67] demonstrated the superprism effect using a 500 µm × 500 µm photonic crystal (which was not optimised for biosensing applications)while the photonic crystal used by

Chow [57] measured approximately 10 μm × 5 μm. Not only does this greatly increase the footprint of our sensor (compromising multiplexing abilities on one chip) but this will also decrease the mechanical robustness of an underetched photonic crystal as will be further touched upon in Chapter 3.

2.4.6 Conclusions

From the above overview, which only highlighted some of the most common uses of photonic crystals, it is clear that a photonic crystal is a very versatile structure. On the other hand, as already mentioned in the beginning of this section, since their strength arises from the periodicity, small fabrication errors can have a significant impact on the PhC performance. Consider a 2D PhC with hole diameter 500 nm: small variations, even in the order of nanometres, disturb the perfect periodicity of the unit cell and degrade e.g. the band gap quality. As will become clear in later chapters, non-uniform stress in a photonic crystal also causes perturbations due to the elasto-optic effect (i.e. stress changes the refractive index locally).

When looking at photonic crystals from a mechanical point-of-view one could argue that a 1D PhC (i.e. a Bragg grating) bares resemblance to e.g. a delay spiral in an MZI. Comparing this to a 2D photonic crystal with holes in a silicon slab, we intuitively would expect the latter to be a more rigid structure when underetched.

2.5 Other sensor types

Apart from the sensor types discussed here, there are other types of photonic based sensors and electrical or mechanical based sensors. For the sake of completeness, we will shortly discuss fibre-based sensors and some other photonic structures (e.g. Young's interferometer) and give some examples of electrical and mechanical sensors.

2.5.1 Photonics

Optical fibres are a key element in photonics and can be manufactured quite cheaply. A commonly used method is to define a Bragg grating (i.e. a 1D photonic crystal) in the fibre core by holographic techniques, producing Fibre Bragg gratings (FBGs) (see Figure 2.24 (top)). These types of fibres are already well established in other sensing fields like strain [69] or temperature sensing [70] or a combination of several physical properties [71]. It comes as no surprise that this type of sensors has also been deployed in biosensing applications. Liang [72] has reported a sensitivity of 71.2 nm/RIU with a LOD of 1.4×10^{-5} RIU for a fibre

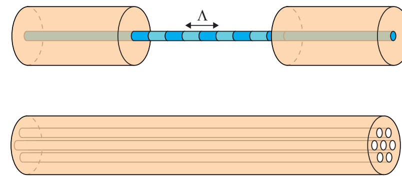

Figure 2.24: The top figure shows a Fibre Bragg grating as proposed in e.g. [72, 73]. At the bottom we see an example of a photonic crystal fibre [75].

etched down to its core (≈ 3 µm). Chryssis [73] has reported a sensitivity of 1394 nm/RIU with a LOD of 7.2×10^{-6} RIU, with a similar device. Variations on the standard design of FBGs are possible as shown by Caucheteur [74] who demonstrated enhanced refractive index sensitivity using tilted FBGs with a high refractive index coating. Another type of photonic crystal fibre is illustrated in Figure 2.24 (bottom). The photonic crystal is defined in the same plane as the fibre cross section and extruded along the fibre's longitudinal axis. Hu [75] has demonstrated a photonic crystal fibre for streptavidin and biotin detection, achieving a sensitivity of 320 nm/RIU. A third technique is introducing a Fabry-Perot cavity in the fibre (through etching or splicing) where the resonances will shift due to a refractive index change in the cavity. This has been, for example, demonstrated by Wei [76] who achieved a sensitivity of 1163 nm/RIU and a LOD of 1.1×10^{-6} RIU. Fortébio [77] produces a commercial biosensor based on a Fabry-Perot cavity at the tip of a fibre. Also worth mentioning is a ring resonator integrated on an optical fibre that was demonstrated in our group [78], achieving the same sensitivity as a ring resonator on a chip.

Apart from optical fibres, there are still other optical techniques not yet discussed in the above. To conclude we will briefly touch on two examples: the first one is a Young interferometer where light is split up in a reference and sensing arm but contrary to a Mach-Zehnder interferometer, the light is not combined at the end but coupled to a Coupled Charge Device (CCD) camera where the interference pattern is recorded and analysed. Ymeti was able to demonstrate a LOD of 6×10^{-8} RIU [79] with such a structure. A second technique is backscattering interferometry: a coherent light beam impinging on a sensor containing small (i.e. sub-wavelength) structures cause interference between the different scattered waves. A detector measures the intensity and according to binding of biomolecules or a refractive index change, the intensity (as a consequence of a phase shift) will change. Wang [80] has reported a LOD of 10^{-9} RIU. As mentioned in the introduction of this chapter, there are still other sensor types for which we refer to a review paper by Fan [1].

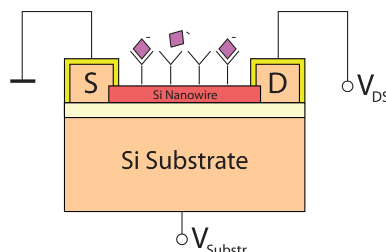

Figure 2.25: Operating principle of a silicon nanowire based metal-oxide-semiconductor field-effect transistor (MOSFET) as a biosensor. Where the conducting channel is normally controlled by the electric field caused by a gate voltage, charged molecules binding to the nanowire channel can similarly induce an electric field controlling the conductance.

2.5.2 Electronics

One of the more recent electronic biosensors makes use of the basic component in microelectronics, i.e. a metal-oxide-semiconductor field-effect transistor (MOSFET). Consider a standard nMOS (the reasoning for a pMOS is analogous). The drain and source are n-doped regions in a p-type silicon substrate. Above the channel between the two n-doped islands is a gate electrode, separated from the silicon by oxide (a dielectric). By considering the drain-source voltage to be zero and by increasing the gate voltage, holes are repulsed and an n-channel is created through which electrons can travel. The transistor works in its triodic or ohmic region and has a certain conductance. Increasing the drain-source voltage will cause the channel to pinch off at a certain point and the transistor goes into saturation.

The triodic mode is of particular interest here because it can be modelled as a resistor (with a certain conductance) in that case, relating the channel current to the drain-source voltage. A silicon nanowire based MOSFET biosensor (see Figure 2.25) replaces the gate electrode by a functionalised p-type nanowire. When electrically charged molecules bind to this nanowire, they create an electric field and behave as a gate electrode, changing the conductance which can be easily measured. Since the silicon nanowires can have a diameter of 2-3 nm [81, 82], the biosensor can be made very sensitive, up to the point where a single influenza virus can be detected [83]. Before the advance of nanowires, a similar concept called an ion-sensitive field-effect transistor (ISFET) was proposed by Bergveld [84] where a reference electrode, acting as a gate electrode, had to be immersed in the solution for stable operation.

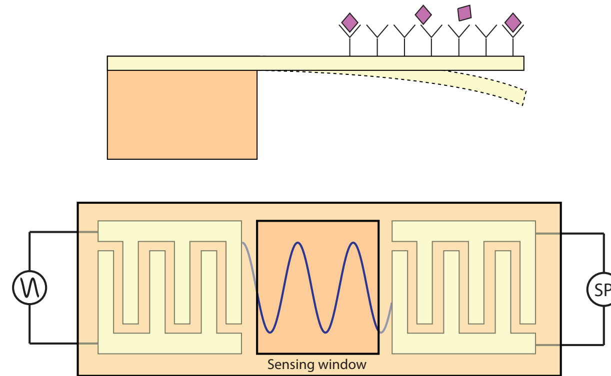

Figure 2.26: The top figure shows a microcantilever that bends because of the added mass of adsorbed biomolecules. This bending or other induced changes in the microcantilever structure are a measure for the amount of biomolecules. The bottom figure shows the concept of a surface acoustic wave (SAW) based sensor. Alternating current (AC) drives interdigitated electrodes, creating a SAW. The properties of this wave can be changed due to biomolecule binding. The SAW is transduced back into an electrical signal after which signal processing (SP) takes place.

2.5.3 Mechanics

Microcantilevers (see Figure 2.26 (top)) can be used to measure a.o. temperature, mass and stress changes and can also be deployed as biosensors. When biomolecules bind to the cantilever surface, stress will be induced in the cantilever as well as a change in resonance frequency, due to mass loading [85]. Measuring this deflection or stress can be done by using several techniques: measuring the piezoresistivity, the capacitance or the deflection of an optical beam are among the most popular read-out methods. Companies like Concentris [86] or Protiveris [87] have commercialised such sensors.

Another type of mechanical sensors makes use of surface acoustic waves (SAWs). These waves are created by driving interdigitated electrodes on a substrate with alternating current (AC) (see Figure 2.26 (bottom)): because the polarity between neighbouring electrodes will be opposite, the stress created in the substrate will alternate from tensile to compressive. This creates a mechanical wave at the substrate surface with a frequency dependent on the electrode spacing. The mechanical wave can be transduced back into an electrical signal by a similar set of electrodes. If the acoustic wave travels along a functionalised surface, it can react to binding of biomolecules by a change in phase, amplitude

or frequency. A review on SAW-based sensors can be found in [88].

2.6 Conclusions

We have given an overview of the most common types of biosensors in integrated photonics and have taken a small step outside this field. Apart from the literature study, we have also proposed a novel sensing concept for photonic crystals by measuring in the angular spectrum, thereby circumventing the need for an, often expensive, tunable light source. It is clear that each of the presented structures has its own advantages and disadvantages and we therefore do not limit ourselves to one structure. In the following chapters, we will make use of Mach-Zehnder interferometers, ring resonators, Vernier ring resonators and photonic crystals.

References

[1] X. Fan, I. M. White, S. I. Shopova, H. Zhu, J. D. Suter, and Y. Sun. *Sensitive optical biosensors for unlabeled targets: A review.* Analytica Chimica, 620:8–26, 2008.

[2] B. Liedberg, C. Nylander, and I. Lundstrom. *Surface plasmon resonance for gas detection and biosensing.* Sensors and Actuators, 4:299–304, 1983.

[3] P. Debackere. *Nanophotonic Biosensor based on Surface Plasmon Interference.* PhD thesis, Ghent University, 2010.

[4] G. Gupta and J. Kondoh. *Tuning and sensitivity enhancement of surface plasmon resonance sensor.* Sensors and Actuators B: Chemical, 122(2):381–388, March 2007.

[5] A. A. Yanik, M. Huang, A. Artar, T.-Y. Chang, and H. Altug. *Integrated nanoplasmonic-nanofluidic biosensors with targeted delivery of analytes.* Applied Physics Letters, 96(021101):1–3, 2010.

[6] J. Dostálek, J. Ctyroký, J. Homola, E. Brynda, M. Skalský, P. Nekvindová, J. Spirková, J. Skvor, and J. Schröfel. *Surface plasmon resonance biosensor based on integrated optical waveguide.* Sensors and Actuators B, 76:8–12, 2001.

[7] Biacore, *http://www.biacore.com.*

[8] Xantec Bioanalytics, *http://www.xantec.com/.*

[9] IBIS, *http://www.ibis-spr.nl/.*

[10] Corning, *http://www.corning.com/lifesciences*.

[11] A. Biosciences, *http://www.aceabio.com/*.

[12] BioNavis, *http://www.bionavis.com/*.

[13] V. Bronner, M. Edri, I. Zafir-Lavie, E. Rabkin, R. Luo, S. Nimri, and D. Shezifi. *The ProteOn HTE Sensor Chip: Novel Surface for Stable Capture of Histidine-Tagged Proteins for Protein-Small Molecule Interaction Analysis*. Technical report, Bio-Rad Laboratories, 2012.

[14] A. G. Brolo. *Plasmonics for future biosensors*. Nature Photonics, 6(November):709–713, 2012.

[15] L. He, M. D. Musick, S. R. Nicewarner, F. G. Salinas, S. J. Benkovic, M. J. Natan, and C. D. Keating. *Colloidal Au-Enhanced Surface Plasmon Resonance for Ultrasensitive Detection of DNA Hybridization*. Journal of American Chemical Society, 122:9071–9077, 2000.

[16] A. Suzuki, J. Kondoh, Y. Matsui, S. Shiokawa, and K. Suzuki. *Development of novel optical waveguide surface plasmon resonance (SPR) sensor with dual light emitting diodes*. Sensors and Actuators B: Chemical, 106:383–387, April 2005.

[17] J. Dostálek and J. Homola. *Surface plasmon resonance sensor based on an array of diffraction gratings for highly parallelized observation of biomolecular interactions*. Sensors and Actuators B: Chemical, 129:303–310, January 2008.

[18] A. K. Sharma, R. Jha, and B. Gupta. *Fiber-Optic Sensors Based on Surface Plasmon Resonance: A Comprehensive Review*. IEEE Sensors Journal, 7(8):1118–1129, 2007.

[19] COMSOL, *http://www.comsol.com/*.

[20] S. Werquin. *Traag licht voor gevoelige nanofotonische silicium biosensoren*. Master's thesis, Ghent University, 2010.

[21] R. G. Heideman and P. V. Lambeck. *Remote opto-chemical sensing with extreme sensitivity: design, fabrication and performance of a pigtailed integrated optical phase-modulated Mach-Zehnder interferometer system*. Sensors and Actuators B, 61:100–127, 1999.

[22] F. Prieto, B. Sepúlveda, A. Calle, A. Llobera, C. Domínguez, and L. Lechuga. *Integrated Mach-Zehnder interferometer based on ARROW structures for biosensor applications*. Sensors and Actuators B: Chemical, 92:151–158, July 2003.

[23] E. F. Schipper, A. M. Brugman, C. Domínguez, L. M. Lechuga, R. P. H. Kooyman, and J. Greve. *The realization of an integrated Mach-Zehnder waveguide immunosensor in silicon technology.* Sensors and Actuators B, 40:147–153, 1997.

[24] W. Bogaerts, P. De Heyn, T. Van Vaerenbergh, K. De Vos, S. Kumar Selvaraja, T. Claes, P. Dumon, P. Bienstman, D. Van Thourhout, and R. Baets. *Silicon microring resonators.* Laser and Photonics Reviews, pages 1–27, September 2011.

[25] T. Claes. *Advanced Silicon Photonic Ring Resonator Label-Free Biosensors.* PhD thesis, Ghent University, 2012.

[26] A. Ramachandran, S. Wang, J. Clarke, S. J. Ja, D. Goad, L. Wald, E. M. Flood, E. Knobbe, J. V. Hryniewicz, S. T. Chu, D. Gill, W. Chen, O. King, and B. E. Little. *A universal biosensing platform based on optical micro-ring resonators.* Biosensors & Bioelectronics, 23(7):939–44, February 2008.

[27] C.-Y. Chao, W. Fung, and L. Guo. *Polymer microring resonators for biochemical sensing applications.* IEEE Journal of Selected Topics in Quantum Electronics, 12(1):134–142, January 2006.

[28] K. De Vos, I. Bartolozzi, E. Schacht, P. Bienstman, and R. Baets. *Silicon-on-Insulator microring resonator for sensitive and label-free biosensing.* Optics Express, 15(12):7610–7615, 2007.

[29] K. De Vos, J. Girones, T. Claes, Y. De Koninck, S. Popelka, E. Schacht, R. Baets, and P. Bienstman. *Multiplexed Anitbody Detection With an Array of Silicon-on-Insulator Microring Resonators.* IEEE Photonics Journal, 1(4):225–235, 2009.

[30] Genalyte, *http://www.genalyte.com/.*

[31] K. De Vos. *Label-free Silicon Photonics Biosensor Platform with Microring Resonators.* PhD thesis, Ghent University, Ghent, 2010.

[32] X. Li, Y. Su, Z. Zhang, M. Qiu, and S. Qin. *Label-free Biosensor Based on Silicon-On-Insulator Concentric Micro-Ring Resonators.* In 2008 IEEE PhotonicsGlobal@Singapore, pages 1–3, Singapore, December 2008. IEEE.

[33] M. Terrel, M. J. F. Digonnet, and S. Fan. *Ring-coupled Mach-Zehnder interferometer optimized for sensing.* Applied ptics, 48(26):4874–9, September 2009.

[34] L. Jin, M. Li, and J.-J. He. *Highly-sensitive silicon-on-insulator sensor based on two cascaded micro-ring resonators with vernier effect.* Optics Communications, 284(1):156–159, January 2011.

[35] M. La Notte and V. M. Passaro. *Ultra High Sensitivity Chemical Photonic Sensing by Mach-Zehnder Interferometer Enhanced Vernier-Effect.* Sensors and Actuators B: Chemical, 176:994–1007, October 2013.

[36] E. Yablonovitch. *Inhibited Spontaneous Emission in Solid-State Physics and Electronics.* Physical Review Letters, 58(20):2059–2062, 1987.

[37] S. John. *Strong Localization of Photons in Certain Disordered Dielectric Superlattices.* Physical Review Letters, 58(23):2486–2489, 1987.

[38] M. Huang, A. A. Yanik, T.-Y. Chang, and H. Altug. *Sub-wavelength nanofluidics in photonic crystal sensors.* Optics Express, 17(26):24224–24233, December 2009.

[39] B. T. Tung, D. V. Dao, T. Ikeda, Y. Kanamori, and K. Hane. *Investigation of strain sensing effect in modified single-defect photonic crystal nanocavity.* Optics Express, 19(9):8821–8829, 2011.

[40] Y. Liu and H. W. M. Salemink. *Photonic crystal-based all-optical on-chip sensor.* Optics Express, 20(18):19912, August 2012.

[41] O. Painter, A. Husain, A. Scherer, P. Lee, I. Kim, J. O'Brien, and P. Dapkus. *Lithographic tuning of a two-dimensional photonic crystal laser array.* IEEE Photonics Technology Letters, 12(9):1126–1128, September 2000.

[42] H.-G. Park, S.-H. Kim, M.-K. Seo, Y.-G. Ju, S.-B. Kim, and Y.-H. Lee. *Characteristics of Electrically Driven Two-Dimensional Photonic Crystal Lasers.* Ieee Journal of Quantum Electronics, 41(9):1131–1141, 2005.

[43] Y. Chassagneux, R. Colombelli, W. Maineults, S. Barbieri, S. P. Khanna, E. H. Linfield, and A. G. Davies. *Predictable surface emission patterns in terahertz photonic-crystal quantum cascade lasers.* Optics Express, 17(12):9491–502, June 2009.

[44] F. Villa and J. Gaspar-Armenta. *Photonic crystal to photonic crystal surface modes: narrow-bandpass filters.* Optics Express, 12(11):2338–55, May 2004.

[45] E. Drouard, H. Hattori, C. Grillet, A. Kazmierczak, X. Letartre, P. Rojo-Romeo, and P. Viktorovitch. *Directional channel-drop filter based on a slow Bloch mode photonic crystal waveguide section.* Optics Express, 13(8):3037–48, April 2005.

[46] M. Davanço, A. Xing, J. W. Raring, E. L. Hu, and D. J. Blumenthal. *Compact Broadband Photonic Crystal Filters With Reduced Back-Reflections for Monolithic InP-Based Photonic Integrated Circuits.* IEEE Photonics Technology Letters, 18(10):1155–1157, 2006.

[47] O. Willekens. *Optische biosensor gebaseerd op het superprismaeffect in fotonische kristallen.* Master's thesis, Ghent University, 2010.

[48] J. D. Joannopoulos, S. G. Johnson, J. N. Winn, and R. D. Meade. *Photonic Crystals: Molding the Flow of Light.* Princeton University Press, 2nd edition, 2007.

[49] Y. Zhao, X. Zhao, and Z. Gu. *Photonic Crystals in Bioassays.* Advanced Functional Materials, 20(18):2970–2988, September 2010.

[50] S. Xiao and N. A. Mortensen. *Highly dispersive photonic band-gap-edge optofluidic biosensors.* Journal of the European Optical Society, 2006.

[51] A. F. Oskooi, D. Roundy, M. Ibanescu, P. Bermel, J. D. Joannopoulos, and S. G. Johnson. *MEEP: A flexible free-software package for electromagnetic simulations by the FDTD method.* Computer Physics Communications, 181:687–702, 2010.

[52] S. G. Johnson and J. D. Joannopoulos. *Block-iterative frequency-domain methods for Maxwell's equations in a planewave basis.* Optics Express, 8(3):173–190, 2001.

[53] S. G. Johnson, P. R. Villeneuve, S. Fan, and J. D. Joannopoulos. *Linear waveguides in photonic-crystal slabs.* Physical Review B, 62(12):8212–8222, 2000.

[54] U. Bog, C. L. C. Smith, M. W. Lee, S. Tomijenovie-Hanic, C. Grillet, C. Monat, L. O'Faolain, C. Karnutsch, T. F. Krauss, R. C. McPhedran, and B. J. Eggleton. *High-Q microfluidic cavities in silicon-based two-dimensional photonic crystal structures.* Optics Letters, 33(19):2206–2208, 2008.

[55] R. Terawaki, Y. Takahashi, M. Chihara, Y. Inui, and S. Noda. *Ultrahigh-Q photonic crystal nanocavities in wide optical telecommunication bands.* Optics Express, 20(20):22743–22752, 2012.

[56] S. Combrié, E. Weidner, A. DeRossi, S. Bansropun, S. Cassette, A. Talneau, and H. Benisty. *Detailed analysis by Fabry-Perot method of slab photonic crystal line-defect waveguides and cavities in aluminium-free material system.* Optics Express, 14(16):7353–7361, 2006.

[57] E. Chow, A. Grot, L. W. Mirkarimi, M. Sigalas, and G. Girolami. *Ultracompact biochemical sensor built with two-dimensional photonic crystal microcavity.* Optics Letters, 29(10):1093–1095, 2004.

[58] N. Skivesen, A. Têtu, M. Kristensen, J. Kjems, L. H. Frandsen, and P. I. Borel. *Photonic-crystal waveguide biosensor.* Optics Express, 15(6):3169–3176, 2007.

[59] S. Fan and J. D. Joannopoulos. *Analysis of guided resonances in photonic crystal slabs.* Physical Review B, 65:1–8, 2002.

[60] M. El Beheiry, V. Liu, S. Fan, and O. Levi. *Sensitivity enhancement in photonic crystal slab biosensors.* Optics Express, 18(22):22702–22714, 2010.

[61] B. Cunningham, P. Li, B. Lin, and J. Pepper. *Colorimetric resonant reflection as a direct biochemical assay technique.* Sensors and Actuators B, 81:316–328, 2002.

[62] B. Cunningham. *Novel biosensors from photonic crystals.* SPIE Newsroom, 2008.

[63] E. Hallynck and P. Bienstman. *Photonic crystal biosensor based on angular spectrum analysis.* Optics Express, 18(17):18164–18170, 2010.

[64] A. Hessel and A. A. Oliner. *A New Theory of Wood's Anomalies on Optical Gratings.* Applied Optics, 4(10):1275–1299, 1965.

[65] N. Le Thomas, R. Houdré, M. V. Kotlyar, D. O'Brien, and T. F. Krauss. *Exploring light propagating in photonic crystals with Fourier optics.* Journal of the Optical Society of America B, 24(12):2964–2971, 2007.

[66] K. Van Acoleyen. *Nanophotonic Beamsteering Elements Using Silicon Technology for Wireless Optical Applications.* PhD thesis, Ghent University, 2012.

[67] H. Kosaka, T. Kawashima, A. Tomita, M. Notomi, T. Toshiaki, S. Takashi, and K. Shojiro. *Superprism phenomena in photonic crystals.* Physical Review B, 58(16):R10 096 —- R10 099, 1998.

[68] T. Prasad, D. M. Mittleman, and V. L. Colvin. *A photonic crystal sensor based on the superprism effect.* Optical Materials, 29:56–59, 2006.

[69] H.-J. Sheng, W.-F. Liu, K.-R. Lin, S.-S. Bor, and M.-Y. Fu. *High-sensitivity temperature-independent differential pressure sensor using fiber Bragg gratings.* Optics Express, 16(20):16013–16018, 2008.

[70] N. Liu, Y. Li, Y. Wang, H. Wang, W. Liang, and P. Lu. *Bending insensitive sensors for strain and temperature measurements with Bragg gratings in Bragg fibers.* Optics Express, 19(15):13880–91, July 2011.

[71] D. Paladino, G. Quero, C. Caucheteur, P. Mégret, and A. Cusano. *Hybrid fiber grating cavity for multi-parametric sensing.* Optics Express, 18(10):10473–86, May 2010.

[72] W. Liang, Y. Huang, Y. Xu, R. K. Lee, and A. Yariv. *Highly sensitive fiber Bragg grating refractive index sensors.* Applied Physics Letters, 86(15):151122, 2005.

[73] A. N. Chryssis, S. M. Lee, S. B. Lee, S. S. Saini, and M. Dagenais. *High Sensitivity Evanescent Field Fiber Bragg Grating Sensor.* IEEE Photonics Technology Letters, 17(6):1253–1255, 2005.

[74] C. Caucheteur, D. Paladino, P. Pilla, A. Cutolo, S. Campopiano, M. Giordano, A. Cusano, and P. Mégret. *External Refractive Index Sensitivity of Weakly Tilted Fiber Bragg Gratings With Different Coating Thicknesses.* IEEE Sensors Journal, 8(7):1330–1336, 2008.

[75] D. J. J. Hu, J. L. Lim, M. K. Park, L. T.-H. Kao, Y. Wang, H. Wei, and W. Tong. *Photonic Crystal Fiber-Based Interferometric Biosensor for Streptavidin and Biotin Detection.* IEEE Journal of Selected Topics in Quantum Electronics, 18(4):1293–1297, July 2012.

[76] T. Wei, Y. Han, Y. Li, H.-L. Tsai, and H. Xiao. *Temperature-insensitive miniaturized fiber inline Fabry-Perot interferometer for highly sensitive refractive index measurement.* Optics Express, 16(8):5764–9, April 2008.

[77] FortéBIO, *http://www.fortebio.com/*.

[78] C. Lerma Arce, K. De Vos, T. Claes, K. Komorowska, D. Van Thourhout, and P. Bienstman. *Silicon-on-Insulator Microring Resonator Sensor Integrated on an Optical Fiber Facet.* IEEE Photonics Technology Letters, 23(13):890–892, 2011.

[79] A. Ymeti, J. S. Kanger, J. Greve, G. A. J. Besselink, P. V. Lambeck, R. Wijn, and R. G. Heideman. *Integration of microfluidics with a four-channel integrated optical Young interferometer immunosensor.* Biosensors and Bioelectronics, 20:1417–1421, 2005.

[80] Z. Wang and D. J. Bornhop. *Dual-capillary backscatter interferometry for high-sensitivity nanoliter-volume refractive index detection with density gradient compensation.* Analytical Chemistry, 77(24):7872–7, December 2005.

[81] F. Patolsky and C. M. Lieber. *Nanowire nanosensors.* Materials Today, April:20–28, April 2005.

[82] S. Roy and Z. Gao. *Nanostructure-based electrical biosensors.* Nano Today, 4:318–334, August 2009.

[83] F. Patolsky, G. Zheng, O. Hayden, M. Lakadamyali, X. Zhuang, and C. M. Lieber. *Electrical detection of single viruses.* Proceedings of the National Academy of Sciences of the United States of America, 101(39):14017–22, September 2004.

[84] P. Bergveld. *Development of an Ion-Sensitive Solid-State Device for Neurophysiological Measurements.* IEEE Transactions on Biomedical Engineering, BME-17(1):70–71, 1970.

[85] L. Carrascosa, M. Moreno, M. Álvarez, and L. Lechuga. *Nanomechanical biosensors: a new sensing tool.* rends in Analytical Chemistry, 25(3):196–206, March 2006.

[86] Concentris, *http://www.concentris.ch/*.

[87] Protiveris, *http://www.protiveris.com/*.

[88] K. Länge, B. E. Rapp, and M. Rapp. *Surface acoustic wave biosensors: a review.* Analytical and Bioanalytical Chemistry, 391(5):1509–19, July 2008.

“We can’t kill our way out of this mess.”

Mitt Romney providing the least American quote of the final debate, Entrepreneur, 1947-present

3 Fabrication

Some of the requirements for a commercially viable biosensor is that it is low cost and capable of being produced in high volumes, as most biosensors are supposed to be disposable after a single use. A good candidate that is capable of delivering these requirements is Silicon-on-Insulator (SOI) in combination with Deep Ultraviolet (Deep UV) lithography. In order to obtain the membranes mentioned in Chapter 1 to facilitate a flow through the photonic structure, we need to perform several post-processing steps on the chips received from the wafer fab. After a short introduction to Silicon-on-Insulator, we will discuss these post-processing steps in more detail.

3.1 Silicon-on-insulator

Photonics is going through the same evolution as electronics has experienced years ago, namely one of integration: bulk components are miniaturised in order to reduce costs and increase production volume. While the largest part of the electronics industry nowadays consists of integrated circuits (ICs) fabricated in silicon using complementary metal-oxide-semiconductor (CMOS) technology, there is no material platform that rises head and shoulders above the others for photonic integrated circuits (PICs). So, instead of one material platform that over time has phased out all others, we see a variety of material systems coexisting, with the most popular ones being GaAs, silica, InP and silicon-based

technologies. One material platform, however, that has several advantages over the others for the application(s) described in this work is silicon-on-insulator (SOI).

Since silicon is the key material used in the electronics industry, the main advantage of it is that for the processing of SOI wafers, we can borrow a lot of the expertise that has already been gathered over the past decades. As in electronics, it is possible to produce large wafers (300 mm diameter wafers are now the standard with perspectives of going to 450 mm diameter) comprising hundreds of individual chips. Together with the fact that silicon is a cheap material that can be found in abundance, worldwide we can produce chips in large quantities at a low price per chip.

While these are all advantages for processing PICs, we have to assure ourselves of the fact that SOI is a suitable platform from a design point-of-view. It turns out that silicon has a relatively high refractive index (3.476 at 1550 nm wavelength) and low loss in both the O and C band (respectively from 1260-1360 nm and 1530-1565 nm) which are used for telecommunication. It can be shown that for a high index contrast (silicon dioxide has a refractive index of 1.444 at 1550 nm), the waveguiding structures can be made very small [1]. As a consequence, another advantage of the SOI platform is that we are able to miniaturise photonic structures to an extent much greater than is possible in e.g. indium phosphide. One drawback of silicon is that it has an indirect band gap and this makes it very difficult to design active components (e.g. lasers or detectors). It is however possible to integrate silicon with other material systems which do allow for active components [2].

The wafers supplied to us are produced by *SOITEC* using the SmartCut^{TM} process (see Figure 3.1) and consist of a 220 nm top silicon layer on a 2-µm-thick buried silicon dioxide or, commonly referred to as, buried oxide (BOX) layer, on top of a 725-µm-thick silicon substrate.

These wafers are processed in the clean rooms of *imec* using Deep UV lithography at a wavelength of 193 nm [3]. A full silicon etch step (220 nm depth) and shallow silicon etch step (70 nm depth) are executed on the top silicon (or device) layer as illustrated in Figure 3.2. In most cases, these two steps suffice to design a photonic structure in silicon. More advanced photonic structures may require an extra etch step [4], at a higher wafer cost, but these structures are outside of the scope of this work.

After these two etching steps, normally no additional processing has to take place and the wafer is ready. In our case, however, we require an additional process step: thinning of the silicon substrate. This is done by mounting the wafer on a chuck after which the substrate is pressed down against a rotating pad while a chemical slurry is flown over the pad. The silicon is removed by a combination of abrasive polishing and chemical etching. Note that while sub-

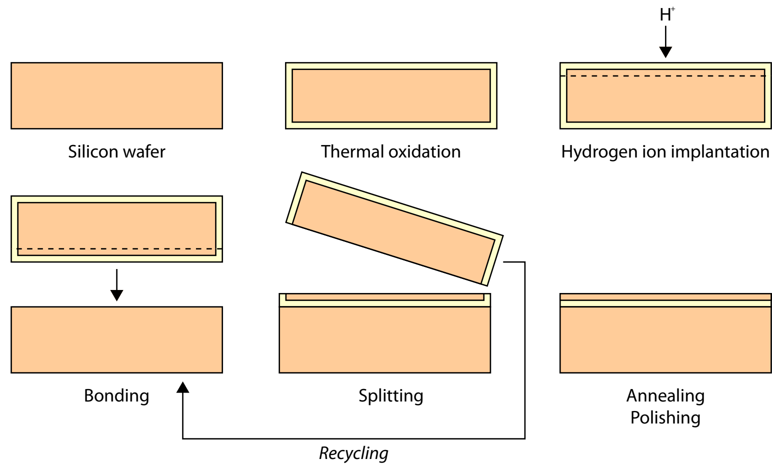

Figure 3.1: SOITEC SmartCut^{TM} process: thermal silicon dioxide is grown on a silicon wafer, hydrogen ions are implanted, a second silicon wafer is bonded, the substrate of the initial wafer is removed after which the remaining silicon-on-insulator wafer is polished and annealed.

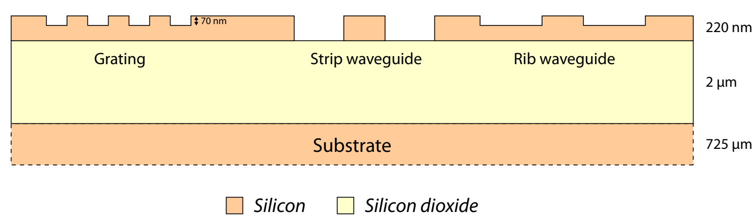

Figure 3.2: Using Deep UV lithography, a full and shallow etch step are executed on the top silicon (or device) layer with respective etch depths of 220 nm and 70 nm. Most basic photonic structures can be implemented using these two etch steps.

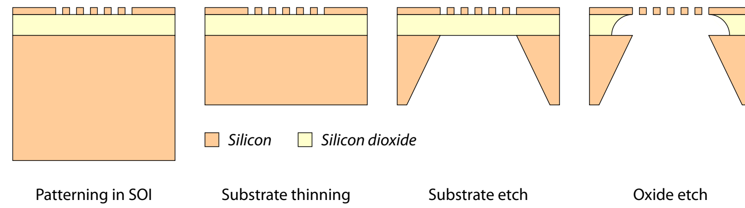

Figure 3.3: Four major processing steps in order to produce thin membranes with holes: a) The photonic structures are defined using Deep UV lithography; b) The wafer is thinned down to facilitate the subsequent substrate etch; c) The substrate is locally etched; d) Finally, the buried oxide layer is removed locally to achieve the thin membranes.

strate thinning is also possible on a die basis, we chose to thin down the entire wafer using a reliable process at *imec*, which can save huge amounts of time compared to die based thinning.

It should be noted that in the following sections, the work done in this PhD has been carried out on single dies, cut from an entire wafer, since the total number of wafers at our disposal was limited. However, none of the following steps are inherently die-based and are all applicable on a wafer scale.

3.2 Anisotropic silicon substrate etch

Now that the wafer is thinned down, we have to etch the silicon substrate underneath the photonic structures of interest (third step in Figure 3.3). The etching of silicon [5–10] has been studied extensively for over decades (not in the least because of its use in the semiconductor industry) and can be done either by dry etching (i.e. ion etching) or wet etching. Dry etching of silicon is mainly done using a combination of a fluorine based gas (like SF_6 or CF_4) and other (like O_2 or N_2O) gases. Without going into further detail, the principle of this etching method is based on generating a plasma of the precursor gasses that comes into contact with silicon. Fluorine ions are responsible for the main mechanism of etching silicon while the oxygen prevents recombination of fluorine ions with fluorosulphur radicals, thus increasing the net amount of fluorine ions and as a consequence, the etch rate [6].

In general, a dry etching process is preferred since it is possible to achieve a very high degree of anisotropy (see Figure 3.4). Since such a process for silicon was not available in our facilities, we had to opt for wet etching. Wet etching of silicon can be done either isotropically (using a mixture of HF, HNO_3, CH_3COOH and water) or anisotropically (see Figure 3.4) where the most com-

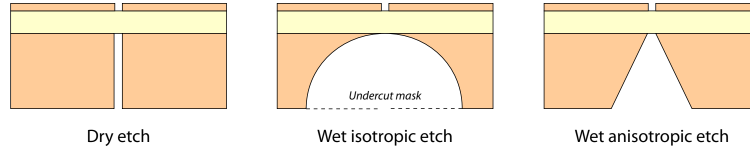

Figure 3.4: Silicon can be dry etched (left) or wet etched isotropically (middle) or anisotropically (right). Since we do not want the etching pits to overlap, it is clear that a higher hole density can be achieved using a dry etch process.

monly used etchants are KOH and tetramethylammonium hydroxide (TMAH).

Two disadvantages of this isotropic etch, compared to the anisotropic etchants, is that a significant part of the substrate will be unnecessarily removed, thus compromising the mechanical integrity of the die. More importantly, due to the fact that the mixture contains HF, once the substrate has been removed, the etch will not stop at the buried oxide layer. This implies that not only the silicon dioxide layer will be removed but the 220 nm thin top silicon layer will also be etched in an instant. Very precise timing is therefore required.

On the other hand, KOH and TMAH, which are both anistropic etchants, exhibit a high selectivity of etching silicon compared to silicon dioxide [9] and as a consequence, the buried oxide layer acts as an etch stop layer. Moreover, since the etching profile is determined by the crystal planes of silicon (some planes exhibit a higher etch rate than others), we conserve much more material in the substrate, compared to an isotropic etch. We have opted for KOH since it is faster and more reliable than TMAH. Some tests with TMAH have been done but the performance of the etchant (in terms of undercut and speed) was well below that of KOH so we decided not to investigate that route further. KOH etches silicon according to the chemical reaction in (3.1) [7]. It is interesting to note that the K^+-ions take no part in the actual reaction.

$$Si + 2H_2O + 2OH^- \rightarrow 2H_2 + SiO_2(OH)_2^{2-} \tag{3.1}$$

The top plane of the wafers supplied to us by ePIXfab [11] is a (100) plane with the wafer flat (horizontal axis in Figure 3.5) along the [110] direction. According to Shikida [10], the ratio of etch rates of the (100) plane compared to the other crystal planes is lowest for the (111) plane (as low as 0.014). Therefore, the walls of the etch pit in our silicon substrate will be oriented along these (111) planes. Due to symmetry in the silicon crystal, the etch pit will have the shape of a trapezoid. From Figure 3.6a it can be calculated that the angle θ between the (111) plane and the [110] flat is $\arctan\sqrt{2}$ or 54.74°.

Since we wish to only etch certain parts of the silicon substrate, we need to

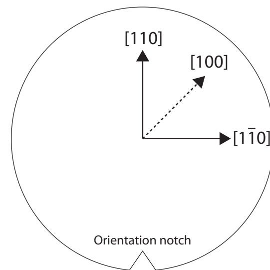

Figure 3.5: The orientation of a silicon wafer can in most cases be determined by means of an alignment notch, cut in the wafer. The wafers supplied to us have the [110] silicon crystal direction along the horizontal axis when the alignment notch is pointing south.

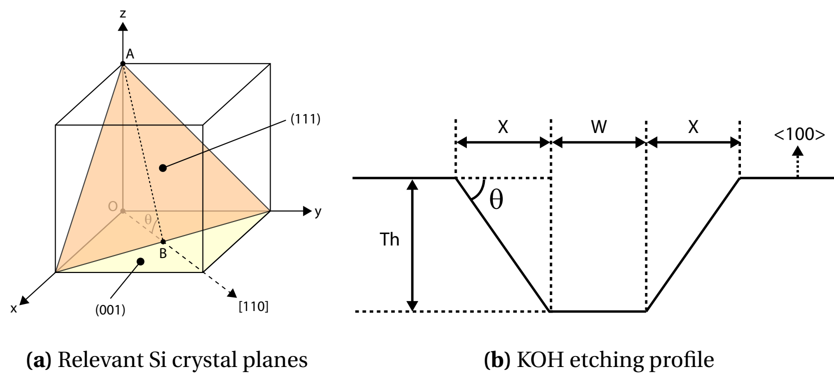

(a) Relevant Si crystal planes

(b) KOH etching profile

Figure 3.6: Because the angle θ between the (111) plane and the [110] flat equals arctan $\sqrt{2}$, the desired window width W needs to be augmented by $2X$ or $\sqrt{2}Th$.

apply a mask layer before etching. Due to the anisotropic nature of KOH etching the openings in the mask layer need to be much broader than the eventual size of the opening near the buried oxide layer. From Figure 3.6b, it can be calculated that the mask dimensions are the eventual opening size W increased by $\sqrt{2}Th$ where Th is the substrate thickness. When placing several photonic structures in the top silicon layer, one has to take into account the fact that the larger openings in the masking material cannot overlap (which would create one big opening) so sufficient spacing between the structures needs to be considered in the design phase.

The actual etching rate of silicon can be determined using the Arrhenius equation:

$$R = R_0 \exp\left(\frac{-E_a}{kT}\right) \tag{3.2}$$

Here R_0 is a pre-exponential factor, E_a the activation energy, k the Boltzmann constant and T the temperature of the etch bath. According to Seidel [9], for 20% KOH, the (100) plane etch has an E_a of 0.57 eV and R_0 equals $1.23 \cdot 10^{10}$ µm/h. At a temperature of 80°C, this corresponds to an etch rate of 1.43 µm/min. To illustrate: etching through a 250 µm thick substrate will take approximately 3 hours. When further increasing the temperature, to increase the etch rate, one has to take into account the fact that the selectivity of the masking material compared to silicon will decrease significantly.

3.2.1 Masking materials

Now that we have sufficient knowledge to design the dimensions of the mask needed for the substrate etch, we need to choose an appropriate masking material. Since etching silicon with KOH is a well-documented etching process, several materials have been tested in the literature: oxide [9], nitride [12, 13], gold [14], ProTEK® [15–17], benzocyclobutene (BCB) [18, 19], ... In the course of this work, we have investigated several of these materials.

- **Gold**
  The option of using gold as a masking material (with a thin chromium layer in between the silicon substrate and the gold to improve adhesion) was only briefly considered since the entire mask layer peeled off almost instantaneously when the die was immersed in KOH. We therefore chose to focus more on the more commonly used dielectric materials like silicon dioxide and silicon nitride, strengthened by the fact that the gold process is not very widely used in literature.

- **Silicon dioxide**
  According to Seidel [9], the selectivity of 20% KOH at 80°C with respect to

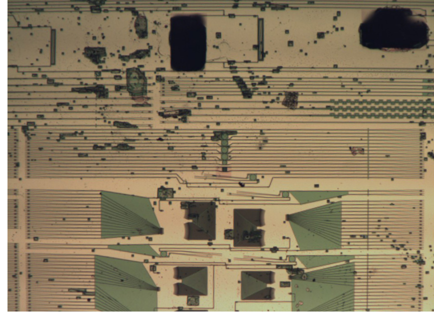

Figure 3.7: Although silicon nitride is used as a protection layer for the silicon structures in the device layer of the die, the large amount of pinholes can render the device useless.

etching (100) silicon over thermal silicon dioxide is 320:1. While this ratio is relatively high, we are likely to observe a lower selectivity for Plasma-Enhanced Chemical Vapour Deposited (PECVD) silicon dioxide due to the nature of the deposition process that creates less dense layers. Therefore, we would need a relatively thick layer of this material to withstand the etching of 250 μm of silicon.

- **Silicon nitride**
  A much better dielectric hard mask layer is silicon nitride. Seidel [9] has reported that in their experiments, they saw no significant etching of a silicon nitride mask (as opposed to silicon dioxide, where they were able to establish an etch rate). It is therefore clear that silicon nitride is preferred over silicon dioxide. However, in our facilities, silicon nitride is deposited using PECVD which can lead to pinholes being introduced in the silicon nitride [20, 21]. KOH can penetrate through these pinholes, etching parts of the silicon that were not intended to be etched. At the substrate side of the die, these small pinholes do not cause major problems but since we also use silicon nitride to protect the device side of the die where the silicon structures are defined, we require a very low pinhole density because one pinhole located over one waveguide can render an entire structure useless. This is illustrated in Figure 3.7. Low-Pressure Chemical Vapour Deposited (LPCVD) silicon nitride would not suffer from this problem of pinholes and would therefore be a preferred choice, but it was not available in our clean rooms.

- **ProTEK®**
  ProTEK® is a commercially available polymer designed specifically to resist alkaline based etchants. It comes in a photodefinable and non-

photodefinable variant (PSB and B3 respectively). Although our tests showed that the material withstands KOH very well and for a very long time, we had several issues trying to develop the photodefinable ProTEK®. Since the material has a very limited shelf life and is quite expensive, we decided to give preference to the readily available silicon dioxide and silicon nitride in our facilities. We also did tests with the non-photodefinable ProTEK® B3 for protection of the device layer (see Section 3.2.3) and found it to be a very useful material although the adhesion quality degraded rapidly after the expiration date of the primer, resulting in peeling of the protective layer. Removal of the material after etching also proved to be difficult at times since the suggested remover of the supplier does not dissolve the material but merely detaches the ProTEK® layer. The problem we faced frequently was that the material redeposited in the holes etched by the KOH after which we were unable to remove it. This is illustrated in Figure 3.8.

- **BCB**
  Cured BCB is also known to resist KOH quite well [19] and was also considered as a masking layer. We observed severe undercut up to the point where individual mask openings would start merging at a very early stage. As a protective layer we were unable to obtain good adhesion between the silicon nitride and the BCB and peeling of the BCB film occurred, leaving the silicon nitride exposed. When the BCB was used as a bonding layer between the device layer and a pyrex wafer, the top silicon was protected during KOH etching but it is however difficult to debond the die afterwards. While cured BCB can normally be etched using a mixture of 3 parts H_2SO_4 and 1 part H_2O_2 (commonly referred to as a Piranha solution due to its bubbly nature when the two components are mixed and the fact that it dissolves nearly all organic materials), in this case the solution can only attack the BCB from the sides of the die making the etching process very inefficient. The use of porous pyrex wafers might be a route worth investigating further.

Eventually, we opted for 400 nm PECVD silicon nitride with a 400 nm PECVD silicon dioxide layer in between the silicon substrate and the silicon nitride. The silicon dioxide acts mainly as a buffer layer between the silicon substrate and the oxide and nitride due to their relatively large lattice mismatch [12, 22]. Note that another possible candidate for a masking material is silicon oxynitride (SiON) which can be grown in thick, stress-free layers and is also known to be resistant to KOH [23]. Further optimisation of the fabrication process should indicate whether it is more beneficial to replace the silicon nitride and silicon dioxide layer stack by a single layer of silicon oxynitride.

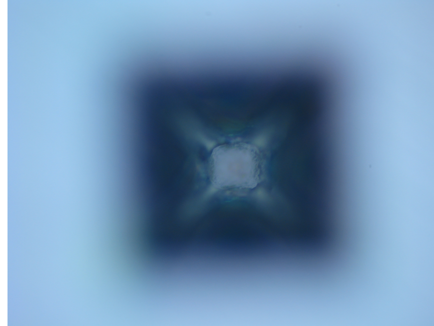

Figure 3.8: When removing the ProTEK® it is possible that it redeposits in the holes etched by the KOH, after which it is very difficult to remove it. In this picture, the photonic structure at the device side is no longer visible and etchants are unable to reach the silicon dioxide layer.

To create openings in the mask layer, we have to perform contact lithography. We apply a thick layer of standard photoresist (e.g. AZ MicroChemicals 5214E) on the substrate side of the die and pattern it using the backside alignment module of our contact lithography tool. This module enables us to define openings in the photoresist on the substrate side of the die, using alignment markers found on the device side of the die. The principle for this is quite straightforward and illustrated in Figure 3.9: two microscope objectives (with a minimal spacing of about 1.5 cm) placed below a transparent sample holder are moved so that they see the alignment markers of the contact mask. A computer captures the images of both objectives and overlays it on the image of the objectives during subsequent steps. The die with photoresist on the substrate side is placed on the maskholder between the contact mask and the microscope objectives in such a way that the device side, containing the alignment markers, face the objectives. The position of the maskholder can now be changed in plane using two translation stages and one rotation stage. Once the alignment markers of the die match those of the overlain image, the photoresist can be illuminated. After development of the photoresist, the die is transferred to a reactive ion etcher (RIE) where a mixture of SF_6 and O_2 is used to etch through the silicon nitride and silicon dioxide layers with the photoresist acting as a soft mask. After removal of the photoresist, the sample is ready for KOH etching. As mentioned above, we used 20% KOH at a temperature of 80°C with which it takes about 3 hours to etch through our dies.

It should be noted that due to poor mask adhesion in some places, we can observe undercut in the etching holes (see Figure 3.10). It is clear that the amount of undercut adds to the final membrane size: an undesired effect. On average, the undercut is limited to about 8 μm on each side of the etching pit

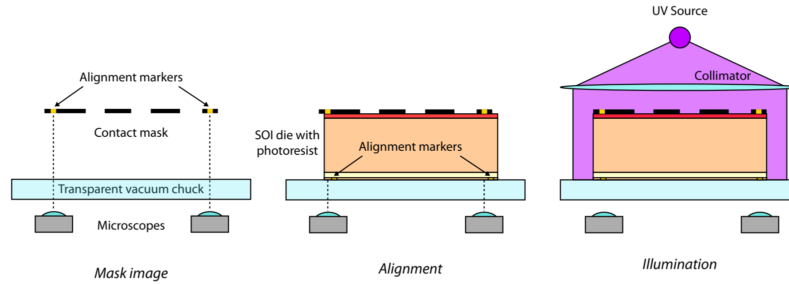

Figure 3.9: Principle of backside alignment: the computer grabs an image of the alignment markers of the mask and overlays it on the image when the die is inserted. By moving the sample in plane and rotating it, the alignment makers of the mask and sample can be matched and the sample can be illuminated.

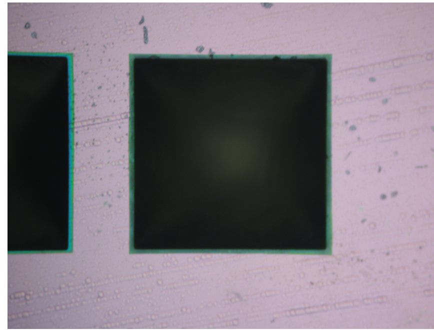

Figure 3.10: The greenish border of the etching pit is undercut silicon nitride in an average case. The amount of undercut adds to the final membrane size.

but in some cases it can go up to several tens of microns, resulting in large, strongly buckled membranes (see later).

3.2.2 Sample preparation

In order to achieve good adhesion of the masking material to the silicon substrate, we have to assure ourselves of the fact that the substrate is free of any contaminants. For this, all samples are rinsed first using acetone and isopropyl alcohol (IPA) and subsequently immersed for 10 minutes in a Piranha solution.

In our experiments we have seen that thorough cleaning of the die proves to be insufficient sometimes for proper mask adhesion. When we use the silicon dioxide and silicon nitride stack (as discussed in Section 3.2.1) as a hard

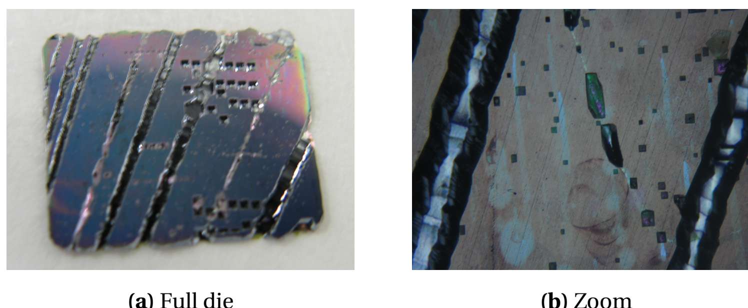

(a) Full die **(b)** Zoom

Figure 3.11: In this die, shown after KOH etching, no initial KOH dip was performed. It is evident that large grooves have formed caused by bad mask adhesion along lines caused by thinning of the die.

mask for KOH, we observe partial or complete loss of adhesion: in the case of complete loss of adhesion, the entire substrate is etched; in the other case of partial loss of adhesion we observe large cracks as can be seen in Figure 3.11. We can conclude that the origin of these cracks is not of a crystallographic nature since their orientation varies across one die. However, when looking at an unprocessed die using a white light interferometer, we see nano-roughness in the form of lines (see Figure 3.12a). These lines are created during the substrate thinning process in the wafer fab. For reasons not yet fully understood, some of these lines cause poor silicon dioxide and silicon nitride adhesion and end up as large cracks in the hard mask during KOH etching.

In order to remove these lines, which should increase silicon dioxide and silicon nitride adhesion to the silicon, there are two possible solutions: a first one is performing an additional CMP step on individual dies using a tool in our clean rooms; a second one is dipping the die shortly in KOH, which will increase the roughness but can also break the line pattern.

Chemical Mechanical Polishing is an art in its own right since it is a process where a lot of parameters need to be fine-tuned: the type and roughness of the polishing pad, the pressure exerted on the pad, the type and dilution of the slurry used, the polishing time, ... A lot of effort was put into trying to decrease the roughness further from the already low value of 4.29 nm of an unprocessed die but with the given tool and slurry, we were unable to do so. However, we were able to remove the line pattern at the cost of increased roughness (see Figure 3.12b). One die needs to be polished for approximately one hour and since the polishing is done on a die-basis, it is a very time-consuming process to prepare a whole batch of dies.

The second option is performing a short KOH dip. This will also increase the roughness but will distort the line pattern. Best results were obtained for

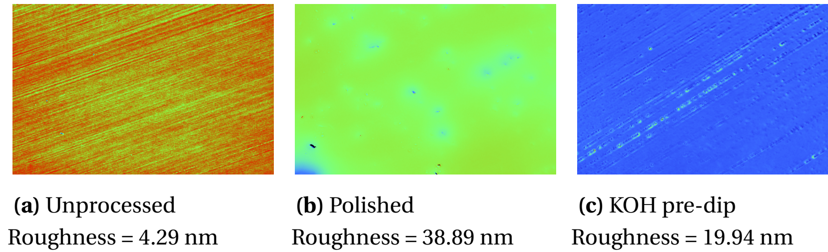

(a) Unprocessed Roughness = 4.29 nm

(b) Polished Roughness = 38.89 nm

(c) KOH pre-dip Roughness = 19.94 nm

Figure 3.12: Although the root mean square roughness of the die increases by either dipping it shortly in KOH or polishing it using our CMP tool, we are able to remove or disrupt the pattern of the unprocessed die.

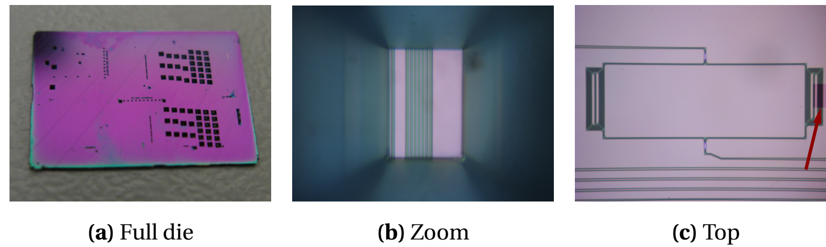

(a) Full die **(b)** Zoom **(c)** Top

Figure 3.13: (a) shows a complete, etched SOI die with the substrate facing up; (b) is a view into one of the holes; (c) shows the complete structure where the discoloured part (see arrow) of the right arm of the Mach-Zehnder interferometer indicates the underetched region.

highly concentrated KOH (in our experiments we went as high as a 65% KOH solution) where a one-minute dip was enough at a temperature of 79°C. The resulting surface can be seen in Figure 3.12c. Not only is this approach much faster compared to CMP but it is also possible to process several samples in parallel.

As mentioned above, the reason why these preparatory steps had a significant beneficial effect on hard mask degradation is not yet understood but the obtained results were very consistent. Figure 3.13 shows a die after KOH substrate etching, where a KOH pre-dip was performed before silicon dioxide and silicon nitride deposition. Some lines are still clearly visible but as shown in Figure 3.12b they are disrupted on a nano-scale. No significant hard mask failure occurs over the entire die.

3.2.3 Protection of the device layer

As mentioned above and illustrated in Figure 3.7, we need to pay attention to proper protection of the photonic structures in the device layer. We can choose

to deposit a layer that can be easily removed afterwards (e.g. organic materials) or a material that can remain on the die (e.g. dielectrics), save for the places where we require only the silicon membrane. The latter approach has the benefit that parts of the device that are not part of the actual transducer are protected from the analyte environment (provided that the evanescent tail of the waveguide mode does not significantly reach through these layers). Note that in practice, silicon dioxide is sometimes deposited on top of the SOI wafer because it is required in the thinning process.

Based on the above arguments, we will also deposit the same layer stack as we use at the substrate side as an etching mask (i.e. 400 nm PECVD silicon nitride with a 400 nm PECVD silicon dioxide layer in between the silicon substrate and the silicon nitride) on the device side of the die. In Section 3.2.1 we mentioned that PECVD silicon nitride can exhibit a high pinhole density, which is unacceptable in our situation as one pinhole above a waveguide can damage the functionality of a whole device. Problems of high pinhole density occur mainly in PECVD silicon nitride films deposited at a temperature lower than 300°C [20]. In our lab, the deposition temperature of the PECVD tool is limited to 320°C, only slightly above this temperature. In our experiments we have seen that silicon nitride deposited at this temperature still showed pinholes (although less than in silicon nitride deposited at a lower temperature). Annealing the silicon nitride after deposition for 1 hour at 450°C also showed no improvement. We therefore need to deposit another material on top of the silicon nitride to solve the problem of pinholes. Note that even in silicon nitride deposited at higher temperatures (much higher than 320°C), some pinholes still appear so an extra layer could also increase yield there, provided the fabrication cost of this extra layer is sufficiently low.

Two good candidates for this extra top layer are the already mentioned BCB and ProTEK® B3. We encountered poor adhesion in most of our BCB experiments except for when the die was bonded to a pyrex wafer. If a proper method would be found to debond the die from the wafer, BCB would be the preferred choice. Therefore, despite the drawbacks of difficult removal and short shelf life, we chose for ProTEK® B3. After silicon oxide and silicon nitride deposition and patterning using contact lithography, we applied a 7.0μm-thick layer of ProTEK® B3, using the process described in the data sheet.

When etching the silicon nitride/dioxide stack using RIE to pattern the substrate etch mask, we have to consider protecting the nitride/dioxide mask on the device side of the die. Due to the isotropic nature of SF_6, part of the nitride/-dioxide mask will be etched, leaving the borders of the device layer vulnerable to KOH (the result of which can be seen in Figure 3.15). In order to prevent this, we can apply a protective layer of photoresist on top of our sample, before dry etching the nitride/dioxide mask. Using another gas, like CHF_3, could increase

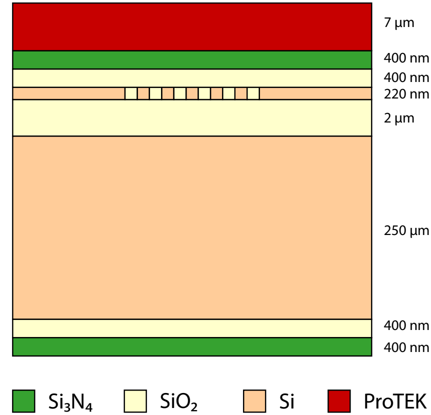

Figure 3.14: Final layer stack of the SOI die. Apart from a stack of silicon nitride on silicon oxide on both sides, we apply an extra protective coating at the top of the sample to protect it from KOH penetrating through silicon nitride pinholes.

directionality of the etching process and make this protective photoresist layer obsolete.

3.3 Isotropic silicon dioxide etch

Once the substrate is etched, we can proceed to the fourth and final step of Figure 3.3, which is the etching of the buried oxide layer. Note that due to the fact that we also used silicon dioxide and silicon nitride on the device side of our samples to protect the silicon structures, we also need to locally remove these layers in this step.

The only effective wet etchant available for silicon dioxide is HF. It etches silicon dioxide according to the following reaction equation:

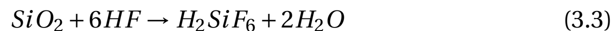

$$SiO_2 + 6HF \rightarrow H_2SiF_6 + 2H_2O \tag{3.3}$$

A typical etch rate of concentrated (49%) HF is about 1 µm/min at room temperature. An advantage of HF is that it also etches silicon nitride (at a faster rate than silicon dioxide). For more control on how much oxide is etched, HF can be diluted with deionised water to decrease the etch rate. Furthermore, in many industrial processes, buffered HF is used since the addition of ammoniumfluoride to diluted HF guarantees a constant level of fluorine ions and consequently a stable, relatively slow etch rate. This balance can be formulated as follows:

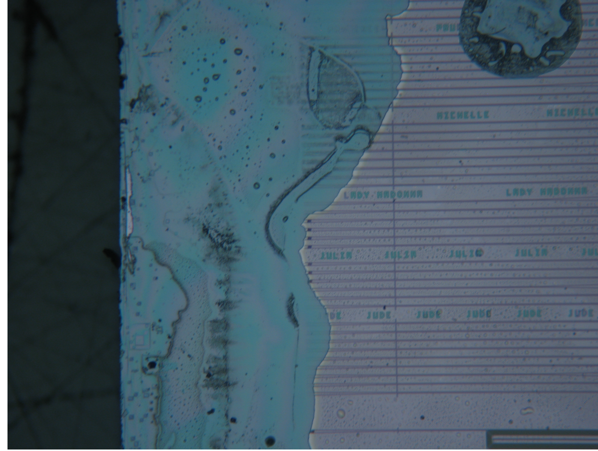

Figure 3.15: When no photoresist coating is applied during opening of the mask layer using reactive ion etching, the top protection layer is also etched away at the borders, leaving the silicon vulnerable for KOH.

$$NH_4F \leftrightarrow NH_3 + HF \qquad (3.4)$$

We have however seen in experiments that buffered HF can induce roughness in the silicon, as can be seen in Figure 3.16. This has also been observed by [24]. Since this roughness can have a negative impact on the optical properties of our photonic devices (in particular the very fabrication-sensitive photonic crystals), we chose for unbuffered hydrogen fluoride. Furthermore, since we need to remove the entire buried oxide layer and top layers, we have no need for accurate control of the etch rate and are able to use concentrated HF which brings the total etching time to about 4 minutes. The device side of the SOI die is protected by bonding it to a small piece of blank silicon using thin film bonding wax [25] which is removed after the HF etch.

A problem that may arise when processing certain photonic structures using liquids is that of stiction [26]. Conventional 2D photonic crystals do not suffer from this problem because they form a mechanically rigid structure (see Figure 3.18). Structures like the one in Figure 3.17 are not as rigid and wet etching can alter the topography: during drying of the liquid, capillary forces can pull the small silicon wires towards each other. Depending on several material parameters (e.g. spring constant), the wires can remain stuck to each other after the liquid has dried. Another similar drawback of wet etching is that other unprotected structures on the die will also be etched and loose silicon parts float around in the HF mixture, with a chance that they end up on the structure of interest. A particular example of this is tiling, a technique used in the semiconduc-

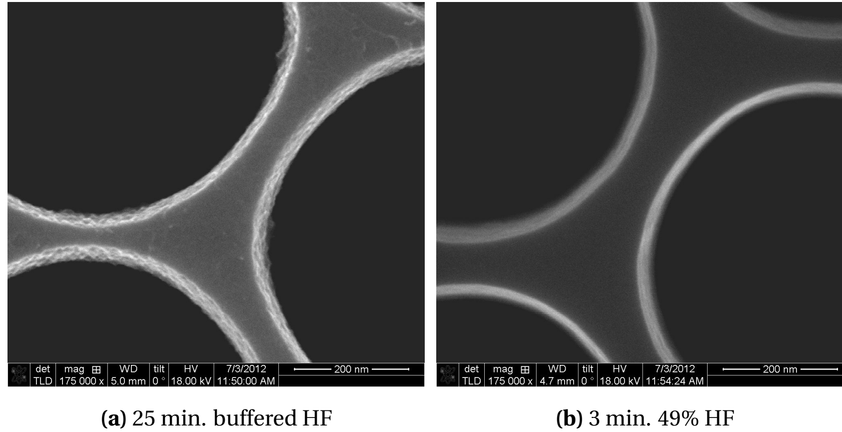

(a) 25 min. buffered HF **(b)** 3 min. 49% HF

Figure 3.16: Buffered HF slowly etches silicon which can induce roughness.

tor industry to improve the etching uniformity when defining the structures in the top silicon layer. When tiles in the surroundings of the photonic structure are underetched (e.g. because the hole in the silicon was too large) they may end up sticking to other parts of silicon as shown in Figure 3.19.

To circumvent the above-mentioned problem of stiction, we considered the use of vapour HF. The rationale behind this process is that we still use HF as an etchant but in a vapour phase, so no liquid comes into play which could damage our photonic structures. The die is clamped to an electromechanical chuck which is then turned upside down over a reservoir of concentrated HF. The vapour produced by this concentrated HF reaches the die and etches the silicon dioxide. Offenberg [27] states that the etching of silicon dioxide occurs through reaction equations (3.5).

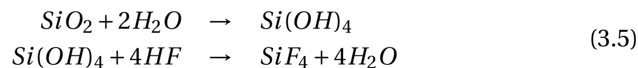

$$\begin{aligned} SiO_2 + 2H_2O &\rightarrow Si(OH)_4 \\ Si(OH)_4 + 4HF &\rightarrow SiF_4 + 4H_2O \end{aligned} \tag{3.5}$$

We see that water is here not only a product but also initiates the first reaction of forming silanol groups. It is clear that the amount of water adsorbed to the die will therefore influence the etching rate. Indeed, it is verified by Witvrouw [28] that both the temperature of the die and the die preparation (i.e. baking in order to evaporate adsorbed water) are key factors in vapour HF etching. In most vapour HF systems, the temperature of the die is controlled by means of the electromechanical chuck to which the die is clamped. Controlling the etch rate of a vapour HF system is not straightforward but, as mentioned before, the actual etch rate of the silicon dioxide is of no real importance to us so the process required minimal fine-tuning. After approximately 30 minutes,

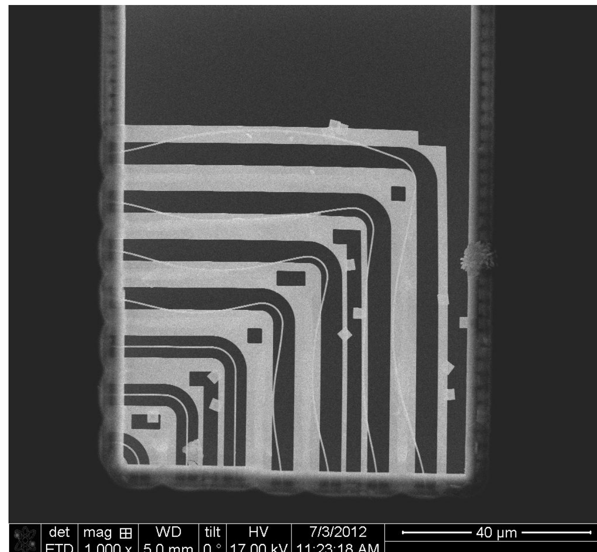

Figure 3.17: When drying a die after wet processing, the liquid can pull the small silicon wires towards other silicon structures where they stick after drying of the liquid, rendering the photonic structure useless.

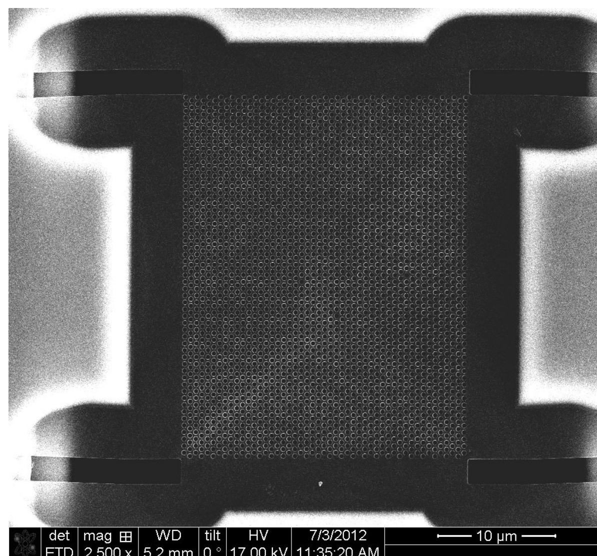

Figure 3.18: 2D photonic crystals can be easily etched using liquid HF. The top silicon dioxide and silicon nitride are also etched locally as seen in this picture taken from the device side.

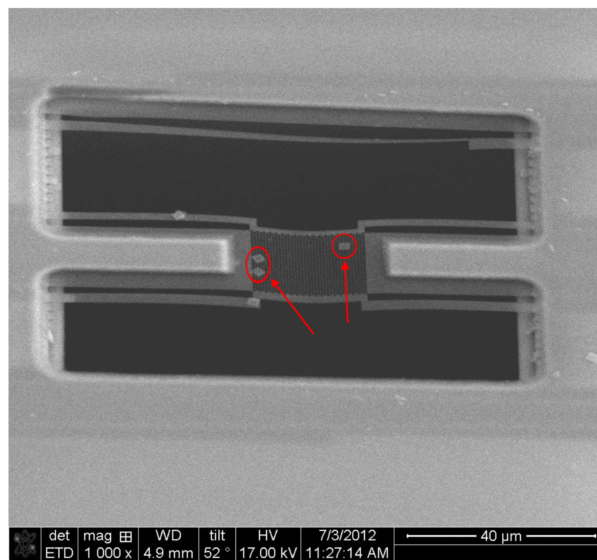

Figure 3.19: Tiling, a technique used in CMOS industry to improve etch uniformity, should be avoided in the neighbourhood of underetched structures: tiles are released due to removal of the silicon dioxide and can redeposit on the photonic structure after drying, causing additional scattering losses.

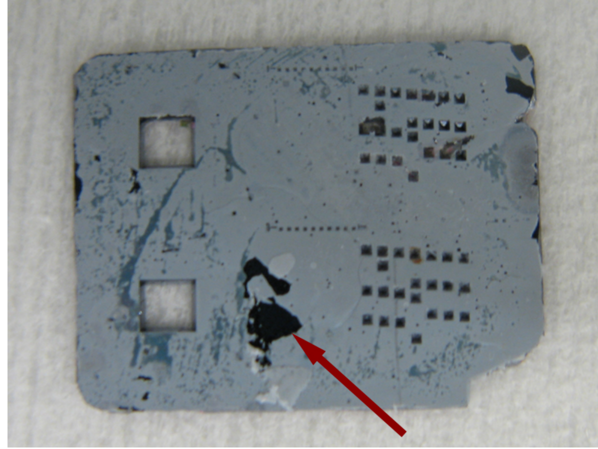

Figure 3.20: Example of the residue after silicon nitride etching with vapour HF. Part of the residue has come loose next to the big bottom left square.

our samples were etched.

We also have to take into account the fact that the device side of the die is not completely protected from the vapour by electromechanical clamping in the vapour HF system. It is however difficult to find a suitable material that protects against vapour HF and is easily removed afterwards [29], e.g.: standard photoresist, which protects the device layer of the die up unto a certain extent in liquid HF, is easily penetrated by the vapour. In practice, we noticed that by using no additional protective layer, we did see removal of the silicon oxide and silicon nitride at the edges of the die but due to the fact that there was a blank silicon border around our photonic structures, this caused no problems for the functionality of the device.

Vapour HF also etches silicon nitride but leaves a residue (which it does not for silicon dioxide), based on the following reaction equation [30]:

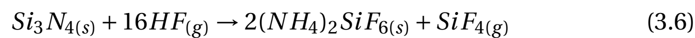

$$Si_3N_{4(s)} + 16HF_{(g)} \rightarrow 2(NH_4)_2SiF_{6(s)} + SiF_{4(g)} \tag{3.6}$$

A photograph of this residue can be seen in Figure 3.20 where part of the residue has been loosened next to the big bottom left square by simply scratching it with a pair of tweezers.

The solid residue from reaction equation (3.6) can be removed by immersing the die in water but this would however reintroduce the problem of stiction. Another way of getting rid of the residue is by heating up the die to a temperature of over 100 °C. Above this temperature, the following decomposition takes place:

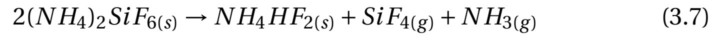

$$2(NH_4)_2SiF_{6(s)} \rightarrow NH_4HF_{2(s)} + SiF_{4(g)} + NH_{3(g)} \quad (3.7)$$

It is possible to avoid the liquid phase of $NH_4HF_{2(s)}$ and directly sublimate this component by performing this reaction at a pressure below 4 kPa (i.e. in a vacuum oven). In our experiments, we found that the vacuum was not really necessary and by simply putting the die on a hot plate in atmospheric conditions, the residue vaporised without causing stiction to the structures. Some structures did break but we observed this phenomenon as well in our experiments with the vacuum oven so concluded that this problem probably originated in prior steps.

An alternative to using vapour HF is to rely on critical point drying: conventionally, when a liquid dries, it converts from liquid to gas at a finite rate. However, for certain combinations of temperature and pressure, a distinction between liquid and gas can no longer be made and we are said to be in the supercritical phase. By going from the liquid to the supercritical to the gas phase, we avoid the direct transition from liquid to gas and can avoid stiction, caused by capillary forces. Advantages of this approach over vapour HF are that there is no longer a residue when etching silicon nitride and other liquids than HF (e.g. a Piranha solution) could be used. Since a critical point dryer was not readily available to us and vapour HF also suited our needs, we did not pursue this route.

After removal of the silicon dioxide and silicon nitride layers we obtain 220 nm thin silicon membranes. During the fabrication of SOI wafers, stress is introduced in the silicon layer due to the different thermal expansion coefficients of silicon and silicon dioxide [31]. This stress, typically ranging from 10-100 MPa [32], can cause the silicon membranes to buckle (i.e. deflect out of the wafer plane) which we observed frequently in our devices. This effect is undesired since large stresses, and as a consequence buckling, alters the refractive index of silicon and its geometry in a non-uniform manner. Figure 3.22a shows the top of a silicon die under relatively low stress (only part of the oxide layers have been removed). Already due to the large ratio of membrane size/thickness, linear buckling occurs, i.e. where the buckling pattern is circular/elliptical. Ziebart [13] has shown that when increasing the stress (e.g. by removing the oxide layers and decreasing the membrane thickness), non-linear buckling can occur, leading to the cross shaped pattern of Figure 3.22b. To avoid this problem of buckling, one can choose to alter the design of the photonic structure so that its mechanical properties are tuned to minimise buckling [32] or stress engineer the top silicon nitride layer so that it compensates the compressive stress of the silicon dioxide with tensile stress. As mentioned in Chapter 2, the functionality of photonic crystals can suffer greatly from distortions of its uniformity. On the other hand, in e.g. Mach-Zehnder interferometers, the buckling behaviour is

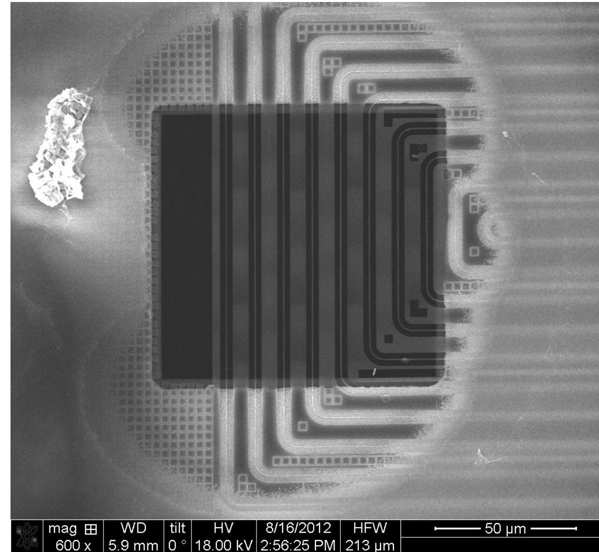

Figure 3.21: Vapour HF enables us to circumvent the problem of stiction as can be seen in this underetched delay spiral of a Mach-Zehnder interferometer.

much less of an issue since we simply wish to monitor the shift of the spectral features and some tolerance is allowed on their absolute position.

3.4 Conclusions

We have implemented a process for anisotropically etching the silicon substrate of SOI dies in our clean room facilities. One of the major advantages of this process is that, although the processing in this work is carried out on individual dies, it is possible to execute the entire flow on wafer-scale with a total processing time, from patterned and thinned dies/wafer to finished devices, of around 9 hours in our facilities. As can be gathered from the above, there are many pitfalls and factors to consider in this process. Problems of stiction and mask adhesion have been described here and we have proposed a solution. The problem of buckling is not very critical for many of our structures and is therefore not further investigated but can be the subject of future work. The process itself can also be fine-tuned further, e.g. by using better quality PECVD silicon nitride or by simply using LPCVD silicon nitride. For industrial applications, dry etching is preferred over wet etching (due to yield and process control considerations) and implementing a Bosch dry etching process [5] would be a next step in improving the fabrication of thin silicon membranes. A step-by-step process flow

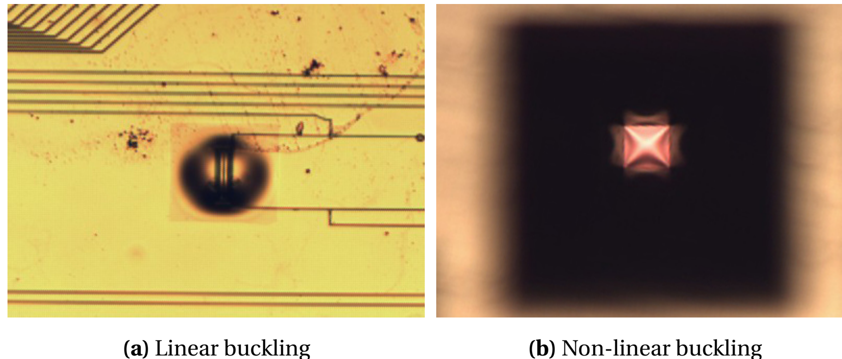

(a) Linear buckling (b) Non-linear buckling

Figure 3.22: When the membrane experiences high stress, the circular, linear buckling pattern can change into a cross shaped, non-linear one.

summarising this chapter can be found in Appendix A.

References

[1] P. Dumon, W. Bogaerts, V. Wiaux, J. Wouters, S. Beckx, J. Van Campenhout, D. Taillaert, B. Luyssaert, P. Bienstman, D. Van Thourhout, and R. Baets. *Low-Loss SOI Photonic Wires and Ring Resonators Fabricated With Deep UV Lithography.* IEEE Photonics Technology Letters, 16(5):1328–1330, 2004.

[2] S. Stankovic. *Hybrid III-V/Si DFB Lasers Based on Polymer Bonding Technology.* PhD thesis, Ghent University, 2013.

[3] S. K. Selvaraja. *Wafer-Scale Fabrication Technology for Silicon Photonic Integrated Circuits.* PhD thesis, Ghent University, 2011.

[4] D. Vermeulen, S. Selvaraja, P. Verheyen, G. Lepage, W. Bogaerts, P. Absil, D. Van Thourhout, and G. Roelkens. *High-efficiency fiber-to-chip grating couplers realized using an advanced CMOS-compatible Silicon-On-Insulator platform.* Optics Express, 18(17):18278–18283, 2010.

[5] F. Laermer and A. Schilp. 2003.

[6] Y. Tzeng and T. H. Lin. *Dry etching of silicon materials in SF6 based plasmas.* Journal of Electrochemical Society, 134(9):2304–2309, 1987.

[7] X. G. Zhang. *Electrochemistry of Silicon and its Oxide.* Springer, 2004.

[8] MicroChemicals. 2012.

[9] H. Seidel, L. Csepregi, A. Heuberger, and H. Baumgärtel. *Anisotropic Etching of Crystalline Silicon in Alkaline Solutions - Orientation Dependence and Behavior of Passivation Layers*. Journal of Electrochemical Society, 137(11):3612–3626, 1990.

[10] M. Shikida, K. Sato, K. Tokoro, and D. Uchikawa. *Differences in anisotropic etching properties of KOH and TMAH solutions*. Sensors and Actuators A: Physical, 80:179–188, March 2000.

[11] ePIXfab, *http://www.epixfab.eu/*.

[12] S. H. Lee, D. H. Kim, H. D. Yang, S. J. Kim, D. W. Shin, S. H. Woo, H. J. Lee, H. M. Seung, S.-K. Lee, G.-S. Lee, and J.-G. Park. *Thin transparent Single-Crystal Silicon Membranes Made Using a Silicon-on-Nitride Wafer*. Journal of the Korean Physical Society, 53(2):579–583, 2008.

[13] V. Ziebart, O. Paul, and H. Baltes. *Strongly buckled square micromachined membranes*. Journal of Microelectromechanical Systems, 8(4):423–432, 1999.

[14] Dow MicroChemicals. *Gold Etching*. Technical report, Dow MicroChemicals, 2009.

[15] Brewer Science, *http://www.brewerscience.com/protek-psb*.

[16] E. Hallynck and P. Bienstman. *Integrated Optical Pressure Sensors in Silicon-on-Insulator*. IEEE Photonics Journal, 4(2):443–450, 2012.

[17] Z. Y. Dang, M. Motapothula, Y. S. Ow, T. Venkatesan, M. B. H. Breese, M. A. Rana, and A. Osman. *Fabrication of large-area ultra-thin single crystal silicon membranes*. Applied Physics Letters, 99(22):223105, 2011.

[18] Dow Chemicals. 2005.

[19] T.-J. Hwang, D. O. Popa, B.-H. Kang, J.-Q. Lu, and H. E. Stephanou. *BCB wafer bonding compatible with bulk micro machining*. In International Electronic Packaging Technical Conference and Exhibition, pages 1–7, 2003.

[20] A. Stoffel, A. Kovacs, W. Kronast, and B. Müller. *LPCVD against PECVD for micromechanical applications*. Journal of Micromechanics and Microengineering, 6:1–13, 1996.

[21] S. Beeby, G. Ensell, M. Kraft, and N. White. *Mems Mechanical Sensors*. Artech Print on Demand, 2004.

[22] V. Lindroos, M. Tilli, A. Lehto, and T. Motooka. *Handbook of Silicon Based MEMs Materials and Technologies.* William Andrew, 2010.

[23] M. Saadaoui, D. Peyrou, H. Achkar, F. Pennec, L. Bouscayrol, B. Rousset, P. T. Boyer, E. Scheid, P. Pons, and R. Plana. *Plasma-enhanced chemical vapor deposition of silicon oxynitride for micromachined millimeter-wave devices.* Journal of Micromechanics and Microengineering, 18(3):035032, 2008.

[24] G. S. Higashi, Y. J. Chabal, G. W. Trucks, and K. Raghavachari. *Ideal hydrogen termination of the Si (111) surface.* Applied Physics Letters, 56(7):656–658, 1990.

[25] Logitech, *http://www.logitech.uk.com/.*

[26] J. Roels. *Actuation of integrated nanophotonic devices through the optical gradient force.* PhD thesis, Ghent University, 2011.

[27] M. Offenberg, B. Elsner, and F. Lärmer. *Vapour HF etching for sacrificial oxide removal in surface micromachining.* In Electrochemical Society Fall Meeting, pages 1056–1057, Miami Beach, 1994.

[28] A. Witvrouw, B. Du Bois, P. De Moor, A. Verbist, C. Van Hoof, H. Bender, and K. Baert. *A comparison between wet HF etching and vapor HF etching for sacrificial oxide removal.* In SPIE, Santa Clara, CA, 2000.

[29] T. Bakke, J. Schmidt, M. Friedrichs, and B. Völker. *Etch Stop Materials for Release by Vapor HF Etching.* In 16th MME Workshok, pages 1–4, Sweden, 2005.

[30] B. Du Bois, G. Vereecke, A. Witvrouw, P. De Moor, C. Van Hoof, A. De Caussemaker, and A. Verbist. *HF Etching of Si-oxides and Si-nitrides for surface micromachining.* Technical report, imec.

[31] S. Y. Dhumal and S. Kommu. *A Theoretical and Experimental Study of Stresses Responsible for the SOI Wafer Warpage.* Journal of Electrochemical Society, 16(6):57, 2008.

[32] E. Iwase, P.-C. Hui, D. Woolf, A. W. Rodriguez, S. G. Johnson, F. Capasso, and M. Loncar. *Control of buckling in large micromembranes using engineered support structures.* Journal of Micromechanics and Microengineering, 22(065028), 2012.

*"Do something... Do something. You phony, prick, fraudulent motherfucker. Do something! Come on! Prove it! Fuck faith! Earn it! Show me something real! I need it now! Not later! Now! Show me and I'll believe in you until the day I die. I swear. I'm calling on you. I'm calling on you! ...
Fuck it, I'll do it myself."*

Liam Neeson in The Grey, Actor, 1952-present

4
Digital microfluidics with pressure-based actuation

Using the process flow described in Chapter 3, we can create silicon membranes with holes through which the liquid can flow, circumventing the problem of laminar flow parallel to the sensor surface as described in Chapter 1. This chapter starts with a theoretical section where we will try to get an estimate of the pressure needed to transport a droplet through the silicon membrane, after which we will verify this using simulations. After that, we will highlight the measurement setup that was used to characterise the sensors. Finally we will show measurement data that indicates that the proposed flow scheme does indeed improve analyte delivery by at least a factor of 3.

4.1 Theory

It can prove to be very difficult to get a thorough understanding of microfluidics. The main reason for this is probably the fact that it can be at times counter-intuitive: consider a 10 mm-diameter Teflon pipe with a water reservoir on top of it. When opening the valve between the pipe and the reservoir, all water will flow through the pipe and fall out at the bottom as we would expect. If we now change the diameter of the pipe to 1 μm and change the reservoir by a droplet of about 10 μl, the droplet will not simply flow through the pipe and fall out at the

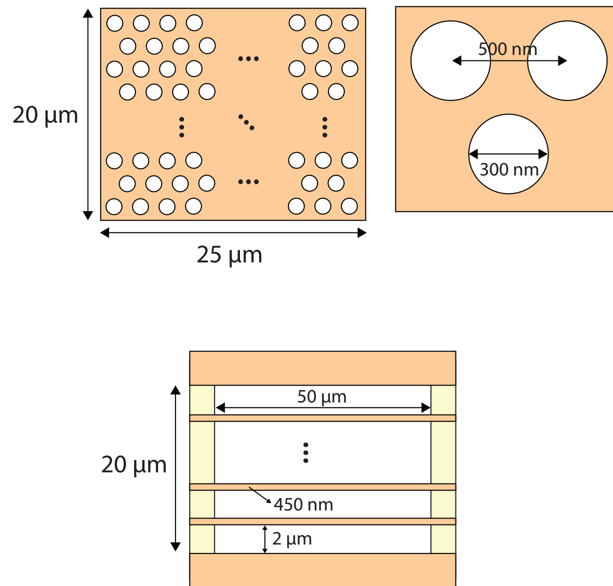

Figure 4.1: Typical dimensions of a photonic crystal membrane (top) and part of a delay spiral of a Mach-Zehnder interferometer (bottom).

bottom. The reason for this difference is that in everyday life fluidics are mainly dominated by volume forces where gravity plays a dominant role. In microfluidics however, the amount of covered surface by a liquid is usually much more important than the actual volume of the liquid. Surface forces become dominant, with the most important force in this work being surface tension. We can therefore not simply assume that, when applying a droplet on our biosensor, everything will just flow through the sub-micron size holes of a photonic crystal or trenches of a delay spiral. In the following, we will, in parallel, consider two structures: one is a photonic crystal membrane and another is part of a delay spiral of a Mach-Zehnder interferometer (MZI). Both structures are shown in Figure 4.1 with their typical dimensions. Before we start investigating how a droplet will behave when introduced in the sensor we take a brief look at the concept of surface tension. For more information, we refer to the book Theoretical Microfluidics by Henrik Bruus [1].

4.1.1 Surface tension

Surface tension is a force that arises at the interface between materials in two different aggregation states. Figure 4.2 shows the interface between a gas and a

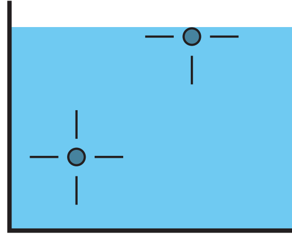

Figure 4.2: Molecules near the surface miss chemical bonds in the direction of the surface, contrary to molecules in the bulk of the liquid. This causes the surface molecules to have a higher energy and results in surface tension.

liquid. In the bulk of the liquid, molecules are chemically bound to their neighbours (e.g. 6 in a cubic geometry). At the surface/interface, the molecules do not have bonds in the direction perpendicular to the surface since the density of a gas is very low. As a consequence, the surface molecules will have a higher energy. The liquid will try to minimise its energy by minimizing the surface area. The force that minimises the area is called surface tension, expressed as a force per length unit [N/m = J/m^2]. A typical value for a water/air interface at 20°C is 72.9 mJ/m^2. Mercury has a relatively high value of 486.5 mJ/m^2 at the same temperature [1].

Because surface tension is a force, we can also associate a pressure with it. The Young-Laplace pressure drop, defined as the pressure drop over a gas/liquid interface, is given by:

$$\Delta p_{surf} = \left(\frac{1}{R_1} + \frac{1}{R_2}\right)\gamma \tag{4.1}$$

Here, γ is the surface tension and R_1 and R_2 are the curvature radii in the two orthogonal tangent directions at a point on the surface [m].

A droplet surrounded by gas will try to minimise its area by contracting into a sphere (if we do not take gravity or drag forces into account). However, when a droplet is resting on a solid surface, this will not be the case since we have to take into account the influence of this third phase. At the point where the three phases come together, the droplet will take the form of a sphere segment with a specific contact angle θ (see Figure 4.3). Depending on the surface of the solid this contact angle will change. In Figure 4.3 we can see the difference between a hydrophilic (left) and hydrophobic (right) surface. A surface is called hydrophilic for a certain liquid when the contact angle θ is smaller than 90°; it is called hydrophobic when the contact angle is greater than 90°(and smaller

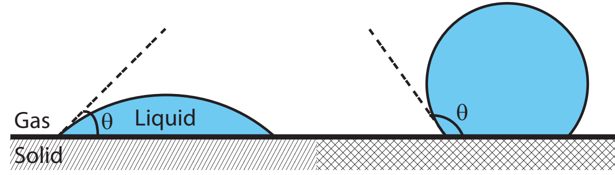

Figure 4.3: A contact angle is formed at the point where three phases (solid, liquid and gas) come together. The value of this angle θ depends on the different material parameters. The left droplet is placed on a hydrophilic surface ($\theta < 90°$) and the right droplet on a hydrophobic surface ($\theta > 90°$).

than the limit of 180°). For water on a glass surface, the contact angle is approximately 0° and we say that full wetting occurs. Changing the surface to e.g. Teflon can drastically change the contact angle: from almost 0° to 115°.

It can be proven that the contact angle is given by the following equation [1]:

$$\cos\theta = \frac{\gamma_{sg} - \gamma_{sl}}{\gamma_{lg}} \tag{4.2}$$

where γ_{sg} is the surface tension between gas and solid, γ_{lg} the surface tension between gas and liquid and γ_{sl} the interface tension (the tension between two non gaseous substances) between solid and liquid phases.

Two common phenomena that we encounter on a daily basis and that are the consequence of surface tension are capillary forces and pendant droplets (see Figure 4.4). In a capillary (i.e. a tube with small diameter), the water level will be either higher or lower than in the reservoir where it is introduced, depending on whether the capillary is hydrophilic or hydrophobic respectively. For a cylindrical capillary and based on the assumptions made in Figure 4.4 (left) we can calculate that the level difference is given by the following formula:

$$H = \frac{2\gamma}{\rho g a}\cos\theta \tag{4.3}$$

where γ is the surface tension between liquid and gas, ρ is the mass density of the liquid, g is the gravitational acceleration, a the radius of the capillary and θ the contact angle of the liquid with respect to the solid and the gas.

For a pendant droplet as in Figure 4.4 (right), we can see that the droplet will remain pendant as long as the mass is low enough so that the force resulting from surface tension is stronger than the gravitational pull. When the droplet mass is small, the gravitational effect expressed by $F_{grav} = \rho V g$ can be neglected and the droplet will look like a spherical cap. Inside the droplet there is an underpressure defined by equation (4.1) which can be seen as a net force

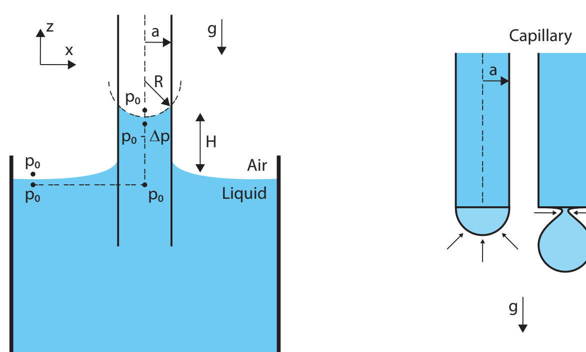

Figure 4.4: Two phenomena that can be explained through surface tension: capillary rise and a pendant droplet.

trying to push the droplet against the solid medium. When we would start to increase the mass through the capillary, the droplet will start to expand, increasing its surface area and as a consequence also the upward directed surface force. At a certain point, the droplet will become spherical and the external overpressure will pinch off the droplet, making it fall from the capillary. At the moment this happens, the following formula holds:

$$mg = 2\pi a\gamma \tag{4.4}$$

where γ is the surface tension between liquid and gas, m is the mass of the droplet, g is the gravitational acceleration and a the radius of the capillary. This experiment is frequently used to determine the surface tension of liquids, provided that the mass of the fallen droplet can be measured.

4.1.2 Equilibrium in an underetched membrane

Using the concept of surface tension, we will try to investigate how a droplet will interact with a thin membrane with holes: will the droplet remain on top of the membrane due to surface tension or will it go through and will it reach an equilibrium state? We start off with a dry sample and apply a droplet of analyte on top of the sensor. A first distinction that we have to make is between the case where the droplet radius is the same order of magnitude as the membrane with holes (because of a large membrane or a small droplet; Figure 4.5 (left)) and the case where the droplet is much larger than the sensor (Figure 4.5 (right)). In the latter case, the surface can be approximated by a smooth surface but in the former case, the non-uniformities introduced by the holes in the membrane

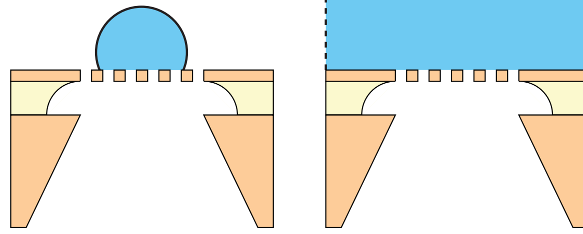

Figure 4.5: Depending on the ratio of the droplet size to the membrane size, we have to take into account surface non-uniformity, formulated by Cassie's law.

have to be taken into account. It is possible in such a case that, even though the material itself is hydrophilic, the non-uniformity changes the effective contact angle to one of more than 90°. This is expressed by Cassie's law [2]:

$$\cos\theta_{eff} = \phi_1 \cos\theta_1 + \phi_2 \cos\theta_2 \tag{4.5}$$

This law formulates the effective contact angle when two liquids or surfaces with different properties are combined in creating a rough surface, where ϕ_i is the areal fraction of the liquids and θ_i their contact angle to a normal uniform surface (i.e. Young's contact angle); note that here we use the term non-uniformity to indicate the topography of the photonic structures and not the smaller-scale material roughness induced by etching. In our case, the membrane holes are filled with air when the droplet is applied so we treat air as our second liquid (with $\theta_2 = 180°$) and the droplet of analyte as the first liquid. Using $\phi_1 + \phi_2 = 1$, we can rewrite equation (4.5) as:

$$\cos\theta_{eff} = \phi(\cos\theta + 1) - 1 \tag{4.6}$$

In the above formulation $\phi_1 = \phi$ and $\theta_1 = \theta$. For a unit cell in the photonic crystal $\phi = 0.717$, for a unit cell of the delay spiral (i.e. one waveguide and one trench) ϕ=0.184. From Figure 4.6 we see that in the case of the delay spiral, no matter what the contact angle, the surface will be hydrophobic.

In the following, we work with membranes in the order of microns thick and with sample volumes in the order of microlitres. As a consequence, the droplet has much bigger dimensions than the membranes and we can assume $\phi \approx 1$, thus neglecting the Cassie effect (i.e. effective contact angle ≈ Young's contact angle).

Another two cases should be distinguished at this point (see Figure 4.7): that of the hydrophilic and that of the hydrophobic material. For the hydrophilic

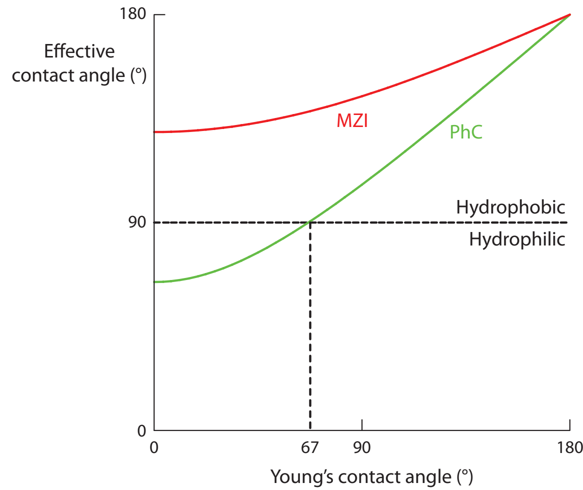

Figure 4.6: The Cassie effect can render a hydrophilic structure hydrophobic. In the case of the delay spiral the non-uniformity will create an inherently hydrophobic structure.

case, we will take as an example a contact angle of 22°, that of water on blank silicon; for the hydrophobic case, we choose 115°, the contact angle of water on Teflon. As will become apparent later on, it is possible to change the surface properties of a material (e.g. silicon) by chemical modification. Electrical modification (i.e. electrowetting [3]) is also possible but lies outside the scope of this work. We will also work with a droplet volume of 5 µl, which is the volume used in our experiments.

Neglecting deformation of the droplet by gravity and the Cassie effect, we can approximate the droplet by a sphere segment with Young's contact angle. We then can calculate the radius of the droplet on the hydrophilic surface to be 3.637 mm and on the hydrophobic surface 1.202 mm. This corresponds with our intuition that a droplet on a hydrophobic surface is more compact. Note that the size of these droplets compared to the membrane size of our sensors is a few orders of magnitude larger so we can assume that we will never reach a point where the entire droplet is pulled through one membrane. Using the formula to calculate the Young-Laplace pressure drop (equation (4.1)) across the interface gas/liquid we get a value of 40 Pa ($= p_0^* - p_0$) for the hydrophilic case and 121 Pa for the hydrophobic case for water at 20°C ($\gamma = 72.9$ mJ/m^2). The pressure build-up inside the droplet can be determined from the height of the droplet and is found to be 2.6 Pa and 16.8 Pa for the hydrophilic and hydrophobic case respectively. A last pressure drop that has to be determined is that at

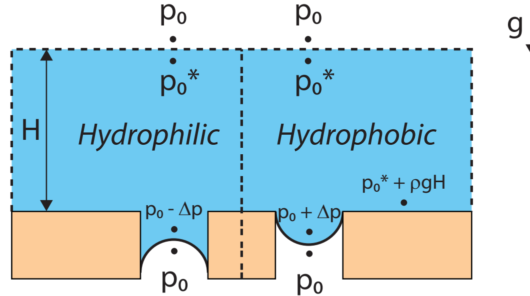

Figure 4.7: Depending on the hydrophilic or hydrophobic character of the surface, the situation on the left or the right will arise respectively.

the liquid-gas interface in the holes. Again using equation (4.1), we obtain for one of the photonic crystal holes a pressure drop of 9.01×10^5 Pa or 9.01 bar for the hydrophilic case and 4.11 bar for the hydrophobic case. It is clear that this is the dominant force compared to the first two effects.

Initially, there is a great pressure inequality in the photonic crystal holes: according to hydrostatics, the pressure just above the meniscus (i.e. the curved liquid-gas interface) should be $p_0^* + \rho g H$ where H is the local height of the droplet. Surface tension, however, dictates that the pressure should be $p_0 - \Delta p$ and $p_0 + \Delta p$ for the hydrophilic and hydrophobic situation respectively. Considering the hydrophilic case (the reasoning is similar for the hydrophobic case), the pressure difference $\left(p_0^* + \rho g H\right) - \left(p_0 - \Delta p\right)$ will cause the liquid to be pushed through the holes as would be the case for a capillary standing in a water basin as shown in Figure 4.4. Since in that case the liquid advances in the direction opposite to gravity, an equilibrium will be achieved due to the fact that downward gravity and upward capillary rise counteract. In our situation on the other hand, capillary "rise" and gravity point in the same direction, thereby enforcing each other. Assuming that the photonic crystal holes are infinitely long, no equilibrium will be reached. Indeed, if the meniscus advances inside the holes by a distance d, the hydrostatic pressure at the meniscus inside the liquid will have increased by an amount $\rho g d$, creating an even greater pressure difference $\left(p_0^* + \rho g (H + d)\right) - \left(p_0 - \Delta p\right)$ that drives the liquid. However, as we have seen, the pressure drop due to surface tension is a few orders of magnitude larger than the hydrostatic pressure and it can therefore be assumed that the effect of gravity is negligible. So without exerting any pressure (i.e. pulling the droplet through from beneath) the droplet goes through the holes. From an intuitive point of view this can be explained by saying that the hydrophilic character causes the droplet to look for more surface to expand its area and at the

same time is marginally being helped by gravity, thereby illustrating the dominance of surface over volume forces on these length scales.

If we now look at the hydrophobic case, we see that we first would have to overcome a large overpressure inside the droplet before it can pass through the holes. In practice, these pressure values are not easily reached using standard equipment and can be high enough to damage the sensor mechanically. It is therefore imperative that we deal with hydrophilic surfaces. Luckily, water on silicon is hydrophilic (θ=22°) and we will see later on that we can improve the hydrophilic character even further.

For the case of the delay spiral, the shape of a small droplet between two arms is not easily defined. If we, however, approximate the rectangular cross-section by an ellipse with the length of its axes equal to the lengths of the rectangle we have an estimate on the pressure values involved. Since the length of the openings is much larger than the width (50 μm compared to 2 μm) we can approximate the effective radius by 1 μm (half the width). The pressure drop is almost an order of magnitude smaller now (1.35 bar and 0.62 bar for the hydrophilic and hydrophobic case respectively) but they are still the dominant forces. Overcoming the hydrophobic pressure drop is no longer a major issue but nevertheless, hydrophilic surfaces are still the preferred choice. In the following, we will limit ourselves to hydrophilic surfaces, unless stated otherwise.

Both for the photonic crystal and the Mach-Zehnder interferometer, the droplet will push itself through the different holes in parallel. The resulting droplets at the bottom side of the membrane/etching pit, whose shapes are still determined by the contact angle, will merge together into one big droplet with the dimensions of the membrane. Note that, although the droplet size is now comparable to the membrane dimensions, the Cassie effect has no negative impact since there is no more air in the holes. The droplet will continue to grow until it reaches the sides of the etched region directly under the membrane. The sides of this region are not made of silicon but silicon dioxide, a highly hydrophilic material for water (the contact angle can be approximated as being 0°, i.e. full wetting occurs). If we again approximate this rectangular region by an ellipse with the dimensions of an underetched photonic crystal, we can calculate that the pressure drop has decreased to 0.26 bar. Since the droplet has only propagated a few extra microns, the hydrostatic pressure will only have increased by at most a few mPa and we are still far from an equilibrium (the hydrostatic pressure build-up over the entire sample thickness, i.e. 250 μm, is only 0.2 Pa). The droplet will now continue to the trapezoidal etching pit in the silicon substrate. At the substrate surface, where the etching pit is at its widest, the dimensions are 374 μm by 379 μm. Using the same elliptical approximation, the pressure drop has drastically decreased to 718 Pa. Leaving the etching pit, the droplet will spread out over the substrate (and in eventual cases

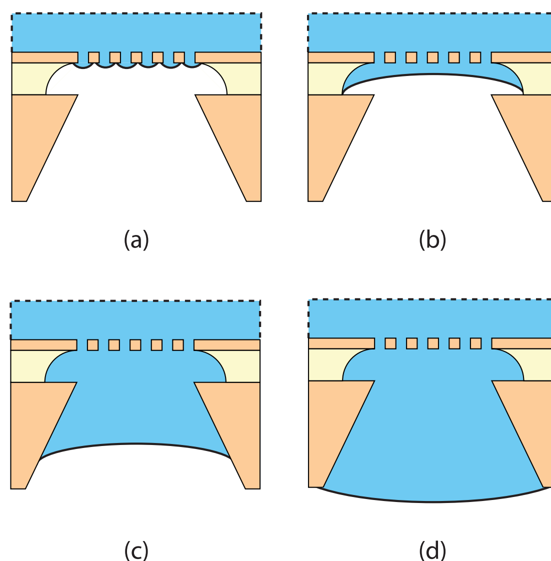

Figure 4.8: Schematic overview of droplet propagation through a membrane with holes in a hydrophilic device (note that the size ratios are not accurate in these illustrative snapshots). (a) Minidroplets are pushed through the small holes under a large pressure. (b) They merge into a bigger droplet and propagate to the highly hydrophilic silicon dioxide region. (c) The big droplet propagates further through the trapezoidal silicon etching pit. (d) When the droplet reaches the substrate surface it will increase its radius in order to reach an equilibrium.

might merge with other droplets, coming through other etching pits) where it can freely adjust its radius as to obtain an equilibrium. We can validate our assumption that not the entire droplet will be pulled through one etching pit by calculating its volume. The underetched region in the silicon dioxide can hold 1 pl (= 10^{-6} μl) and the trapezoidal silicon etching pit 18 nL (= 18×10^{-3} μl), well below the 5 μl mentioned in the beginning.

4.1.3 Flow through an underetched membrane

Since still a large portion of the analyte volume has not passed through the membrane holes, we would like to apply pressure as to create a flow. If we e.g. apply under pressure at the bottom of the droplet, an extra force will try to pull the droplet downwards. The droplet will react by trying to expand its surface

area (thereby increasing the magnitude of the counteracting surface force). For this increase in surface area, liquid is pulled from the top part of the droplet, through the small holes, towards the bottom part of the droplet. If the pressure difference between the top and bottom part is high enough, the entire droplet can be pulled through. Note that in large fluidic configurations (where volume forces are dominant) a constant pressure implies a constant flow since there is no counteracting force. When surface tension is involved, this will not be the case and a new equilibrium will be established where the droplet has expanded its surface area.

Assuming that at both the device and substrate side, there will always be a relatively large droplet (if not, we would have to counteract the capillary forces in the individual, small diameter holes), we know from calculations in the above that the Young-Laplace pressure drop for these droplets are in the order of tens of Pascals. The required pressure to increase the size of the substrate droplet, so that the fluid is transported from the device to the substrate device through the membrane holes, will therefore be in the same range. In practice, we will apply pressure gradients of about 10 kPa so we can be quite certain that we will be able to pull the entire droplet through, whereas e.g. a pressure difference of 10 Pa would only be able to increase the size of the substrate droplet up to a certain point where there is still liquid at the top side. Since the applied pressure difference is several orders of magnitude larger than the Young-Laplace pressure drop over the droplet shapes involved, we will neglect the effect of surface tension in this section and model the device as a series of channels.

A first way to approach this is to make use of Bernoulli's principle [4] that states

$$\frac{\rho v^2}{2} + \rho g z + p = constant \tag{4.7}$$

with ρ the density of the fluid, v the fluidic speed, g the gravitational constant, z the gravitational direction and p the pressure in a given point. If we neglect gravitational effects we can write

$$\begin{aligned} \frac{\rho v_1^2}{2} + p_1 &= \frac{\rho v_2^2}{2} + p_2 \\ &\Updownarrow \quad Q = A_1 v_1 = N \cdot A_2 v_2 \\ p_1 - p_2 &= \frac{1}{2}\rho\left(\frac{Q}{N\cdot A_2}\right)^2 - \frac{1}{2}\rho\left(\frac{Q}{A_1}\right)^2 \\ &\Downarrow \quad A_1 \approx \infty \\ p_1 - p_2 &= \frac{1}{2}\rho\left(\frac{Q}{N\cdot A_2}\right)^2 \end{aligned} \tag{4.8}$$

Here subscript 1 denotes the region before the holes (i.e. the device side of the sensor) and 2 denotes the region inside the holes (see Figure 4.9). A_2 is the projected area of one opening. The entire flow is accommodated by all holes in

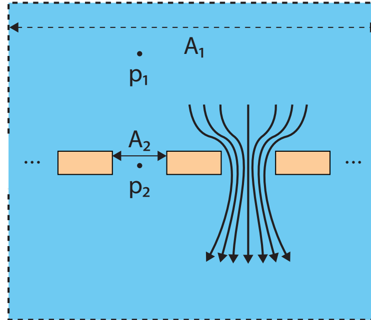

Figure 4.9: Bernoulli's principle relates the pressure and flow velocity between two points in the fluid. Note that this is an approximation since viscous forces are not taken into account.

parallel so the overall flow rate Q is determined by the total area $N \cdot A_2$ where N is the number of equivalent openings. Note that Bernoulli's principle does not take into account viscous forces so in reality, the pressure needed to reach a certain flow rate will be higher since it has to compensate for these viscous forces.

Assuming that the bottleneck of the flow is in the membrane holes (since that part of the structure comprises the least flow area), we only take that part into account to simplify our calculations. A typical photonic crystal with the dimension of Figure 4.1 consists of approximately 2000 holes. The total area is then 141.372 μm^2. To obtain a flow of 1 μl/s (which would transport a typical droplet of 5 μl in a matter of seconds), we need a pressure of 25 kPa. For the delay spiral of the MZI, we have 8 times a surface of 100 μm^2. The pressure needed here for the same flow rate is 0.78 kPa, much less than in the case of the photonic crystal. The reason why the difference is so great, is that the area $N \cdot A_2$ in the denominator of equation (4.8) is squared. So if the area is expanded by a factor of e.g. 6, the required pressure is 36 times less.

The problem with the above calculations is that, as mentioned, viscosity is not taken into account. Since the channel thickness (i.e. 220 nm) is thin compared to the hole dimensions, we might be able to neglect viscous forces. We shall verify this by calculating the required pressure using another method which does take viscous forces into account: the Hagen-Poisseuille flow: a pressure-driven, steady state flow in a channel. It can be shown [1] that by solving the Navier-Stokes equation [5] with a set of boundary conditions following from the fact that we have a pressure-driven, steady state flow, the flow rate Q can be linearly related to the pressure difference Δp through a factor R_{hydr}

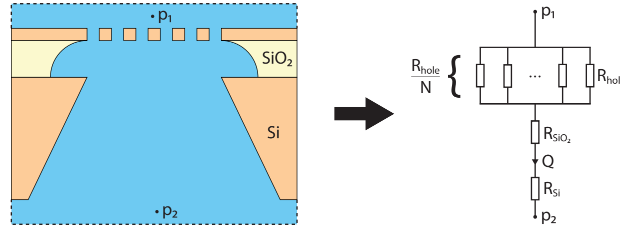

Figure 4.10: A Hagen-Poiseuille flow through a number of channels connected in parallel and/or series can be transformed into an equivalent electrical circuit where the hydraulic resistance of a channel is dependent on its geometry.

determined by the geometry of the channel:

$$\Delta p = R_{hydr} Q \tag{4.9}$$

Due to the analogy that can be drawn with Ohm's law (a linear relation between *current* flow and *voltage* difference) we call the proportionality factor the hydraulic resistance. A structure containing a set of channels (in parallel and/or series) can therefore also be modelled as an equivalent electrical circuit (see Figure 4.10). In our case the membrane with holes can be interpreted as a set of parallel, equal hydraulic resistors, which can be replaced by one equivalent resistor $R_{channel}/N$ where N denotes the number of parallel channels. This corresponds with the notion that an increasing number of channels will decrease the overall resistance, allowing more fluid to flow through. The other channels (i.e. in the silicon dioxide layer and the silicon substrate) are modelled as separate resistors placed in series after the equivalent resistor of the membrane holes. These can be transformed into one equivalent resistance for the entire structure R_{total}. The sign convention from electronics that states that current flows from a high to a low potential also holds here: the fluid is pushed away from a high pressure to a low pressure point. It can be proven [1] that the hydraulic resistance for a cylindrical channel (as is the case for the photonic crystal holes) is given by

$$R_{cyl} = \frac{8}{\pi} \mu L \frac{1}{a^4} \tag{4.10}$$

where μ is the dynamic viscosity of the fluid, L is the length of the channel and a is the radius. For a rectangular channel, the resistance is given by

$$R_{rect} = \frac{12}{1 - 0.63(h/w)} \mu L \frac{1}{h^3 w} \tag{4.11}$$

Here h is the short side of the rectangle and w the long side.

For one photonic crystal hole with the dimensions of Figure 4.1, the hydraulic resistance is 1.109×10^{18} Pa·s/m^3. Here, we have taken the value of 1.002 mPa·s for the viscosity of water [6]. To obtain the total resistance, we should divide this number by the number of holes (in this case 2000).On the other hand, the resistance of the region in the silicon dioxide is 2.667×10^{10} Pa·s/m^3, a few orders of magnitude smaller than the total resistance of the holes. We can therefore neglect the effect of the silicon dioxide and silicon substrate region and focus on the bottleneck: the membrane holes. To obtain a flow rate of 1 $\mu l/s$, a pressure of 0.554 MPa would be needed in the case of a photonic crystal. For a channel in the delay spiral of an MZI, the hydraulic resistance is 6.784×10^{12} Pa·s/m^3. For 8 such channels in parallel, the required pressure is 0.848 kPa, three orders of magnitude lower than the pressure needed for a photonic crystal. A pressure of 1 kPa is easily achieved but creating an under pressure of 0.554 MPa is not straightforward: since the atmospheric pressure is 0.1 MPa we can not achieve this pressure difference by creating a vacuum at the bottom side of the sensor; we would also have to increase the pressure at the top side of the sensor which could dramatically increase packaging costs. Therefore we will have to make do with a lower flow rate at a pressure which can be easily achieved. The pressure used in our experiments later on is chosen at 10 kPa which gives a flow rate of 0.02 µl/s for the photonic crystals. For the MZI delay spiral, this corresponds to a flow rate of 11.8 µl/s.

The value obtained here for the case of a photonic crystal differs greatly from the one obtained using Bernoulli's principle (554 kPa compared to 25 kPa) so it is advised to make use of the value obtained through equation (4.9) since viscosity is taken into account here. For the delay spiral, the difference is quite small. In the following we will see that this is most likely caused by an underestimation of viscous forces in the Hagen-Poiseuille model during development of the flow. Indeed, the linear relation between pressure and flow rate given by equation (4.9) only holds for a fully developed flow in a long channel. However, when the fluid enters the channel the velocity profile is uniform. Only gradually, over the length of the channel, the velocity profile will transform into a parabolic profile with a zero velocity component at the channel walls (see Figure 4.11). The length needed for a flow to develop in a channel is given by [7]:

$$\begin{aligned} Circular: L_{dev} &\approx \left[(0.619)^{1.6} + [(0.0567Re)^{1.6}\right]^{1/1.6} D_{eff} \\ Rectangular: L_{dev} &\approx \left[(0.631)^{1.6} + [(0.0442Re)^{1.6}\right]^{1/1.6} D_{eff} \end{aligned} \tag{4.12}$$

Here Re is the Reynolds number, a dimensionless quantity that basically gives the ratio of the inertial forces to the viscous forces, and D_{eff} the hydraulic channel diameter given by $4A/P$ where A stands for the cross-sectional area and P the wetted perimeter. The Reynolds number is defined as

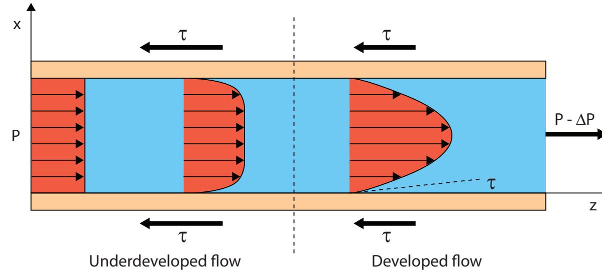

Figure 4.11: When a flow enters the channel, the velocity profile needs space to develop (i.e. the development length) from a uniform velocity profile to a steady-state parabolic profile where it truly becomes a Hagen-Poiseuille flow. During this development phase, viscous forces are greater than in steady-state.

$$Re = \frac{\rho v_{mean} D_{eff}}{\mu} \tag{4.13}$$

where v_{mean} is the mean velocity, ρ is the fluid density, D_{eff} the hydraulic diameter and μ the dynamic viscosity. In the case of the photonic crystal (where the flow rate at 10 kPa is 0.02 µl/s), the Reynolds number is 0.04 and the resulting development length is 186 nm. We can therefore state that our 220-nm-long channel will support a developed flow although 85% of the channel is used for flow development. In the case of the delay spiral, the Reynolds number is 59 for a flow rate of 11.8 µl/s, corresponding to a development length of 5.53 µm. The length of our channel is much less than that and it is therefore clear that the flow will be far from developed at the end of the channel. For a flow rate of 0.02 µl/s ($Re = 0.1$) the development length would still be 1.26 µm.

The penalty for an underdeveloped flow is that in practice more pressure will be required than calculated using the hydraulic resistance for a developed flow. This can be explained using Figure 4.11 and the following equation for the shear stress [5], where r = (x,y,z):

$$\vec{\tau}(r) = -\mu \frac{\mathrm{d}\vec{\mathrm{v}}(\mathrm{r})}{\mathrm{dr}} \tag{4.14}$$

This formula basically states that the amount of shear stress in a given point is proportional to the derivative of the velocity profile. When the flow enters the channel, the velocity profile is uniformly distributed and the shear stress is very large at the sidewalls. The velocity profile will evolve into a parabolic one where the shear stress gradually becomes smaller until reaching steady-state in a parabolic velocity profile. In the derivation of equation (4.9) viscosity is taken

into account under the assumption that the channel length is much greater than the development length of the flow and the higher effective viscosity in the development phase can be neglected. In order to overcome these higher shear stresses, more pressure will be needed. To calculate the actual pressure needed for a given flow rate in an underdeveloped system, numerical simulations or actual experiments are required.

4.2 Simulations

Using the finite element analysis software *COMSOL* [8], we performed simulations to verify the theoretical value given by the linear relation between pressure and flow rate for a Hagen-Poiseuille flow (equation (4.9)). For both the photonic crystal and the delay spiral of the MZI, one channel was modelled. The properties of the fluid were chosen the same as in the theoretical analysis above: the dynamic viscosity μ was set at 1.002 mPa·s and the density at 1 kg/dm^3. At the inlet of the channel, a uniform velocity profile with magnitude $Q/N \cdot A$ was applied where Q is the flow rate, A the cross-sectional area of one channel and N the number of parallel channels. The software then proceeds to calculate the evolving velocity field $\vec{v}(r)$ of which we can take the derivative at the sidewalls. The pressure Δp needed to sustain a certain flow rate is equal to the counteracting viscous forces (see Figure 4.11) so we can state:

$$\Delta p = -\frac{\oint_A \mu \frac{\mathrm{d}\vec{v}(r)}{\mathrm{d}r} \mathrm{d}A}{A} \tag{4.15}$$

Here, the closed surface integral of the shear force is calculated and divided by the cross-sectional area of the channel.

In Figure 4.12 we see that the flow at the end of the 220-nm-thin channel is far from developed. For the MZI, the resulting pressure needed to support a total (i.e. through all parallel channels combined) flow rate of 11.8 µl/s is 44 kPa, over four times the calculated pressure of 10 kPa. It should be noted that we were not able to chose the element size in an optimal manner due to the large aspect ratio of the structure (50 µm compared to 220 nm) so the obtained value might still change with a finer grid size. For a pressure of 10 kPa, a total flow rate of 2.7 µl/s can be achieved.

For the photonic crystal, for a total flow rate of 0.02 µl/s in 2000 cylindrical channels, a pressure of 20 kPa is required, again higher than the theoretical value. The difference between the simulated and theoretical value is here smaller since the flow development length in the cylindrical channel is shorter, as we can see in Figure 4.13. For a pressure of 10 kPa, a total flow rate of 0.01 µl/s can be achieved. Note that here, the aspect ratio of the simulated structure

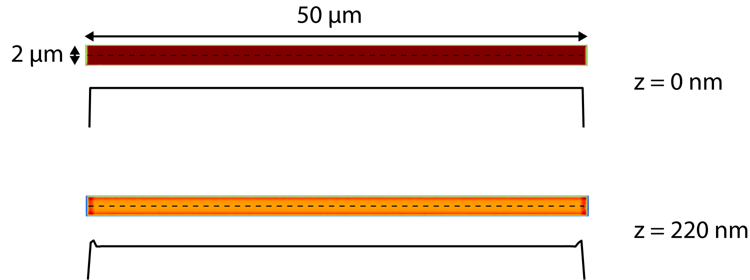

Figure 4.12: Velocity fields at the beginning and the end of a rectangular channel of an MZI hole with cross-sections through the centre. Due to the fact that the laminar flow is not yet fully developed in the short rectangular channel, the actual pressure needed to support a flow will be higher. In this case, we need 44 kPa (compared to a theoretical value of 10 kPa) to support a 11.8 μl/*s* flow.

is more favourable for a better grid definition and the results should be more accurate.

4.3 Experiments

Now that we have a good understanding of the fluidic part of the sensor, we can shift our focus to the optical part and the sensor as a whole. Both photonic crystal based sensors and MZI based sensors have been fabricated using the process described in Chapter 3. However, the light source and detector are not integrated on the chip but are in this experimental phase externally coupled through optical fibres. The setup used to characterise the sensors is described here first, followed by experimental data.

4.3.1 Setup

Coupling light in and out of a photonic integrated circuit is a problem that has been investigated thoroughly in literature [9–12] because it is indeed a very important issue: if one is unable to efficiently couple light into a chip, a perfectly working circuit can be rendered useless. The advantage of silicon photonics, that we can create wavelength-scale waveguides, becomes a disadvantage here: the light, guided in an optical fibre with a core diameter of about 10 μm has to be coupled in a waveguide of 220 nm by 450 nm. If we were to simply place both the fibre and waveguide close to each other, it is intuitively clear that the light coupling will be very inefficient due to a size mismatch of a few orders of

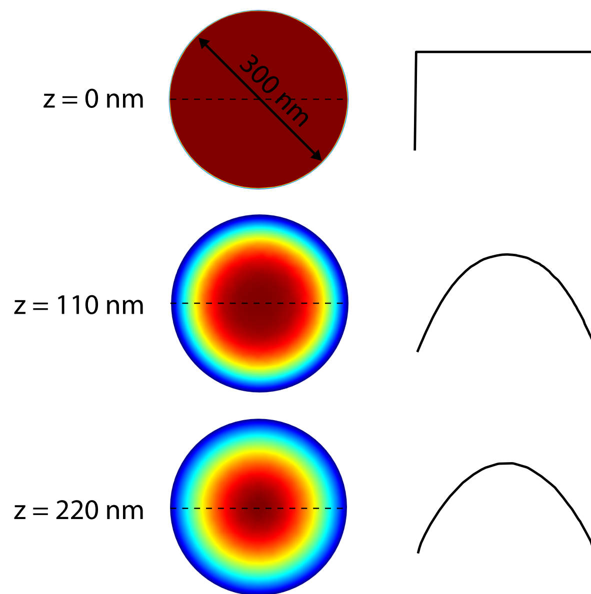

Figure 4.13: Velocity fields at the beginning, middle and end of a cylindrical channel of a photonic crystal hole with cross-sections through the centre. In the cylindrical channel, the flow is developed although 85% of the channel is used for the development phase. Therefore, the pressure will be again higher than the theoretical value: we need 20 kPa (compared to a theoretical value of 10 kPa) to support a 0.02 $\mu l/s$ flow.

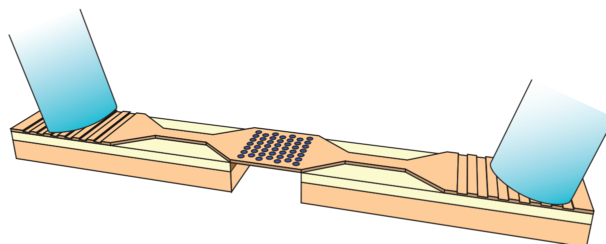

Figure 4.14: Grating couplers can be used to efficiently couple light from an optical fibre to a nanophotonic waveguide. The grating changes the propagation direction of the light from vertical to horizontal (or vice versa). Horizontal mode conversion is done by tapering from a 10-μm-broad to a 450-nm-broad waveguide.

magnitude. This can be solved e.g. by using a lensed fibre that focuses the light onto a smaller spot at the end of the fibre as to decrease the mode mismatch between the optical fibre and the waveguide. Other methods are also possible but in our group, the most commonly used structure is a grating coupler. Basically, this structure, comprising a 1D photonic crystal (i.e. Bragg grating), can couple vertically incident light, for a certain wavelength range, in the horizontal direction. A detailed explanation about the principle behind a grating coupler is given in Chapter 6 where we propose an improved version of this structure but for now, we only take into account its property to change the direction of light. If we make such a grating coupler with the same width as an optical fibre, most of the light can be collected. Once the collected light is changed from the vertical to the horizontal direction, it still has to be converted from a 10-μm-broad to a 450-nm-broad waveguide. This can be done by using an adiabatic taper where there are, in theory, no conversion losses. Since both the grating coupler and taper are reciprocal structures, they can also be used to convert the small light mode to a broad optical fibre mode. This coupling scheme is illustrated in Figure 4.14. Two key advantages of this approach is that it has a large alignment tolerance and that no cleaved facets are required to horizontally couple a fibre. An added benefit is that grating couplers can be placed anywhere on a device (i.e. the centre) so a lot of structures can be interrogated or a wafer can be tested before it has to be cleaved. Katrien De Vos [13] used these grating couplers to demonstrate a multiplexed ring resonator-based biosensor.

Figure 4.15 shows a practical implementation of a measurement setup using grating couplers. Light coming from a SANTEC TSL-510 [14] tunable laser is coupled in through a fibre (left fibre in the figure) in the grating coupler, after its polarisation has been adjusted to match that of the grating coupler mode (by

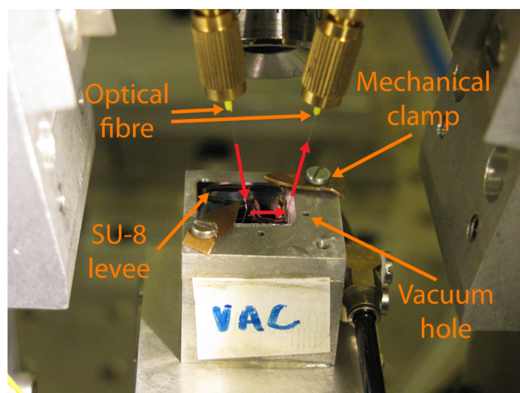

Figure 4.15: Practical implementation of a measurement setup using grating couplers. Fibres are placed at an angle of 10°to the normal of the chip surface. A specially designed chip holder allows for pressure to be applied under the chip (not visible here).

achieving maximum output intensity in a reference waveguide). After travelling through the chip, the light is coupled back out and directed to an HP 8153A optical power meter [15]. Note that the optical fibres are not placed exactly vertical over the grating couplers. As will be explained in more detail in Chapter 6, a vertically positioned fibre will not only couple light in the direction of the sensing structure (right in the figure) but also an equal amount in the other direction where it is not used. By positioning the fibres under an angle, symmetry is broken and for the right period Λ of the Bragg grating, most of the light can be coupled in only one direction.

Since binding of biomolecules can happen in a few minutes, we wish to scan a certain wavelength spectrum in a very short time as to obtain several data points in a binding curve. Furthermore, we wish to show that the proposed fluidics scheme is faster than conventional, diffusion limited schemes. A measurement method where we change the lasing wavelength, wait for a signal of the laser saying that the wavelength has been reached, measure the output, change the wavelength again and so on can be very time consuming since a lot of communication has to take place between the computer and peripheral devices. The tunable laser can however be set in a continuous sweep mode where no explicit control signals are sent to the computer. Instead, the laser sends a pulse train for each wavelength sweep and records in a buffer memory the wavelength values at which a pulse is sent. Using a National Instruments USB-6212 data acquisition (DAQ) module [16] connected to a computer, we can use this pulse train as a trigger signal on the analogue output signal of the optical power meter (which provides a continuous output). This setup is shown in Figure 4.16.

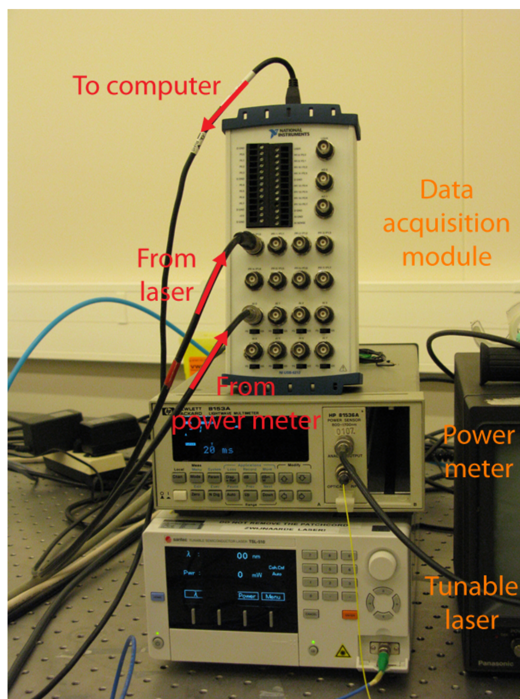

Figure 4.16: Using a data acquisition module, we can perform fast measurements over a certain wavelength spectrum. These fast measurements are needed since binding of biomolecules can happen in a few minutes.

Using this method, we can obtain a high resolution wavelength spectrum with an average time period of 15 s, while it can take up to 5 minutes to obtain the same spectrum using the stepwise method.

4.3.2 Results

To characterise our sensors, we will measure the shift of a spectral feature when a 5 µl droplet containing 1.25 mg/ml bovine serum albumine (BSA) is added to a 5 µl droplet of phosphate buffered saline (PBS) with pH 8. This experiment is straightforward since no receptor molecules need to be applied to our sensor because BSA binds directly to silicon [17]. Before starting the experiment, we want to ensure that our sensor is in fact hydrophilic. The contact angle of blank silicon is 22° [1] but HF treated silicon has a contact angle of 70° [18]. Although this should pose no real problem since the surface is still hydrophilic, we give our sensors a 10-minute oxygen plasma treatment. Not only does this reduce

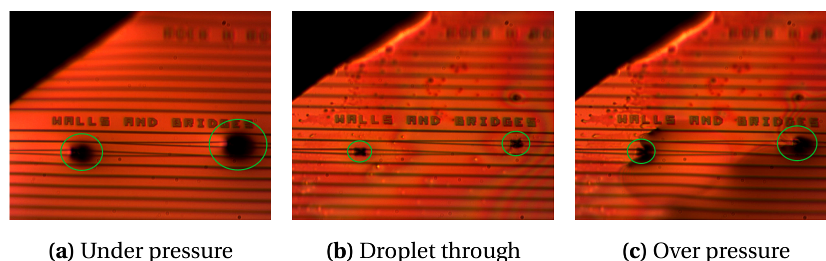

(a) Under pressure **(b)** Droplet through **(c)** Over pressure

Figure 4.17: When applying under pressure, the droplet is pulled through the photonic crystals (marked in green) (a) until it is no longer on the surface (b). By applying over pressure, the droplet can be pushed back through (c).

the contact angle to practically 0° (i.e. full wetting), due to the creation of silanol groups that have a strong affinity to water, but it also acts as an extra cleaning step to remove organic contaminants. Another preparatory step we do after this is making a small reservoir around the actual sensor by creating a closed SU-8 levee. If not for this reservoir, full wetting would make the liquid solution cover the entire chip, including the grating couplers which is an undesired effect.

Before actual measurements, we tested whether we could in fact pull and push the droplet through the membrane with holes. Movie stills of a droplet being pulled and pushed back through can be seen in Figure 4.17. In the first frame, we see two darkened regions (marked in green) where two photonic crystals are located. Since an underpressure of 10 kPa is applied, the liquid is pulled through the photonic crystals and they can be considered as sinks. In the second frame, most of the droplet has been pulled through (save for some locally wet regions on the chip surface). If we now apply overpressure at the substrate side of the chip, we can push the liquid back through the photonic crystals which can now be considered sources (third frame).

The time it takes to pull the 5 μl droplet through is about 30 s for this device. Due to the design of the chip holder, three photonic crystals can be addressed in parallel. If we compare this to the theoretical time of 250 s for one photonic crystal (83 s for three photonic crystals in parallel) we are in the same order of magnitude. The reason why in practice, the droplet goes through faster is that, due to misalignment or undercut (see Chapter 3) during fabrication, the underetched windows are not always exactly aligned with the photonic crystals and can also cover part of the 2-μm-wide waveguide trenches near the photonic crystals (see Figure 4.18). These trenches also act as channels and due to their relatively large size they can accommodate a larger flow rate than the photonic crystals at the same pressure. Since these trench channels have a much lower hydraulic resistance than the photonic crystal holes, most of the fluid will flow

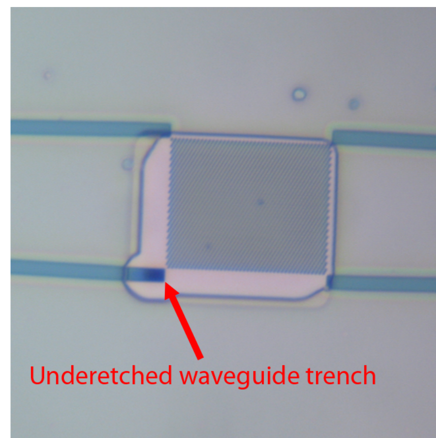

Figure 4.18: An underetched bulk photonic crystal where part of the waveguide trench is also underetched. This will act as a low resistance channel, preventing a significant flow through the photonic crystal holes.

through this channel, which is an undesired effect.

As touched upon in Chapter 2, photonic crystals are very sensitive to variations in the unit cell (e.g. hole diameter, periodicity or refractive index). Since the photonic crystals we fabricated all exhibit non linear buckling behaviour, we expect that the quality of the optical spectrum (e.g. band edge sharpness) will degrade due to the elasto-optic effect which accounts for a change in refractive index due to mechanical stress. This is what we observe in Figure 4.19 which shows the upper band edge of an underetched bulk photonic crystal in air, with period a=580 nm and hole diameter d=0.6a, excited in the ΓM direction. Here, the band edge is no longer sharply defined which makes it difficult to use it as a measure for high resolution sensing. Furthermore, we also cannot fit an analytical model to the measurement data which would normally improve sensor resolution.

We tried measuring a BSA solution using photonic crystals but did not find a suitable structure with a well-defined band edge in an aqueous environment. Other moderately sharp spectral features were present but since no clear theoretical explanation could be found for them, we could not perform data fitting rendering the measurement analysis dubious.

Although Mach-Zehnder interferometers are mechanically more fragile than photonic crystals, they are optically more robust: the entire wavelength spectrum consists of a cosine function so the elasto-optic effect will only induce an absolute shift of these features compared to the design values. Since we are only interested in a relative shift, this poses no problem and we can use MZIs

Figure 4.19: Upper band edge of an underetched bulk photonic crystal with a period a=580 nm and hole diameter d=0.6a, excited in the ΓM direction in air. Due to non linear buckling, the band edge is no longer sharply defined and it is difficult to use it as a measure for high resolution sensing.

for sensing purposes. An example of a measured MZI-based sensor is shown in Figure 4.20 where we see two arms from two different MZIs. On the left, we see the right arm of one MZI and on the right the left arm of another MZI. Since they are closely spaced at one point, we can use one underetched window for both devices. In this particular chip, no delay spiral was used but only one straight waveguide. The underetched waveguide retained some extra mechanical stability because of a silicon dioxide bridge that remained after vapour HF etching, which in this case occurred in a non uniform manner. This allowed us to reuse the sample several times by cleaning it with a (wet) Piranha solution. For normal MZI-based sensors, i.e. without the bridge, wet processing causes stiction and renders them useless.

A measurement is divided into several pump cycles: an underpressure of P_{pump} is applied at the substrate side of the chip for a number of seconds ($T_{pump}/2$). After that, an overpressure of P_{pump} is applied at the substrate side of the chip for the same number of seconds. The pressure is stabilised again (i.e. no pressure gradient) and the wavelength spectrum is measured N_{meas} consecutive times. When this is done, a new pump cycle is started. Note that we do not perform measurements when there is either over or under pressure. This is because the elasto-optic effect created by this pressure gradient would cause an additional shift of the spectral features which has to be decoupled from the biomeasurements. In practice, the change from 0 to P_{pump} is not instantaneous but the pressure difference is created by enlarging or diminishing the volume of a piston (which causes a pressure change, due to the ideal gas law). More information and a schematic of this set-up to apply pressure, can be found in Section 5.3.

In our experiments, first a droplet of PBS is applied on the sensor. A few pump cycles are executed after which a droplet of BSA solution is added to the

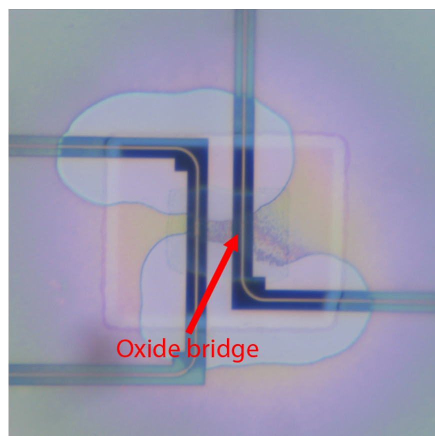

Figure 4.20: The right arm of one MZI and left arm of another MZI are close together so that both devices can be underetched with one window. In this particular chip, the underetched waveguide retained some extra mechanical stability because of a silicon dioxide bridge that remained after vapour HF etching, which in this case occurred in a non uniform manner.

PBS droplet. Again, a number of pump cycles are executed until the measurement is stopped. Table 4.1 shows the parameters used for the measurements of MZI-based biosensors. Figure 4.21 shows the wavelength shift of a spectral dip at 1530 nm in function of time for the same biosensor (which is reused after being cleaned using a Piranha solution): the solid curve shows a measurement where the BSA droplet is introduced right before a new pump cycle starts and the dashed curve shows a measurement where the BSA droplet is applied after pumping but before the wavelength measurements start, i.e. no subsequent pumping is performed to help the BSA reach the sensor.

When studying the individual curves we see that when no BSA has been introduced yet (i.e. only 5 μl of PBS is present) there is already a relatively large negative shift. Since this wavelength shift can not be caused by chemical binding, we treat this as drift. Since silicon has a high thermo-optic coefficient (1.86×10^{-4} K^{-1} [19]), thermal drift can be significant. At several occasions, we can also see sudden increases of the shift. These always occur after a pump cycle and can be caused by e.g. a change in hydrostatic pressure: since the analyte volume is finite, it is not always guaranteed that after a pump cycle, we end up in the same situation as before. It is possible that small changes in the pressure equilibrium have an effect on the mechanically sensitive waveguides of 220 nm thickness.

When examining the binding event (i.e. transition from PBS to PBS+BSA),

Parameter	Value
P_{pump}	10 kPa
T_{pump}	20 s
N_{meas}	10
PBS pump cycles	5
BSA pump cycles	5
PBS pH	8
PBS volume	5 µl
BSA volume	5 µl
BSA concentration	1.25 mg/ml

Table 4.1: Parameters used for the measurements of MZI-based biosensors.

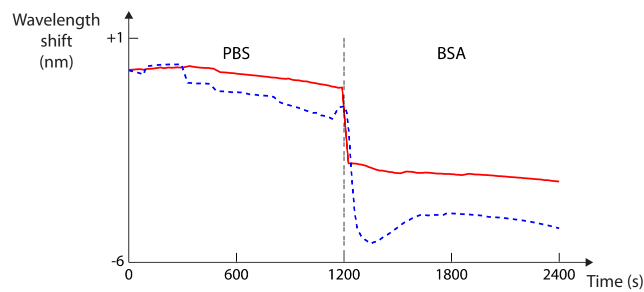

Figure 4.21: Both curves show the shift of a spectral feature in function of time. At t=1200 s, the BSA droplet is added to the PBS droplet and the wavelength of the spectral dip begins to shift. The red, solid curve shows the shift over time when the fluid is pumped immediately after adding the BSA droplet. The blue, dashed curve shows the shift over time when no initial pumping is performed after adding BSA.

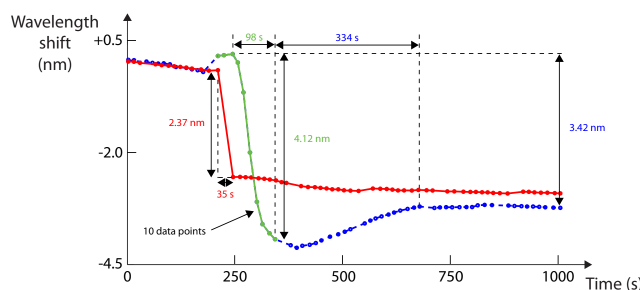

Figure 4.22: Zoom on the binding of BSA. Pumping the BSA through immediately after application (red, solid curve) improves the binding time compared to the case of no pumping (blue, dashed curve). The green section of the dashed curve indicates one sequence of 10 measurements after a pump cycle.

we notice a clear difference in the binding curves of both measurements. In the case where the BSA is applied after the pumping and before the 10 measurements, we see a typical binding curve that starts off steeply and gradually reaches its peak value. In the other case, where the BSA is introduced and we immediately pump, we do not see this binding curve and immediately go into saturation. Although we were unable to irrefutably prove it, what we see then is, most likely, immediate saturation due to binding. This is what we set out to demonstrate: by creating a flow path through the sensor (latter case), binding of the biomolecules would occur quicker than if we would have to wait for diffusion (former case). When quantitatively comparing both configurations, we see that the time it takes for binding with pumping is about 35 s (which is here limited by the pump duration and can be reduced upon optimisation) while the time it takes for the binding curve to reach its maximum is 98 s, almost a factor of 3. However, when examining the first case further, we see that there appears to be an overshoot between t=250 s and t=750 s in the binding curve (another overshoot before t=250 s is caused by pumping effects). This phenomenon has also been observed by Glazer [20] in the binding behaviour of oligonucleotides to corresponding receptor molecules where they explain that in some cases, two molecules bind to one probe, creating a metastable state. Eventually one of the molecules will desorb explaining the relaxation of the overshoot peak. Although we do not work with probes here but rely on direct binding of BSA to silicon, it is possible that the overshoot behaviour in our case can be attributed to a similar effect although a further, thorough analysis of the chemical reactions is required to be certain of this. It is interesting to note that in the case of pumping, this metastable state does not occur. If we consider that the time until saturation

also includes the time it takes for the overshoot to relax, we can state that the total binding time is 432 s in the case without pumping. Using pumping, the binding time will be more than a factor of 10 shorter. The difference in amount of shift between the two measurements is probably caused by the above mentioned temperature and pressure effects. There is no apparent reason to state that using the pump delivers less biomolecules to the sensor surface as in both measurements, the sensor is eventually saturated.

We have seen in Chapter 2 that the sensitivity of an MZI is determined by the following formula:

$$S = \frac{\mathrm{d}\lambda}{\mathrm{d}n_{bio}} = -\frac{\lambda \frac{\partial n_{eff,bio}}{\partial n_{bio}} L_{1,bio}}{n_{g,clad}(L_{2,clad} - L_{1,clad}) - n_{g,bio} L_{1,bio}} \tag{4.16}$$

Using this formula, we can theoretically determine the sensitivity of the sensor to temperature changes, bulk refractive index change and thin layer adsorption. From Scanning Electron Microscope (SEM) pictures, we can measure the exposed part of the MZI and find $L_{1,bio}$ = 56 µm. The other relevant length in that formula is $L_{2,clad} - L_{1,clad}$ = 98 µm. Using *COMSOL*, we can calculate the group index in the cladding and exposed parts of the MZI and find $n_{g,clad}$ = 4.138 and $n_{g,bio}$ = 4.227 respectively. To illustrate: for a temperature change in the exposed part of the MZI $L_{1,bio}$, we can easily determine the temperature dependence by replacing $\frac{\partial n_{eff,bio}}{\partial n_{bio}}$ and $\mathrm{d}n_{bio}$ with $\frac{\partial n_{eff,bio}}{\partial T}$ and $\mathrm{d}T$ respectively, where T is the temperature. This derivative can again be simulated using *COMSOL* and is 0.2067e-3 K^{-1} where we used the value of the thermo-optic coefficient that was stated in the above. The resulting temperature sensitivity is then -106 pm/K, showing that temperature effects can have a significant influence. Future versions of the chip holder should therefore include a temperature feedback loop so these effects can be minimised. The wavelength shift induced by a bulk refractive index change can be deduced in a similar fashion and is found to be -139 nm per refractive index unit (RIU). The refractive index of PBS is 1.3348 [21]. Adding BSA will increase the refractive index by an amount 0.00187C where C is the BSA concentration in percent [22, 23]. By adding 5 µl of 1.25 mg/ml BSA in PBS to a 5 µl pure PBS droplet, the total BSA concentration becomes 0.625 mg/ml, giving a concentration of 0.0625%. The refractive index will then shift by an amount of 1.17×10^{-4} RIU. The shift of the spectral features will then be 16 pm, which is virtually undetectable in our setup as this shift would be indistinguishable from a temperature variation of 0.1 K.

However, in experiments where a layer of biomolecules adsorbs to the sensor surface, the dominating wavelength shift is induced by a thin layer of biomolecules around the sensing arm [24]. When we model this layer as being uniformly coated around the waveguide with an average refractive index $\overline{n}$ and thickness $\overline{t}$, we can determine the adsorbed layer sensitivity (for a given $\overline{n}$) in

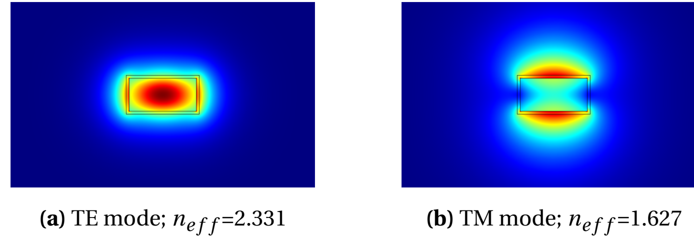

(a) TE mode; n_{eff}=2.331 **(b)** TM mode; n_{eff}=1.627

Figure 4.23: Magnitude of the electric field for Transverse Electric (TE) and Transverse Magnetic (TM) mode of a 220 nm by 450 nm silicon waveguide with an adsorption layer of 20 nm thickness $\overline{t}$ with average refractive index $\overline{n}$ = 1.45. The TM mode extends more into the surrounding medium (hence the lower effective index) and is therefore more sensitive to refractive index changes in that region.

nm/nm. Some authors [24, 25] assume for all proteins an average refractive index of 1.45 and determine an effective thickness, depending on the protein and other factors (e.g. pH-value and surface chemistry). For the specific case of BSA, Watanabe [26] determined that for 1 mg/ml BSA at pH 7 adsorbed on a cationic monolayer, the layer thickness was 8 nm with an average refractive index of 1.40. Freeman [27] states different values (using a slightly different set of parameters) but claims that the BSA layer thickness can vary between 4 and 14 nm in certain cases, depending on the orientation of the absorbed molecules. In our experiments, we were unable to quantify the average refractive index of the adsorbed layer nor its thickness since we did not have the appropriate tools at our disposal during the measurements so the following calculations are merely indicative estimates. Furthermore, the exact value of the wavelength shift is of less importance than the speed at which binding occurs.

With *COMSOL*, we can calculate that for an average refractive index of $\overline{n}$ = 1.40, the sensitivity is -0.129 nm/nm while for an average refractive index of $\overline{n}$ = 1.45 this is -0.228 nm/nm. Note that, apart from the strong dependence of this sensitivity on the average refractive index $\overline{n}$, both values are for the Transverse Electric (TE) mode of the waveguide. The Transverse Magnetic (TM) mode extends more into the surrounding medium (see Figure 4.23b), which explains the lower effective index, and is therefore more sensitive: for the case of $\overline{n}$ = 1.45, the sensitivity of the TM mode is -0.527 nm/nm compared to -0.228 nm/nm of the TE mode. The reason why we used TE-polarised light in our experiments is that in our group, most photonic structures are optimised for this polarisation.

Using the data from Watanabe [26] and our calculated layer sensitivity, we expect a wavelength shift of 1.03 nm. Comparing this to the experimental values of 2.37 nm and 3.42 nm we see more than a factor of 2 and 3 difference respec-

tively. As mentioned above, the exact behaviour of proteins depends on a variety of factors and the discrepancy between our experimental results and the calculated results probably is caused by the fact that the surface chemistry between the cationic layer in Watanabe's work is different from the fully wetted silicon we use. Furthermore, although BSA normally forms monolayers [28], some authors have reported multilayer BSA behaviour on mica [29, 30]. The difference in shift between the two situations (pumping or no pumping) might be attributed to BSA solution degradation over time, temperature drift or improper cleaning of the sensor between two measurements. Finally, since we were unable to perform post-measurement analysis on the characterised sensors, caution should be exercised when interpreting the results since it might be possible that we are observing a mixing effect instead of actual binding. We can conclude that we need more information on the actual adsorbed layer properties and more experimental data before we can quantitatively compare theoretical and experimental results and to inconclusively prove that binding behaviour is in fact observed. However, we were able to show that transporting a droplet of analyte through a biosensor membrane is in fact possible and that it is likely that the binding time can be improved by a factor of 3.

4.4 Conclusions

Using microfluidics theory we have calculated the pressure that is required to create a flow through a membrane with openings that acts as a biosensor. These theoretical insights and calculations were further improved using numerical simulations that showed us that due to the approximations used in the Hagen-Poiseuille theory, the actual required pressure is larger although in the same order of magnitude. We have characterised a Mach-Zehnder interferometer-based biosensor and were able to show that it would be possible to achieve faster binding (in this case at least 3 times faster) of proteins to the biosensor using a flow through the biosensor. Further experiments should verify that this is indeed caused by binding behaviour. We were unable to prove the secondary goal of increased sensitivity for low concentration detection since no robust surface chemistry was available at the time for our sensors. Since the above experiment is a proof of concept, there is still room for improvement on several levels, e.g.: mechanically more stable structures, temperature controlled measurements and using TM-polarised light.

References

[1] H. Bruus. *Theoretical Microfluidics*. Oxford University Press, 2008.

[2] A. B. D. Cassie and S. Baxter. *Wettability of porous surfaces.* Transactions of the Faraday Society, 40:546–551, 1944.

[3] G. Karniadakis, A. Beskok, and N. Aluru. *Microflows and Nanoflows.* Springer, 2005.

[4] D. Bernoulli. *Hydrodynamica.* Argentorati: sumptibus J. R. Dulseckeri, 1738.

[5] Y. Cengel, R. Turner, and J. Cimbala. *Fundamentals of Thermal-Fluid Sciences.* McGraw-Hill Science/Engineering/Math, 4th edition, 2011.

[6] J. Kestin, M. Sokolov, and W. A. Wakeham. *Viscosity of Liquid Water in the Range -8 °C to 150 °C.* Journal of Physical and Chemical Reference Data, 7(3):941–948, 1978.

[7] F. Durst, S. Ray, B. UÌĹnsal, and O. A. Bayoumi. *The Development Lengths of Laminar Pipe and Channel Flows.* Journal of Fluids Engineering, 127(6):1154, 2005.

[8] COMSOL, *http://www.comsol.com/.*

[9] F. M. Soares, F. Karouta, E. J. Geluk, J. H. C. van Zantvoort, H. De Waardt, R. Baets, and M. K. Smit. *Extremely low-loss vertically-tapered spot size converter in InP-based waveguide structure.* In Proceedings Symposium IEEE/LEOS Benelux Chapter, pages 127–130, Ghent, 2004.

[10] D. Taillaert. *Grating couplers as Interface between Optical Fibres and Nanophotonic Waveguides.* PhD thesis, Ghent University, 2004.

[11] J. V. Galan, P. Sanchis, J. Martí, S. Marx, H. Schroeder, B. Mukhopadhyay, T. Tekin, S. Selvaraja, W. Bogaerts, P. Dumon, and L. Zimmermann. *CMOS compatible silicon etched V-grooves integrated with a SOI fiber coupling technique for enhancing fiber-to-chip alignment.* In 6th IEEE International Conference on Group IV Photonics, pages 148–150, San Francisco, 2009.

[12] D. Vermeulen, S. Selvaraja, P. Verheyen, G. Lepage, W. Bogaerts, P. Absil, D. Van Thourhout, and G. Roelkens. *High-efficiency fiber-to-chip grating couplers realized using an advanced CMOS-compatible Silicon-On-Insulator platform.* Optics Express, 18(17):18278–18283, 2010.

[13] K. De Vos, J. Girones, T. Claes, Y. De Koninck, S. Popelka, E. Schacht, R. Baets, and P. Bienstman. *Multiplexed Anitbody Detection With an Array of Silicon-on-Insulator Microring Resonators.* IEEE Photonics Journal, 1(4):225–235, 2009.

[14] Santec, *http://www.santec.com/*.

[15] HP, *http://www.agilent.com/*.

[16] National Instruments, *http://www.ni.com/*.

[17] R. Desai and R. J. Richards. *The adsorption of biological macromolecules by mineral dusts*. Environmental Research, 16:449–64, July 1978.

[18] S. Franssila. *Introduction to Microfabrication*. Wiley, 2010.

[19] B. Guha, B. B. C. Kyotoku, and M. Lipson. *CMOS-compatible athermal silicon microring resonators*. Optics Express, 18(4):3487–93, February 2010.

[20] M. Glazer, J. a. Fidanza, G. H. McGall, M. O. Trulson, J. E. Forman, A. Suseno, and C. W. Frank. *Kinetics of oligonucleotide hybridization to photolithographically patterned DNA arrays*. Analytical Biochemistry, 358(2):225–38, November 2006.

[21] S. Pace, B. Seantier, E. Belamie, N. Lautrédou, M. J. Sailor, P.-E. Milhiet, and F. Cunin. *Characterization of phospholipid bilayer formation on a thin film of porous SiO2 by reflective interferometric Fourier transform spectroscopy (RIFTS)*. Langmuir : the ACS journal of surfaces and colloids, 28(17):6960–9, May 2012.

[22] R. Wayne. *Light and Video Microscopy*. Elsevier, 2009.

[23] S. Carrara. *Nano-Bio-Sensing*. Springer, 2011.

[24] K. De Vos. *Label-free Silicon Photonics Biosensor Platform with Microring Resonators*. PhD thesis, Ghent University, Ghent, 2010.

[25] E. Özkumur, M. Cretich, C. A. Lopez, D. A. Bergstein, B. B. Goldberg, M. Chiari, and M. S. Ünlü. *Quantification of DNA and protein adsorption by optical phase shift*. Biosensors & Bioelectronics, 25:167–72, September 2009.

[26] N. Watanabe, T. Shirakawa, M. Iwahashi, K. Ohbu, and T. Seimiya. *Effect of surface charge on adsorption of bovine serum albumin as studied by ellipsometry*. Colloid and Polymer Science, 264:903–908, 1986.

[27] N. J. Freeman, L. L. Peel, M. J. Swann, G. H. Cross, A. Reeves, S. Brand, and J. R. Lu. *Real time, high resolution studies of protein adsorption and structure at the solid-liquid interface using dual polarization interferometry*. Journal of Physics: Condensed Matter, 16:S2493–S2496, 2004.

[28] V. B. C. Figueira and J. P. Jones. *Viscoelastic study of the adsorption of bovine serum albumin on gold and its dependence on pH.* Journal of Colloid and Interface Science, 325:107–13, September 2008.

[29] J.-P. Gallinet and B. Gauthier-Manuel. *Adsorption-desorption of serum albumin on bare mica surfaces.* Colloids and Surfaces B: Biointerfaces, 68:189–193, 1992.

[30] H. Terashima and T. Tsuji. *Adsorption of bovine serum albumin onto mica surfaces studied by a direct weighing technique.* Colloids and Surfaces B: Biointerfaces, 27:115–122, 2002.

"Life can be a challenge
Life can seem impossible
It's never easy
When there is so much on the line"

Donna Summer, Musician, 1948-2012

5

Differential pressure sensor

Checking the quality of a vacuum, controlling tire pressure or determining the altitude in an aeroplane: these are all applications for a pressure sensor. For decades, research into electrical pressure sensors has been ongoing with plenty of scientific output [1–3]. Although most sensors focus on an electrical implementation, there is also a possibility to develop the sensor in the optical domain where the key advantages are that optical devices are immune to electromagnetic interference and can be deployed in explosive or spark-sensitive environments. Indeed, a lot of work has been published about these optical pressure sensors as well [4–20].

Optical pressure sensors can be subdivided into two main categories: integrated and non-integrated sensors. Non-integrated sensors consist of several discrete components that in some cases require precise alignment, which can increase the packaging cost drastically. Well-known examples of non-integrated pressure sensors are Fabry-Perot based sensors [4–7]. Integrated sensors can be subdivided into two categories: sensors where the transducer is integrated but source and detector are external (e.g. Fibre Bragg Grating (FBG) based sensors [8–12, 17]) and sensors where source, transducer and detector are fully integrated. Fully integrated optical pressure sensors have already been demonstrated in a variety of material platforms [13–16, 19] but here we demonstrate such a sensor in a silicon-on-insulator platform, the main advantage of which is mass fabrication of devices at a low cost.

In this chapter, we will investigate whether we can use the fabrication process described in Section 3.2, to create thin membranes that are sensitive to a pressure gradient. After a theoretical explanation of how a pressure change is translated into an optical signal, we will characterise some devices that we have fabricated, backed by numerical simulations. The optical structures have been designed by Tom Claes during his PhD work [21]. Finally, we will compare our results to other optical pressure sensors reported in literature.

5.1 Theory

When pressure is exerted on an object, stress and strain will be introduced in said object. The profile of stress and strain in function of spatial coordinates depends on both the geometry of the structure and a set of boundary conditions (e.g. free, hinged or fixed points). From the fabrication process described in Chapter 3 it is clear that we will be dealing with rectangular, thin (compared to the substrate thickness) membranes with four fixed edges (see Figure 5.1). If we are able to determine the amount of deflection $w(x, y)$ in the z-direction, it is possible to derive the resulting stresses, strains and bending moments. The deflection $w(x, y)$ of an isotropic plate can be calculated from the following equilibrium condition, provided that the deflection is small compared to the plate thickness:

$$\frac{\partial^4 w}{\partial x^4} + 2\frac{\partial^4 w}{\partial x^2 \partial y^2} + \frac{\partial^4 w}{\partial y^4} = \frac{q}{D} \tag{5.1}$$

where q is the load distribution and D is the flexural rigidity defined as $\frac{Eh^3}{12(1-\nu^2)}$. Here E is Young's modulus of elasticity, ν is Poisson's ratio and h is the plate thickness. Although the above equation can be solved analytically for a circular plate due to axial symmetry, it is not possible to solve it for a rectangular plate. However, under certain conditions (e.g. the deflection must be small compared to the plate thickness and the plate thickness should be small compared to the width and length), approximate solutions exist in literature [22, 23]. For completeness, we add that for large deformations, equation (5.1) is no longer valid and the non-linear Föppl-von Kármán equations [24] have to be solved:

$$\begin{aligned} \frac{Eh^3}{12(1-\nu^2)}\Delta^2 w - h\frac{\partial}{\partial x_\beta}\left(\sigma_{\alpha\beta}\frac{\partial w}{\partial x_\alpha}\right) &= P \\ \frac{\partial \sigma_{\alpha\beta}}{\partial x_\beta} &= 0 \end{aligned} \tag{5.2}$$

where $\sigma_{\alpha\beta}$ is the stress tensor with $\alpha = 1..3$ and $\beta = 1..3$ (corresponding to x, y, and z) and P the applied pressure.

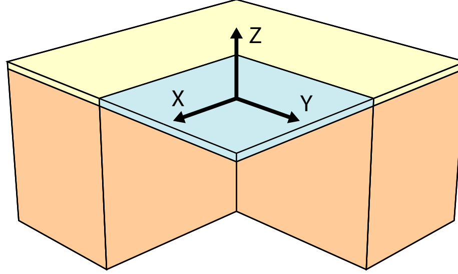

Figure 5.1: The mechanical structure we will be investigating in this chapter is a rectangular, thin membrane with four fixed edges (for clarity, two edges are not shown).

Since strain changes the local density of a material, we can intuitively expect that the refractive index will also change locally. Indeed, due to the elasto-optic effect [25], the refractive index will change according to:

$$\Delta(\frac{1}{n^2})_i = \sum_{k=1}^{6} \pi_{ik}\sigma_k \tag{5.3}$$

Here $(1/n^2)_i$ are the components of the indicatrix or refractive index ellipsoid, π_{ik} the piezo-optical coefficients and σ_k the stress components with $i = 1..6$ and $k = 1..6$ where $1 \equiv xx$, $2 \equiv yy$, $3 \equiv zz$, $4 \equiv yz$, $5 \equiv xz$ and $6 \equiv xy$. If we now place a waveguide on the membrane (e.g. part of a ring resonator), the refractive index change will give rise to a phase shift $\Delta\phi$ in the waveguide:

$$\Delta\phi = \frac{2\pi}{\lambda} \int_{waveguide} n_{eff}(l)\mathrm{d}l \tag{5.4}$$

with λ is the wavelength of the incident light and $n_{eff}(l)$ the local effective index along the waveguide located on the membrane. Similar to biosensing, we can translate this phase shift into a shift of the spectrum of e.g. a ring resonator or Mach-Zehnder interferometer.

Since the above equations are either impossible to solve analytically or have approximate solutions under conditions of which we do not know whether they are fulfilled, we will only make use of numerical simulations in the following.

5.2 Simulations

In the theoretical explanation given above, we can distinguish three parts in the process of changing the total phase shift in a waveguide due to pressure:

- **Stress and strain profiles**
  After the membrane is modelled and the appropriate boundary conditions are set, the stress and strain profiles can be calculated under the influence of a certain pressure P.

- **Refractive index change**
  Due to the elasto-optic effect, the refractive index will no longer be uniform throughout the membrane.

- **Effective index change**
  Based on the now spatially dependent refractive index, the effective index of the waveguide mode can be calculated. Note that this effective index can vary along the waveguide and that an integral along the propagation direction needs to be calculated in order to obtain the total phase shift.

Using *COMSOL* [26], it is possible to link these three parts into one simulation. The mechanical and electromagnetic solver calculate the stress profile and effective index respectively, while the refractive index change is modelled according to equation (5.3), which we can transform into the following formula (in tensor notation):

$$\Delta n_{ij} = -C_{ijkl}\sigma_{kl} \tag{5.5}$$

where Δn_{ij} is the refractive index tensor, C_{ijkl} is the stress-optical tensor and σ_{kl} is the stress tensor. Due to symmetry arguments in an optically isotropic medium, only two independent components of the stress-optical tensor remain, giving:

$$\begin{aligned} n_x &= n_0 - C_1\sigma_{xx} - C_2\left(\sigma_{yy} + \sigma_{zz}\right) \\ n_y &= n_0 - C_1\sigma_{yy} - C_2\left(\sigma_{xx} + \sigma_{zz}\right) \\ n_z &= n_0 - C_1\sigma_{zz} - C_2\left(\sigma_{xx} + \sigma_{yy}\right) \end{aligned} \tag{5.6}$$

where n_0 is the isotropic refractive index in the case without stress in the membrane, σ_{ii} is the stress in the three principal directions and C_1 and C_2 the two independent stress-optical constants. The values used in our simulations are shown in Table 5.1, alongside other mechanical constants.

One of the structures we would like to simulate is shown in Figure 5.2: part of a ring resonator residing on a thin membrane is used as a pressure-sensitive component. In theory, for this type of problem we should make use of 3D simulations. Due to the large difference in dimensions between the membrane (measuring 60 μm by 70 μm) and the optical waveguide (450 nm by 220 nm), along with the fact that the ratio of the membrane thickness to its width and length is quite low (3 μm compared to 60 μm), these simulations would require a large amount of both memory and time. Since simulations here are a means and not

Constant	Value
E_{Si}	169 GPa [27]
ν_{Si}	0.28 [27]
ρ_{Si}	2.330 kg/dm^3 [28]
E_{SiO_2}	75 GPa [29]
ν_{SiO_2}	0.17 [30]
ρ_{SiO_2}	2.200 kg/dm^3 [31]
$n_{0,Si}$	3.476 [32]
$C_{1,Si}$	-17.13$\times$10^{-12} Pa^{-1} [32]
$C_{2,Si}$	5.51$\times$10^{-12} Pa^{-1} [32]
n_{0,SiO_2}	1.444 [32]
C_{1,SiO_2}	1.17$\times$10^{-12} Pa^{-1} [32]
C_{2,SiO_2}	3.73$\times$10^{-12} Pa^{-1} [32]

Table 5.1: Constants used in COMSOL simulations.

an end, we can make use of some simplifications: instead of calculating the total phase change in function of pressure, we will simulate a 2D cross-section of a waveguide on a membrane (see Figure 5.3) and assume that no strain effects occur in the propagation direction of the light (i.e. plane strain approximation; $\epsilon_y = 0$ [33]). By multiplying the calculated effective index, in function of applied pressure, by the path length we obtain the total optical path length instead of having to integrate a varying effective index over the propagation path. Furthermore, we neglect the fact that silicon is a mechanically anisotropic material [27, 34] and treat it as an isotropic material with values listed in Table 5.1. However, we do take into account non-linear mechanical effects because of the small thickness of the membrane.

Figure 5.4 shows the effective index of the Transverse Electric-like (TE-like) mode of a single waveguide in function of the pressure difference over the membrane for different positions on the membrane (the offset value is determined from the centre of the membrane). A negative pressure difference indicates that the pressure below the membrane is lower than above (i.e. atmospheric pressure). In none of the cases we see a linear dependence of the effective index on the applied pressure, proving that non-linear mechanical effects can indeed not be neglected. Although the response for 0 μm offset appears linear at first sight, a closer look reveals that it is in fact slightly non-linear. Furthermore, we see that, depending on the position of the waveguide, the effective index shift is either positive or negative, something that has also been reported by Ohkawa [14]. To explain this, we look at Figure 5.5, where we see that the strain in the x-direction changes sign when comparing the cases of a waveguide with 0 μm offset (i.e. in the middle of the membrane) and 40 μm offset. Note that the

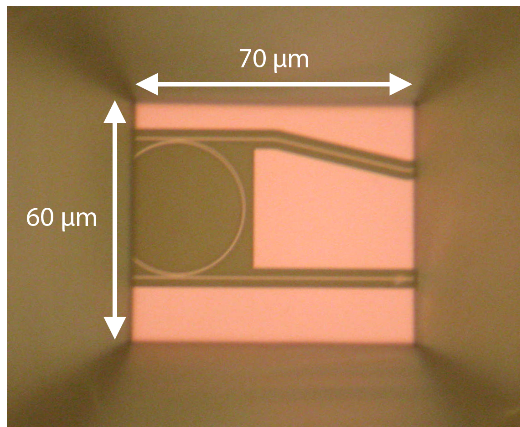

Figure 5.2: Microscopic image of part of a silicon ring resonator where the silicon substrate is locally etched away (seen from the substrate side).

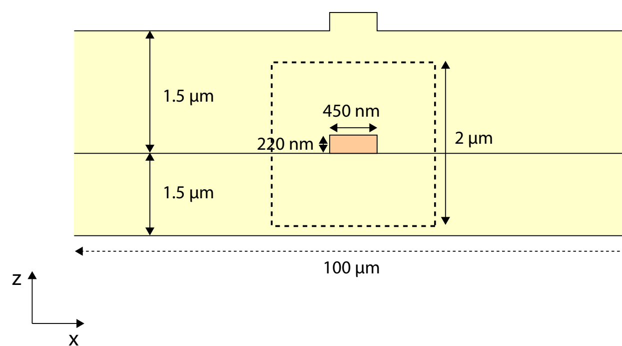

Figure 5.3: Instead of computing the entire 3D structure, we limit ourselves to a 2D cross-section of a waveguide on a thin membrane.

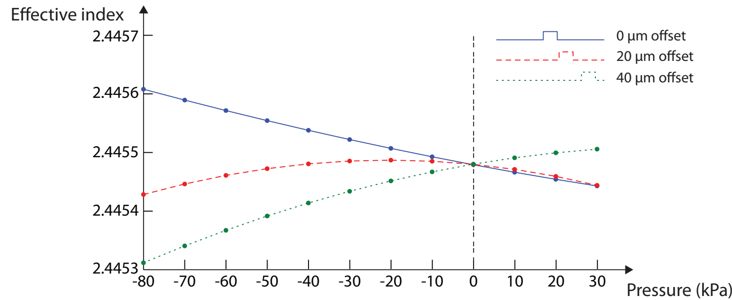

Figure 5.4: The effective index in function of the applied pressure difference also depends strongly on the position on the waveguide. Non-linear mechanical effects play an important role in the sensor response.

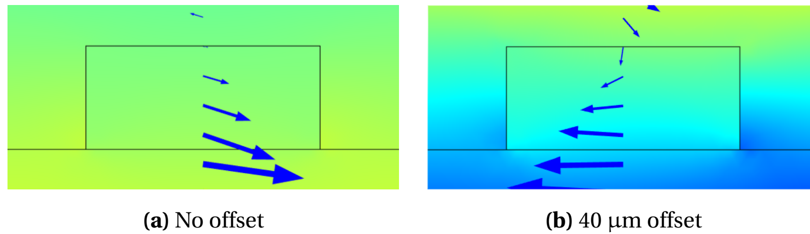

(a) No offset **(b)** 40 μm offset

Figure 5.5: The strain vectors, defined as (ϵ_x, ϵ_z), for a waveguide located in the centre of the membrane (i.e. no offset) and a waveguide located near the membrane edge point towards opposite horizontal directions. The applied pressure difference is -80 kPa and the membrane is 100 μm wide.

arrows in Figure 5.5 do not represent the direction of material expansion but indicate whether the material expands (arrow to the right; positive strain) or compresses (arrow to the left; negative strain). Since the TE-like mode is most sensitive for changes in the x-direction, we see the change in sign translated in the response of the effective index to the applied pressure for both situations. Figure 5.6 further illustrates this by showing the horizontal strain ϵ_x for the entire membrane. The absolute value of the effective index shift for the case of a central waveguide and a waveguide near the membrane edge is in the same order of magnitude with a slightly higher value for the waveguide near the edge (1.7×10^{-4} refractive index units (RIU) compared to 1.3×10^{-4} RIU going from 0 to -80 kPa). These simulations imply that for e.g. a delay spiral arm of a Mach-Zehnder interferometer, where in a cross-section several waveguides are positioned next to each other, the individual responses of the effective index to the pressure difference can add up or partly cancel out.

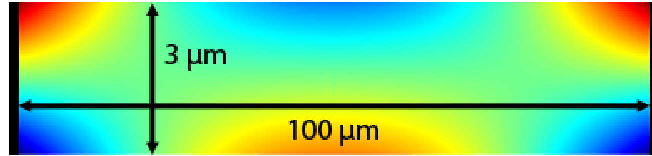

Figure 5.6: The strain ϵ_x in the horizontal direction is, at the top of the membrane, positive (red) near the membrane edges and negative (blue) in the centre. The applied pressure difference is -80 kPa.

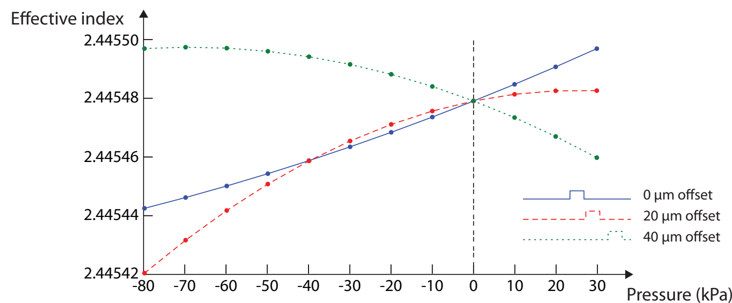

Figure 5.7: The effective index in function of the applied pressure difference depends strongly on the position on the waveguide with a buried oxide layer thickness of 1.5µm instead of 1.0µm. Apart from a smaller effective index shift, we see that the shapes of the curves have altered drastically.

If we were to increase the thickness of the buried oxide (BOX) layer, we would intuitively expect a smaller effective index shift. Figure 5.7 confirms this (the maximum shift has decreased to 5.9×10^{-5} RIU) but we also see that the responses of the effective index to the pressure difference have altered drastically. The reason for this can again be found in the sign of the strain in the horizontal direction. Figure 5.8 shows the sign of the horizontal strain ϵ_x in and around a waveguide located at an offset of 40 µm from the membrane centre. For an increase of 500 nm of the buried oxide layer thickness, the sign changes; the same effect is observed for a waveguide in the centre of the membrane (i.e. no offset). This explains why for 0 µm and 40 µm offset, the rising response of effective index to applied pressure difference has changed into a falling response and vice versa. Note that for a waveguide located near the top of the membrane, changes in the BOX layer thickness will not have such a pronounced effect.

As we have seen in Chapter 3, in reality there is some stress due to lattice mismatch of silicon and silicon dioxide. Figure 5.9 shows that pre-stress has indeed an effect on the effective index shift in function of the pressure difference

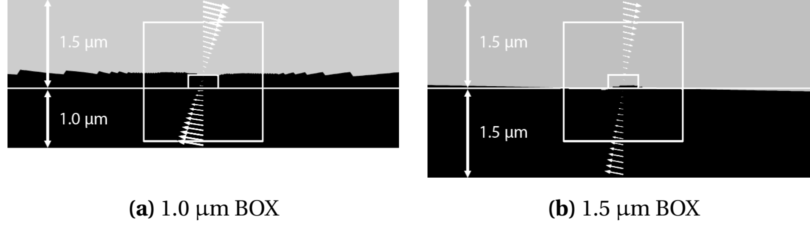

(a) 1.0 µm BOX **(b)** 1.5 µm BOX

Figure 5.8: The sign of the horizontal strain ϵ_x in the waveguide region is opposite for a buried oxide layer thickness of 1.0 µm and 1.5 µm (black indicates a negative sign; grey a positive sign). The applied pressure difference is -80 kPa and the waveguide is located at an offset of 40 µm from the membrane centre.

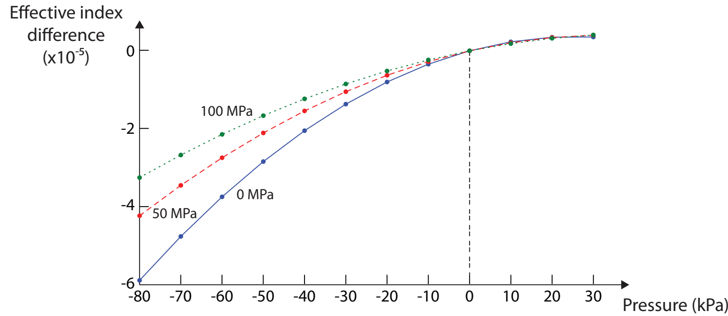

Figure 5.9: When pre-stress is present in the membrane, the shape of the response curve remains similar but the absolute value of the effective index shift decreases with increasing pre-stress.

over the membrane. When the pre-stress increases from 0 to 50 and finally to 100 MPa (typical values for pre-stress in silicon-on-insulator [35]), we see that the effective index shift decreases. When comparing measurement results to simulations, the actual pre-stress in the sensor should be determined as to make a good comparison.

From the above, it is clear that it is not straightforward to perform a good quantitative analysis of a pressure sensor based on numerical calculations. Already under simplified conditions (e.g., 2D cross-section, plain strain approximation), we see that small changes in geometry can have a large impact on the response of the pressure sensor. Therefore, when quantitative simulation results are required, it is advised to compute the entire structure in 3D, bearing in mind the mechanically anisotropic nature of some materials (e.g. silicon) and a good knowledge of all relevant parameters (e.g. pre-stress values, exact layer stack thickness and waveguide positions) is required.

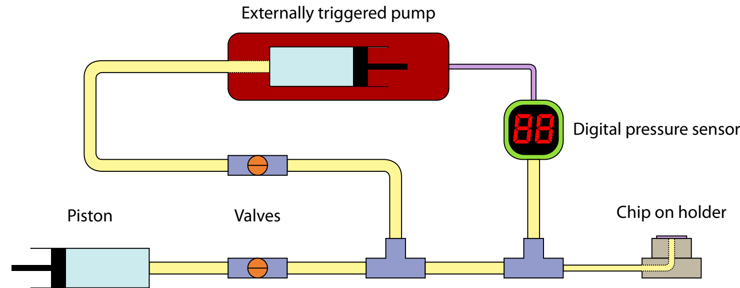

Figure 5.10: The initial pressure difference is achieved by means of a piston. Due to imperfections in the setup or chuck, the pressure difference will decrease over time. By adding a feedback loop between the pump and the digital pressure sensor, the desired pressure level can be maintained.

5.3 Measurements

For characterisation of the devices in the wavelength spectrum, we have used the same set-up as described in Section 4.3.1. Measurements of first generation pressure sensors were done by fixing the chip to the holder using vacuum. However, when trying to create a positive pressure difference (i.e. the pressure under the membrane is higher than atmospheric pressure), the attractive force of the vacuum would be counteracted until the chip would slightly lift from the holder after which there was no longer a sealed pressure volume. In subsequent measurements, we fixed the chip by use of mechanical clamps which were able to withstand higher positive pressure differences.

In order to characterise the pressure sensors, we must obtain a good knowledge of the actual pressure difference that is applied. Using a SUNX DP-101 digital pressure sensor [36], we were able to monitor the applied pressure difference with an accuracy of 1 kPa. In practice, the pressure difference is applied roughly by a piston after which it can be fine-tuned using a syringe in a NE 1000 syringe pump [37]. Due to imperfections in the chip substrate and the pressure circuit, small leaks can occur which will cause the pressure difference to drop over time. To compensate for this, we can use the built-in comparator of the DP-101: when the pressure difference drops below a certain set value, a digital output signal of the sensor changes value. Since the NE 1000 has the capability of being externally triggered, we can use the digital output signal of the pressure sensor as a trigger for the pump. The resulting feedback loop ensures that the pressure level remains fixed over time with an accuracy of about 1 kPa. The entire pressure set-up is illustrated in Figure 5.10.

The first structure we will highlight is a ring resonator as already shown in

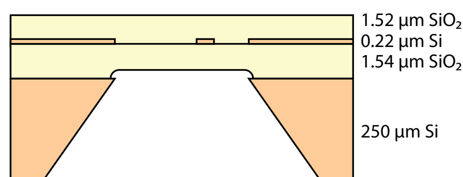

Figure 5.11: After etching the silicon substrate using KOH, the membrane is thinned down using HF to obtain the layer stack above.

Figure 5.2. Conventionally only part of the ring resonator is underetched [16] but due to suboptimal alignment accuracy in our contact lithography, we opted for a larger membrane that holds almost the entire structure. Figure 5.12 shows indeed that the spectral position of a resonance in the ring resonator shifts under the influence of pressure. As expected, Figure 5.13 shows that the position of the resonance peak is non-linearly related to the applied pressure. The final layer stack of the characterised device is as follows: the BOX layer is thinned down to 1.54 µm, the silicon waveguides are 220 nm thick and a 1.52-µm-thick top silicon dioxide layer, resulting in a total membrane thickness of 3.28 µm (see Figure 5.11). The resonances of a non-etched ring resonator on a thinned chip also shift when pressure is applied on the sensor, albeit in a negligible manner (17 pm compared to 208 pm of an underetched sensor). As stated above, in the first design of the chip holder, we were only able to apply a positive pressure difference up to +10 kPa. We did not remeasure these sensors with the improved design of the holder, using mechanical clamping, but instead opted to focus on next generation devices.

As already discussed in Chapters 2 and 4, integrated Mach-Zehnder interferometers (MZIs) can also be used to monitor a shift in the wavelength spectrum. As can be seen in Figure 5.14a, a large portion of one arm of an MZI can be located on a pressure-sensitive membrane. The wavelength shift of its spectral features in function of the applied pressure difference is shown in Figure 5.15. As predicted, we see that by decreasing the membrane thickness (through means of a 10-s HF dip), we can greatly enhance the sensitivity (from 755 pm to 1585 pm). Apart from the increased sensitivity compared to the ring resonator, we see that the wavelength shift is now positive (red shift) when increasing the negative pressure difference while it was negative in the case of the ring resonator. As seen in Section 5.2, this change is caused by the great difference in topography between a ring resonator and an MZI. Furthermore, the layer stack used in these second generation devices is somewhat different: the final layer stack is 220 nm of silicon on 1.8 µm of buried oxide without a top silicon diox-

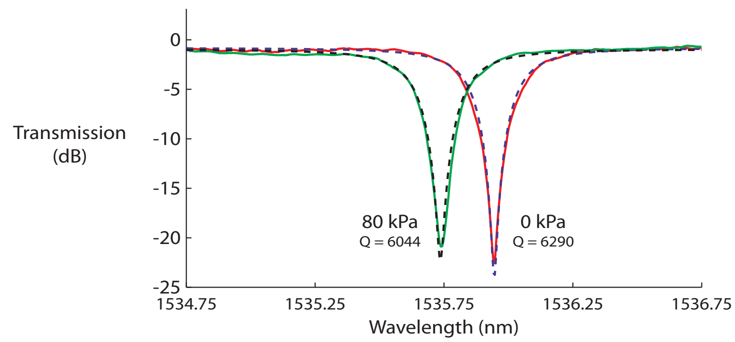

Figure 5.12: Applying a differential pressure over a thin membrane holding a ring resonator makes the resonances shift due to the elasto-optic effect. The quality factor of the resonance does not change significantly.

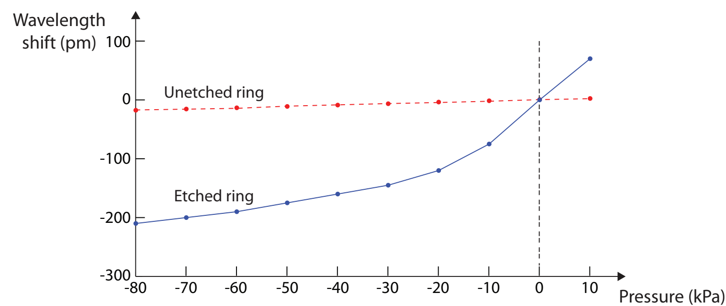

Figure 5.13: Going from 0 to -80 kPa, a resonance peak of an underetched resonator can shift by an amount of 208 pm while that of a ring resonator on a non-etched, 250-µm-thin sample shifts by only 17 pm.

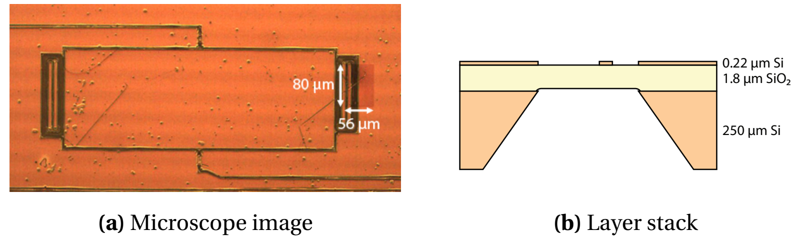

(a) Microscope image

(b) Layer stack

Figure 5.14: Sensitive pressure sensors can be produced when a large portion of one arm of an integrated Mach-Zehnder interferometer is located on a pressure-sensitive membrane.

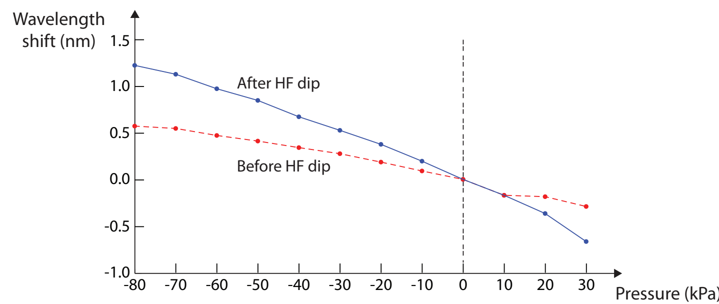

Figure 5.15: When underetching one arm of a Mach-Zehnder interferometer, we also obtain a pressure sensor (where spectral features can shift by an amount of 755 pm, going from 0 to -80 kPa). By further thinning of the membrane, the sensitivity increases even further (1585 pm, going from 0 to -80 kPa).

ide layer, so the total membrane thickness amounts to 2.02 μm. Not only is the thickness different but also whereas the waveguide in the ring resonator sensor was located in the middle of the membrane, it is located at the top for the MZI.

A final photonic structure that we will use as a transducer for pressure sensing is a Vernier effect ring resonator. As described in Chapter 2, these structures can be made very sensitive and it is therefore interesting to have an estimate as to what typical sensitivity values would be for pressure sensing. Figure 5.17 illustrates that, instead of the usual data fitting of one resonance peak to an analytical model, the data analysis process now comprises two steps: first, all individual peaks are fitted to their typical Lorentzian shape. Second, using the resulting peak values, a large Lorentzian envelope is fitted. It is the central wavelength of this envelope that is monitored to determine the wavelength shift in function of the applied pressure. Figure 5.16a shows one of the two ring resonators that are placed in cascade so as to achieve the Vernier effect. The wave-

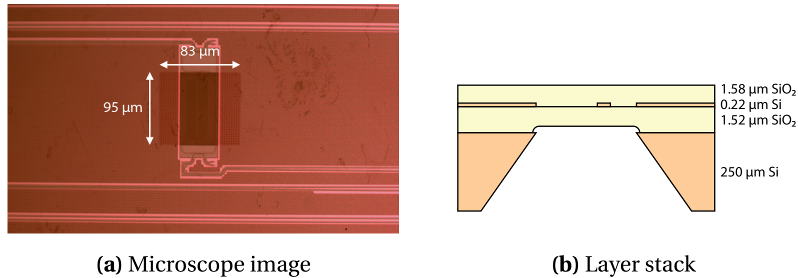

(a) Microscope image **(b)** Layer stack

Figure 5.16: As is the case for biosensing, the sensitivity of a regular ring resonator can be greatly improved by making use of the Vernier effect. The reference ring resonator is not pictured here.

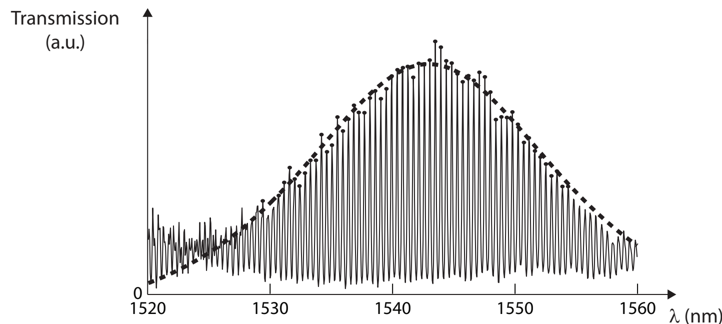

Figure 5.17: In a Vernier effect ring resonator, the combined resonance peaks form an envelope function which is used to monitor the wavelength shift.

length shift in function of the applied pressure difference is shown in Figure 5.18. A shift of 2.175 nm, going from 0 to -80 kPa, can be achieved for the pictured device with the following layer stack: a 220-nm silicon layer sandwiched between a buried oxide layer with thickness 2.0 µm and a top oxide thickness of 1.85 µm giving a total membrane thickness of 4.07 µm. When decreasing the thickness using a one-minute HF etch, the buried oxide and top oxide thickness have decreased to 1.52 µm and 1.58 µm respectively, according to scanning electron microscope (SEM) measurements. The resulting wavelength shift increases to 6.322 nm over the same pressure range.

In the above, we have characterised a variety of photonic structures that can be used as an integrated optical pressure sensor in Silicon-on-Insulator. Although the proposed devices already exhibit a high sensitivity, there is still room for improvement: it has been shown that a membrane where the length-

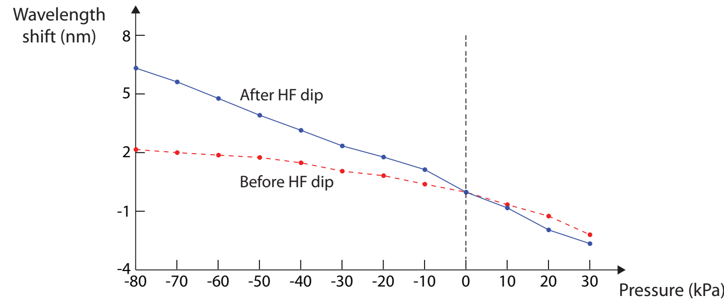

Figure 5.18: Using a Vernier effect ring resonator, the total shift of 2.175 nm, going from 0 to -80 kPa, can be increased to 6.322 nm by thinning down the membrane.

/width ratio equals 2, will produce a more sensitive device [14] (in our case it was approximately 1). Although some authors suggest [14, 16] that using Transverse Magnetic-like (TM-like) polarised light increases the sensitivity of optical pressure sensors in certain other material systems, we have not been able to see this in our basic simulations for Silicon-on-Insulator and have not verified this experimentally because of the same reasons mentioned in Chapter 4. Third, the membrane thickness can be further decreased although care should be taken that the membranes do not become too fragile and the effects of buckling behaviour might play an important role in the sensor response. Another design improvement that can be made is using several pressure-sensitive membranes in series as demonstrated by Porte [13]. Although this could circumvent the problem of buckling in large membranes, the spacing of the membranes (and as a consequence the eventual footprint of the sensor) is limited by the anisotropic silicon etch. However, perhaps one of the most important issues is fabrication process control: due to suboptimal alignment during contact lithography, the reproducibility of the proposed sensors is quite low. Furthermore, a well-controlled etch process should be used as to be able to accurately define the layer stack. As we have seen in the simulations, small changes in the layer stack can have significant effects on the sensor response. In any case, due to the non-linear behaviour of the sensor, proper characterisation of the resulting device is required.

Table 5.2 shows a comparison between the pressure sensors we have designed over the course of this work and some other devices published in literature. Since not all devices, including the ones we characterised, exhibit linear behaviour, we compare the total wavelength shift of a certain spectral feature for a pressure difference of 100 kPa (in our case: from -80 kPa to +20 kPa). We have divided the table into two categories: the first section lists integrated pressure

Type	λ shift over 100 kPa
SOI Ring resonator	0.15 nm [39]
SOI Ring resonator	0.21 nm
Si_3N_4	0.80 nm [13]
SOI MZI	1.59 nm
SOI Vernier	8.24 nm
Fibre Bragg Grating	82.1 nm [38]
All-silica FP membrane	1100 nm [4]
Graphene FP membrane	6300 nm [20]
Silver FP membrane	7050 nm [7]

Table 5.2: When comparing the proposed pressure sensors (set in cursive) to some devices published in literature, we see that our sensors are at the top of the integrated variants. FP denotes a pressure sensor based on a Fabry-Perot cavity.

sensors on a certain material platform while the second category encompasses fibre-based sensors where a Fabry-Perot (FP) cavity has been implemented at the fibre tip. For completeness, we mention one result obtained using a Fibre Bragg Grating: Sheng [38] was able to measure a wavelength shift of 82.1 nm for the above-mentioned pressure range. Fibre Bragg Grating-based sensors are in general not used for pressure sensing but are more commonly employed for strain measurements [17, 18].

It is clear that the sensitivity of integrated pressure sensors is a few orders of magnitude lower than FP cavity based devices and to a lesser extent than FBG-based sensors. However, each sensor type has its own advantages and specific applications: one of the strengths of the integrated pressure sensors is their small footprint. In our experiments, we have used an externally coupled source and detector but in theory, it is possible to integrate these two components on the same chip as the transducer. In some cases, a large sensitivity can become a drawback: consider the fibre with the silver FP membrane, with a sensitivity of 70.5 nm/kPa. If we would like to detect a shift of more than 1 kPa, the free spectral range between subsequent spectral dips should be more than 70.5 nm to avoid aliasing effects. One could argue that the free spectral range is a design parameter but it should also be taken into account that in practice, the source and detector have a limited bandwidth (a typical superluminescent LED (SLED) has a bandwidth of around 100 nm). When comparing the proposed devices to other integrated sensors, we see that our devices rank at the top. At around the same time we published our first results [40] of a ring resonator, Zhao et al. [39] published a very similar structure, albeit with a larger footprint and smaller sensitivity. Note that when sensor size is of the essence, the less sensitive ring res-

onator can be implemented, having a footprint of less than 100 × 100 μm^2.

5.4 Conclusions

We have demonstrated a variety of optical pressure sensors integrated in a Silicon-on-Insulator platform. We have seen that much care has to be taken when performing numerical analysis since a lot of parameters have to be taken into account that can all have a significant effect on the response of the sensor. The characterised devices show a sensitivity that ranks at the top of integrated sensors published in literature, combined with a relatively small footprint (made possible through the high refractive index contrast of SOI). Due to the non-linear dependence of the wavelength shift of spectral features under influence of an applied pressure difference, it is not straightforward to determine a sensitivity per unit of pressure but a wavelength shift of 8.24 nm going from -80 kPa to +20 kPa has been demonstrated. Design and fabrication improvements could even further increase this figure.

References

[1] V. Mortet, R. Petersen, K. Haenen, and M. D'Olieslaeger. *Wide range pressure sensor based on a piezoelectric bimorph microcantilever.* Applied Physics Letters, 88(13):133511, 2006.

[2] I. Manunza, A. Sulis, and A. Bonfiglio. *Pressure sensing by flexible, organic, field effect transistors.* Applied Physics Letters, 89(14):143502, 2006.

[3] M. A. Fonseca, J. M. English, M. von Arx, and M. G. Allen. *Wireless Micromachined Ceramic Pressure Sensor for High-Temperature Applications.* Journal of Microelectromechanical Systems, 11(4):337–343, 2002.

[4] W. Wang, N. Wu, Y. Tian, C. Niezrecki, and X. Wang. *Miniature all-silica optical fiber pressure sensor with an ultrathin uniform diaphragm.* Optics Express, 18(9):9006–9014, April 2010.

[5] W. Wang, N. Wu, Y. Tian, X. Wang, C. Niezrecki, and J. Chen. *Optical pressure/acoustic sensor with precise Fabry-Perot cavity length control using angle polished fiber.* Optics Express, 17(19):16613–16618, September 2009.

[6] I. Padron, A. T. Fiory, and N. M. Ravindra. *Integrated Optical and Electronic Pressure Sensor.* IEEE Sensors Journal, 11(2):343–350, 2011.

[7] F. Xu, D. Ren, X. Shi, C. Li, W. Lu, L. Lu, L. Lu, and B. Yu. *High-sensitivity Fabry-Perot interferometric pressure sensor based on a nanothick silver diaphragm.* Optics Letters, 37(2):133–135, 2012.

[8] H.-J. Sheng, M.-Y. Fu, T.-C. Chen, W.-F. Liu, and S.-S. Bor. *A Lateral Pressure Sensor Using a Fiber Bragg Grating.* IEEE Photonics Technology Letters, 16(4):1146–1148, 2004.

[9] B. McMillen, C. Jewart, M. Buric, K. P. Chen, Y. Lin, and W. Xu. *Fiber Bragg grating vacuum sensors.* Applied Physics Letters, 87(23):234101, 2005.

[10] X. Ni, Y. Zhao, and J. Yang. *Research of a novel fiber Bragg grating underwater acoustic sensor.* Sensors and Actuators A: Physical, 138(1):76–80, 2007.

[11] S. Campopiano, A. Cutolo, A. Cusano, M. Giordano, G. Parente, G. Lanza, and A. Laudati. *Underwater Acoustic Sensors Based on Fiber Bragg Gratings.* Sensors, 9(6):4446–4454, June 2009.

[12] D. A. Singlehurst, C. R. Dennison, and P. M. Wild. *Comprising Multiplexed In-Fibre Bragg Gratings Within a Flexible Superstructure.* Journal of Lightwave Technology, 30(1):123–129, 2012.

[13] H. Porte, V. Gorel, S. Kiryenko, J.-P. Goedgebuer, W. Daniau, and P. Blind. *Imbalanced Mach-Zehnder interferometer integrated in micromachined silicon substrate for pressure sensor.* Journal of Lightwave Technology, 17(2):229–233, 1999.

[14] M. Ohkawa, M. Izutsu, and T. Sueta. *Integrated optic pressure sensor on silicon substrate.* Applied Optics, 28(23):5153–5157, December 1989.

[15] C. Wagner, J. Frankenberger, and P. Deimel. *Optical pressure sensor based on a Mach-Zehnder interferometer integrated with a lateral a-Si:H p-i-n photodiode.* IEEE Photonics Technology Letters, 5(10):1257–1259, 1993.

[16] G. de Brabander, J. Boyd, and G. Beheim. *Integrated optical ring resonator with micromechanical diaphragms for pressure sensing.* IEEE Photonics Technology Letters, 6(5):671–673, May 1994.

[17] C. Caucheteur, S. Bette, R. Garcia-Olcina, M. Wuilpart, S. Sales, J. Capmany, and P. Mégret. *Transverse Strain Measurements Using the Birefringence Effect in Fiber Bragg Gratings.* IEEE Photonics Technology Letters, 19(13):966–968, 2007.

[18] N. Liu, Y. Li, Y. Wang, H. Wang, W. Liang, and P. Lu. *Bending insensitive sensors for strain and temperature measurements with Bragg gratings in Bragg fibers.* Optics Express, 19(15):13880–91, July 2011.

[19] P. K. Pattnaik, B. Vijayaaditya, T. Srinivas, and A. Selvarajan. *Optical MEMS pressure sensor using ring resonator on a circular diaphragm.* In Proceedings of the 2005 International Conference on MEMS, NANO and Smart Systems (ICMENS'05), pages 1–4, 2005.

[20] J. Ma, W. Jin, H. L. Ho, and J. Y. Dai. *High-sensitivity fiber-tip pressure sensor with graphene diaphragm.* Optics Letters, 37(13):2493–5, July 2012.

[21] T. Claes. *Advanced Silicon Photonic Ring Resonator Label-Free Biosensors.* PhD thesis, Ghent University, 2012.

[22] S. Timoshenko and S. Woinowsky-Krieger. *Theory of plates and shells.* McGraw-Hill, 1987.

[23] W. C. Young and R. G. Budynas. *Roark's Formulas for Stress and Strain.* McGraw-Hill, 7 edition, 2002.

[24] L. D. Landau, E. M. Lifshitz, A. M. Kosevich, and L. P. PitaevskiĂŋ. *Theory of elasticity.* Butterworth-Heinemann, 1986.

[25] C. C. Davis. *The Electrooptic and Acoustooptic Acoustooptic Effects and Modulation of Light Beams.* In Lasers and Electro-optics, pages 623–639. University of Maryland, 1996.

[26] COMSOL, *http://www.comsol.com/.*

[27] M. A. Hopcroft, W. D. Nix, and T. W. Kenny. *What is the Young's Modulus of Silicon?* Journal of Microelectromechanical Systems, 19(2):229–238, 2010.

[28] J. F. Shackelford and W. Alexander. *CRC Materials Science and Engineering Handbook.* CRC Press, 2000.

[29] B. Halg. *On a nonvolatile memory cell based on micro-electro-mechanics.* In IEEE Micro Electro Mechanical Systems, pages 172–176, Napa Valley, CA, 1990.

[30] M. T. Kim. *Influence of substrates on the elastic reaction of films for the microindentation tests.* Thin Solid Films, 283(1-2):12–16, 1996.

[31] K. E. Petersen. *Dynamic micromechanics on silicon: Techniques and devices.* IEEE Transactions on Electron Devices, 25(10):1241–1250, 1978.

[32] D. J. Lockwood and L. Pavesi. *Silicon Photonics II: Components and Integration.* Springer, 2011.

[33] J. M. Gere and B. J. Goodno. *Mechanics of Materials.* Cengage Learning, 2009.

[34] J. Roels. *Actuation of integrated nanophotonic devices through the optical gradient force.* PhD thesis, Ghent University, 2011.

[35] E. Iwase, P.-C. Hui, D. Woolf, A. W. Rodriguez, S. G. Johnson, F. Capasso, and M. Loncar. *Control of buckling in large micromembranes using engineered support structures.* Journal of Micromechanics and Microengineering, 22(065028), 2012.

[36] SUNX, *http://www.panasonic.com/*.

[37] New Era Pump Systems Inc., *http://www.syringepump.com/*.

[38] H.-J. Sheng, W.-F. Liu, K.-R. Lin, S.-S. Bor, and M.-Y. Fu. *High-sensitivity temperature-independent differential pressure sensor using fiber Bragg gratings.* Optics Express, 16(20):16013–16018, 2008.

[39] X. Zhao, J. M. Tsai, H. Cai, X. M. Ji, J. Zhou, M. H. Bao, Y. P. Huang, D. L. Kwong, and A. Q. Liu. *A nano-opto-mechanical pressure sensor via ring resonator.* Optics Express, 20(8):8535, March 2012.

[40] E. Hallynck and P. Bienstman. *Integrated Optical Pressure Sensors in Silicon-on-Insulator.* IEEE Photonics Journal, 4(2):443–450, 2012.

"You're a funny guy, Sully, I like you. That's why I'm going to kill you last."

Arnold Schwarzenegger in Commando, Actor, 1947-present

6 Increased efficiency grating couplers

One of the great challenges of integrated photonics is finding a method to couple light between the photonic integrated circuit (PIC), of which an optical biosensor is an example, and the outside world (e.g. through means of an optical fibre). This problem is quite complex since we have to find a way to couple light from a single mode optical fibre (SMF) with a diameter of 10 μm to a nanophotonic waveguide of 220 nm by 450 nm and vice versa. Figure 6.1 illustrates the gravity of this dimension mismatch. Since the light coupling section of the PIC is so crucial (in case of bad coupling, very little or no light enters the circuit making proper functionality very difficult), a lot of research has been done on this issue [1–4]. Figure 6.2 shows some of the most commonly methods used nowadays. The simplest solution is placing the optical fibre very close to the nanophotonic waveguide in such a way that maximal modal overlap occurs (see Figure 6.2a). The resulting transmission loss of 26 dB [2] can be reduced by inserting a lens in-between the fibre and the waveguide, either in a discrete form or integrated in the optical fibre (i.e. a lensed fibre). However, for sub-micron waveguides, alignment is very critical. Another way to tackle the coupling problem is introducing a tapered spot-size converter as illustrated in Figure 6.2b. When properly designed, this 3D structure can gradually convert the large optical mode of the fibre to the small mode of the waveguide without, in theory, any loss. Although the coupling loss can be reduced down to -3.5 dB [5], three-dimensional structures are in general not easy to fabricate and

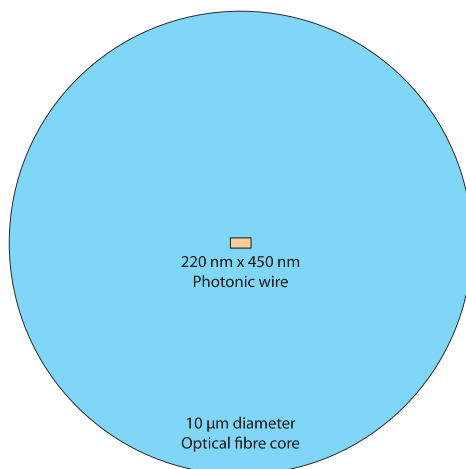

Figure 6.1: Due to the large mismatch in size between an optical fibre and a nanophotonic waveguide, it is not straightforward to efficiently couple both light modes.

the length of such a taper can easily exceed 500 µm. It is possible to decrease the length of this taper by employing an inverted taper: instead of expanding the taper dimensions when going from the waveguide mode to the fibre mode, the sizes are decreased: when a waveguide becomes too small for a certain wavelength, the waveguide mode expands. Although these structures can be made shorter, they are even more difficult to fabricate because of their small dimensions (starting from an already small 220 nm by 450 nm, the sizes have to decrease). A 2D variant on this inverted taper exists where the spot-size is only converted in the lateral direction while the vertical conversion is handled by an intermediary waveguide [6].

The percentage of light that is converted from the optical fibre to the nanophotonic waveguide (i.e. the coupling efficiency) is not the only figure of merit of a light coupling method; other factors like ease of fabrication, alignment tolerance and bandwidth are equally important. The coupling scheme that we will focus on in this chapter is a waveguide grating coupler (see Figure 6.2c). Using the fabrication process described in Chapter 3 and by applying a metallic mirror at the bottom of these devices, we will see that we can increase their coupling efficiency. Fabrication of the proposed devices was done by ourselves while simulations and measurements were carried out by Diedrik Vermeulen of Acacia Communications.

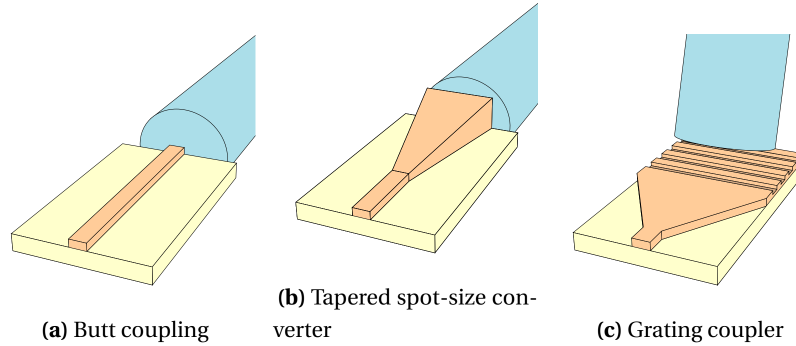

(a) Butt coupling **(b)** Tapered spot-size converter **(c)** Grating coupler

Figure 6.2: 3 of the most commonly found coupling methods between an optical fibre and a nanophotonic waveguide.

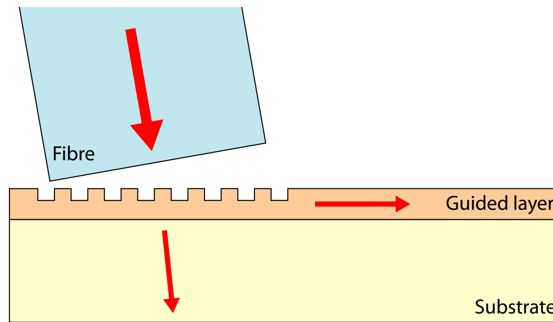

Figure 6.3: A Bragg grating can diffract light from an optical fibre into a nanophotonic waveguide. Note that sometimes, other diffraction orders exist that direct light towards the substrate where it is generally lost.

6.1 Grating coupler theory

A grating coupler is a type of photonic crystal that can couple light at a certain combination of wavelength, polarisation and incidence angle to a nanophotonic waveguide as shown in Figure 6.3. To explain this behaviour, we make use of Bragg's law [7]:

$$\vec{k_{out}} = \vec{k_{in}} + m\vec{K} \tag{6.1}$$

Here, $\vec{k_{out}}$ and $\vec{k_{in}}$ are the resulting and incident wavevectors respectively and $\vec{K}$ is the reciprocal lattice vector of which the magnitude is defined as $\frac{2\pi}{\Lambda}$ where Λ is the period of the grating. The magnitude of a wavevector $\vec{k}$ is given by $k_0 n$ with n the refractive index of the medium in which the wave propagates and k_0

its wavevector in vacuum. Therefore, we can represent Bragg's law graphically as illustrated in Figure 6.4. The wavevectors $\vec{k}$ are represented by circles with radius $k_0 n$ where n can be the refractive index of the top cladding layer or the substrate of the grating coupler or in the case of the waveguide, the effective index of the waveguide mode to which coupling is desired. Note that we will explain the graphical interpretation of Bragg's law here by coupling light from a waveguide into an optical fibre as to not overload the picture. Since the structure is reciprocal, a grating with the same period can be used to couple light from a fibre into a waveguide. Through the intersection of the incident wavevector $\vec{k_{in}}$ with its corresponding circle, a vertical line can be constructed indicating zeroth order diffraction or Snell's law (i.e. conservation of the parallel wavevector). However, in this particular case where k_{in} corresponds to the wavevector in the waveguide, there are no intersections. If we now construct other vertical lines, spaced with a distance $\frac{2\pi}{\Lambda}$, we can choose Λ in such a way that one of the vertical lines coincides with the circle of the effective index of the waveguide mode.

For the case of vertical incidence it is clear from Figure 6.4 (top) that the grating period Λ should be chosen so that $\left|\vec{K}\right| = k_0 n_{eff}$. This implies $\Lambda = \frac{\lambda_0}{n_{eff}}$ where λ_0 is the wavelength of the incident light in vacuum. However, we see in Figure 6.4 (top) that, due to symmetry arguments, light is not only coupled in the two vertical directions ($k_{out,-1}$) but also in the opposite direction of the waveguide, indicating reflection ($k_{out,-2}$). Although a structure can be devised that also collects this light and combines it with the light travelling in the right direction, it is easier to break the symmetry by tilting the optical fibre slightly. As is apparent from Figure 6.4 (bottom), this diffraction order vanishes when the fibre is placed under an angle θ with the normal to the grating surface. Bragg's law becomes $\left|\vec{K}\right| = k_0 \left(n_{eff} - n_{incident} \sin\theta\right)$. The period of the grating should be chosen then as $\Lambda = \frac{\lambda_0}{n_{eff} - n_{incident} \sin\theta}$.

Bragg's law is a mathematical formulation that only holds for infinite gratings. In practice, we will make a finite grating that is approximately as long as the optical fibre diameter (see Figure 6.3) so that all light is efficiently collected by the grating. One could argue to make the grating longer to increase alignment tolerance. However, one effect of using a finite grating instead of the theoretical infinite grating is that the former has a certain bandwidth that increases with a decreasing number of periods in the grating: while for an infinite grating, incident light at an angle θ=10°will couple to the waveguide mode, light at an angle θ=9°will not. Due to the bandwidth of finite gratings, light at an angle $\theta = 9°$ will also be coupled to the waveguide mode, be it less efficiently. A high bandwidth is desired in coupling schemes and therefore, we do not wish to make the grating longer than necessary. Note that a grating coupler only changes the direction of the light; a lateral 2D taper converts the spot-size of a 220 nm by 10

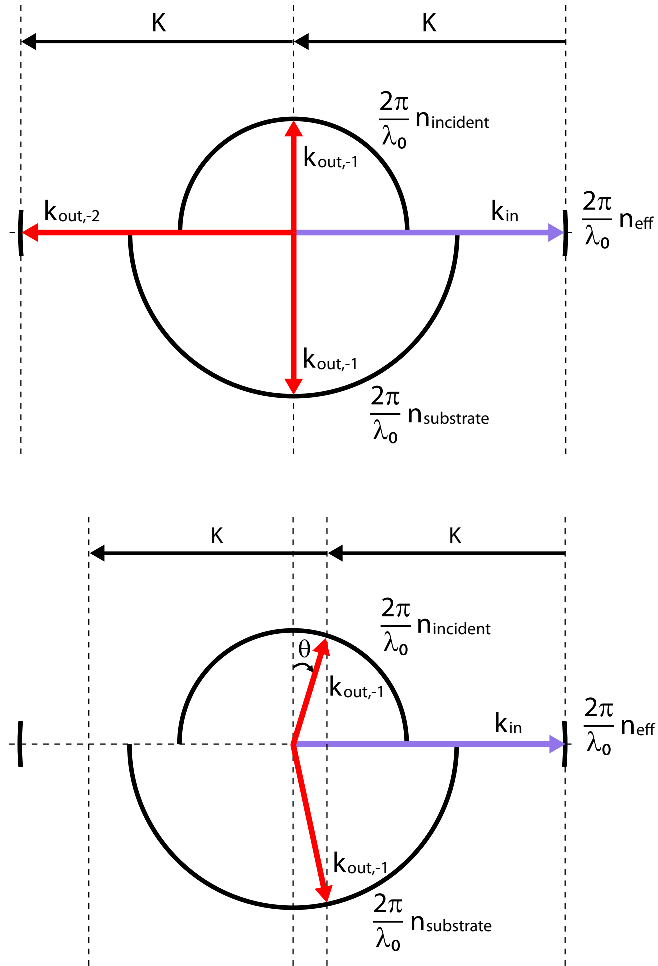

Figure 6.4: A graphical representation of Bragg's law. When $\vec{K}$ is chosen in such a way that we want the waveguide mode to couple light to a vertically positioned optical fibre, part of the light will be reflected back into the waveguide, due to symmetry. Breaking this symmetry, by tilting the fibre, prevents this unwanted second order diffraction. However, a portion of the light will always couple to the substrate.

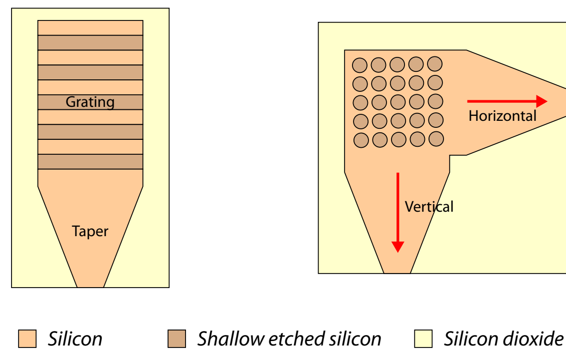

Figure 6.5: The left figure shows a top view of a standard grating coupler with taper to convert the mode size in the lateral direction. The right figure illustrates a 2D grating coupler which couples both TE- and TM-like modes simultaneously.

μm waveguide to that of a 220 nm by 450 nm waveguide (see Figure 6.5).

Grating couplers are easy to fabricate in Silicon-on-Insulator (SOI) using a standard Deep UV lithography process [8] and a shallow etch step of 70 nm depth and can be placed anywhere on a chip or wafer. The optical fibre is simply positioned above the grating without a need for cleaved and polished facets, as would be the case for butt coupling or the spot-size converters mentioned above. Another advantage is the alignment tolerance of a grating coupler: an alignment error of 1 μm results in a penalty of only 0.5 dB [2]. Although this component is polarisation sensitive, advanced implementations of the standard grating coupler depicted in Figure 6.2c have been demonstrated. In general, the polarisation of the light coming out of a fibre is not linearly polarised but elliptically polarised (i.e. a superposition of two linearly polarised modes). Standard grating couplers only work efficiently for light with a polarisation parallel to the grating lines (from a waveguide point-of-view Transverse Electric-like (TE) light). The orthogonal polarisation in an optical fibre will therefore experience very poor coupling. By adding another waveguide to the grating, perpendicular to the already present one and transforming the 1D grating coupler into a 2D grating coupler we can, in first order approximation, treat the resulting structure as a superposition of a grating coupler that couples light with one polarisation (e.g. horizontal with respect to a certain axis) and a grating coupler that couples light with the orthogonal polarisation (vertical with respect to the same axis). This is further illustrated in Figure 6.5. In theory, the combined light coupled into both waveguides should remain constant no matter what the input polarisation from the optical fibre might be.

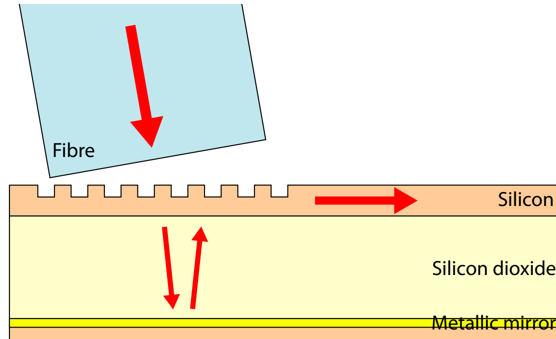

Figure 6.6: By applying a metallic mirror between the BOX-silicon substrate-interface, the light that is diffracted downwards is reflected upwards. Part of this reflected right is also coupled into the waveguide. If a proper thickness of the BOX layer is chosen, both waves entering the waveguide can interfere constructively.

However, two major drawbacks of this device still remain: coupling efficiency and wavelength bandwidth. The poor coupling efficiency is partly due to the fact that light is lost in the first order diffraction mode towards the substrate. In SOI there is a silicon dioxide layer in-between the light-guiding silicon top layer and the silicon substrate. By applying a mirror coating between this buried oxide (BOX) layer and the substrate, that light will be reflected towards the grating structure where a substantial part is coupled again into the waveguide (see Figure 6.6). Although this has already been demonstrated by Van Laere [9] using a wafer-to-wafer bonding approach, we will see that, using the fabrication process described in Section 3.2, it is also possible to apply a mirror coating under the BOX layer. Furthermore, if deemed necessary, the BOX layer thickness can also be tuned using HF etching.

6.2 Simulations

Using 3D Finite Difference Time Domain (FDTD) simulations, we can calculate the coupling efficiency from an optical fibre to a nanophotonic waveguide by calculating the overlap integral between the optical fibre mode and the radiated field of the grating coupler. Besides the efficiency improvement caused by the metal mirror, it is worth investigating whether the thickness of the BOX layer is optimal so that constructive interference is achieved between the directly coupled wave and the reflected wave. Figure 6.7 shows the coupling efficiency as a function of the BOX layer thickness for a focusing grating coupler: a type of grating coupler with curved grating lines that simultaneously acts as a lens that

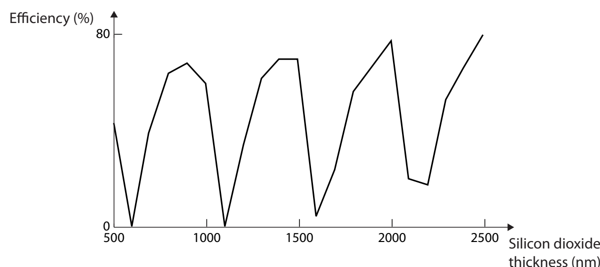

Figure 6.7: The coupling efficiency as a function of the buried oxide layer thickness for a focused grating coupler reaches maxima for a BOX thickness of 900 nm, 1400 nm and 2000 nm.

focuses the diffracted light directly on a small waveguide, without the need for a taper [10]. We observe constructive interference (and thus maximal coupling efficiency) for a BOX thickness of 900 nm, 1400 nm and 2000 nm. Since the BOX thickness of standard SOI wafers used in our group is in fact 2 μm, this makes an HF etching step to modify the thickness unnecessary. From the graph in Figure 6.7, we also see that a coupling efficiency of over 70% can be achieved using this mirror, while standard grating couplers usually reach maxima that are roughly half of that [9].

Another interesting structure to investigate is the already mentioned 2D grating coupler that can couple perpendicular polarisations simultaneously. Figure 6.8 shows simulation results for such a 2D grating coupler with a period of 605 nm and a hole radius of 195 nm. Although, in theory, the polarisation state of the incident light should have no effect on the efficiency, in practice there is a polarisation where maximum efficiency is achieved and one where minimum efficiency is achieved [2]. The efficiency as a function of the wavelength is shown for both the minimum and maximum polarisation, in cases with and without a bottom mirror. For both polarisations, we see that the efficiency is roughly doubled due to the introduction of the bottom mirror.

In the above simulations a 100-nm-thick gold mirror was used due to its excellent reflective properties [11] in the infra-red wavelength range. In practice, the adhesion of gold to silicon dioxide is in general not adequate [12, 13]. Therefore, an intermediate layer of titanium dioxide is introduced between silicon dioxide and gold to improve the adhesive properties. The titanium dioxide should be chosen sufficiently thin as to not introduce extra absorption losses.

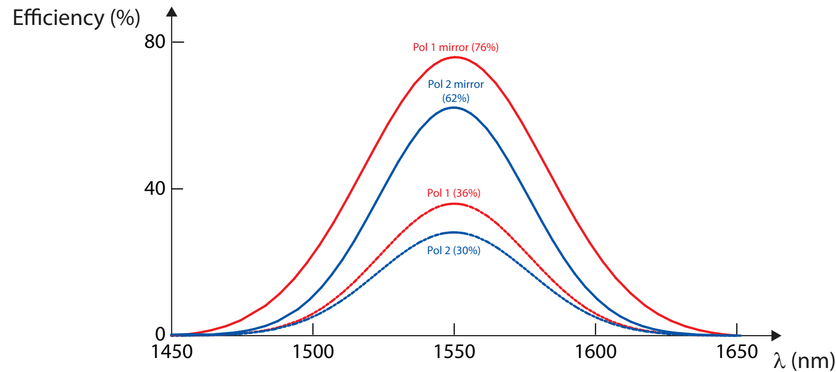

Figure 6.8: The coupling efficiency in function of the wavelength λ is shown for TE- and TM-like polarised light for the cases with and without a bottom mirror. The efficiency is roughly doubled due to the mirror.

6.3 Measurements

Starting from SOI chips with several grating coupler designs placed on them, we use the fabrication steps described in Chapter 3 to remove the substrate under the grating couplers. Since no further HF etching is required, we can immediately deposit a metal mirror on the silicon dioxide layer. Before depositing 100 nm of gold, we perform a titanium flash deposition [14] which oxidises to form a layer of titanium dioxide that is sufficient for proper adhesion but thin enough as to not introduce noticeable coupling efficiency loss. A picture of a die with a gold layer deposited at the substrate side is shown in Figure 6.9a. Figures 6.9b and 6.9c show a 1D and 2D grating coupler respectively where the yellowish region indicates that a gold bottom mirror is present under these structures.

Due to the fabrication process used, a silicon dioxide and silicon nitride layer still remain on top of the structures. Although the exact transmission loss due to this layer stack has to be calculated using FDTD simulations, we can illustrate the effect of the silicon nitride layer by assuming a semi-infinite slab of air at one side of the layer and another semi-infinite slab of silicon dioxide at the other side. Using a transfer matrix method, we can calculate that for silicon nitride with a refractive index of 1.8, a typical value for silicon nitride deposited in our clean rooms, the transmission will not drop below 85% for any given layer thickness. In the actual case of a layer thickness of 400 nm, the transmission is around 96%. Since the silicon nitride layer thickness is not very critical in the fabrication process, it can be tuned to a certain extent to allow for maximal transmission: the maximum value of 96.5% is achieved for a thickness of 432 nm. In our experiments we will make use of index matching fluid (IMF): this

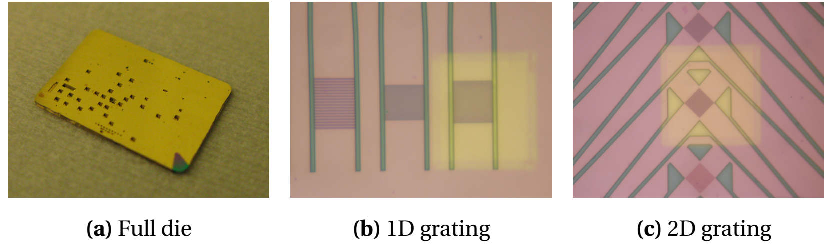

(a) Full die **(b)** 1D grating **(c)** 2D grating

Figure 6.9: (a) shows an etched SOI die with a gold layer; (b) and (c) respectively show a 1D and 2D grating coupler with golden bottom mirror.

liquid has a very similar index to that of silicon dioxide in the wavelength range of our interest and can be easily applied on the die after which the fibre tip is immersed in it. Since the light then doesn't travel through an air layer anymore, the index contrast between the incident medium and the silicon nitride is decreased. The transmission for a 400-nm silicon nitride layer becomes 99.8%. We restate however that these calculations are illustrative and exact values have to be extracted from 3D FDTD simulations.

Apart from the silicon nitride layer, the silicon dioxide layer will also have an effect: changing the refractive index of the top cladding layer of a grating coupler will not significantly change the absolute value of the coupling efficiency (unless the material has a non-negligible imaginary part of the refractive index) but will cause a shift in the wavelength spectrum. From the condition $\Lambda = \frac{\lambda_0}{n_{eff} - n_{incident} \sin\theta}$, we can expect that the wavelength spectrum will shift to shorter wavelengths (i.e. blue shift) when increasing the refractive index of the top cladding layer (from 1.0 of air to 1.444 of silicon dioxide).

Using a measurement set-up similar to the one described in Section 4.3.1 (the only difference is that the chip holder does not have to be able to apply pressure to the sample), the grating couplers were characterised. Figure 6.10 shows the coupling efficiency in function of the wavelength λ for a 1D grating with bottom mirror using TE-like polarised light and for a 2D grating for both orthogonal polarisations and also for the case without a bottom mirror. The 1D grating has a period of 630 nm while the 2D grating has a period of 605 nm and a hole radius of 195 nm. Both grating couplers are fabricated in the same layer stack used throughout this PhD: 220 nm silicon as the light guiding layer on 2 μm silicon dioxide on a 250-μm-thick silicon substrate.

When talking about an overall power budget in a circuit, it is more practical to use a dB-scale since the total power loss is simply the sum of all losses in dB. A 69.96% coupling efficiency of the 1D grating coupler corresponds to a coupling loss of -1.55 dB. For the 2D grating coupler, the coupling loss has been decreased from -5.25 dB and -5.96 dB for the maximum and minimum polari-

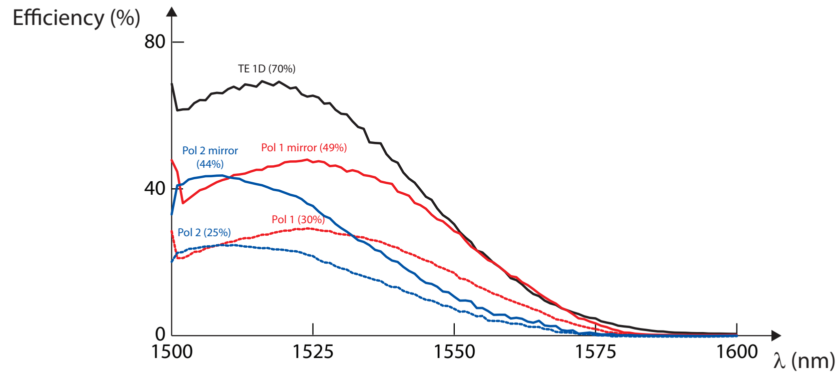

Figure 6.10: The 1D grating coupler achieves a peak coupling efficiency of almost 70%. For the 2D grating coupler, we see for both polarisations a substantial increase in coupling effiency.

sation respectively to -3.13 dB and -3.54 dB. As expected, the peak of the wavelength spectrum is not located around 1550 nm but it is blue shifted by over 30 nm.

For the case of the 1D grating coupler, these results agree with our simulations and also with the results published by Van Laere [9]. At around the same time we obtained our results, Zaoui et al. [15] published their results of the same concept, be it with a different layer stack (i.e. different silicon and silicon dioxide thickness and an aluminium mirror). They achieved a coupling loss of -1.63 dB, again comparable to what we achieved.

The measured efficiency of the 2D grating coupler is less than the simulated value but the positive effect of the metal mirror is apparent from the comparison with the case without a bottom mirror. The fact that the peak wavelengths for the minimum and maximum polarisation don't match might be caused by imperfect symmetry: the projected axis of the optical fibre should coincide with the bisector of both perpendicular waveguides. To our knowledge, no other research groups have published results on a 2D grating coupler structure with a metal bottom mirror in SOI. The PhD work of Frederik Van Laere [16] does contain results for a structure in indium phosphide.

6.4 Conclusions

Coupling light from an optical fibre to a nanophotonic waveguide is an important issue in photonic integrated circuits. Despite its good alignment tolerance and ease of fabrication, the grating coupler is traditionally not the best in terms

of coupling efficiency and bandwidth. The poor coupling efficiency is explained by the fact that in a grating coupler, part of the first order diffracted light is directed towards the substrate. Using a fabrication process to etch the silicon substrate under the grating couplers and applying a metallic mirror, we are able to reflect this light back into the grating coupler structure where part of it can constructively interfere with the already coupled part of the light. We have experimentally shown a significant increase in the coupling efficiency of both 1D and 2D grating couplers. Although this principle has already been demonstrated in the past [9], we believe that by removing the substrate locally instead of completely and replacing it by a new carrier substrate using wafer-to-wafer bonding, the fabrication process to obtain these structures is simpler. Furthermore, since the same process is used to fabricate the biosensors and/or pressure sensors described in Chapters 4 and 5 respectively, these improved efficiency grating couplers could easily be implemented in said devices.

References

[1] F. M. Soares, F. Karouta, E. J. Geluk, J. H. C. van Zantvoort, H. De Waardt, R. Baets, and M. K. Smit. *Extremely low-loss vertically-tapered spot size converter in InP-based waveguide structure.* In Proceedings Symposium IEEE/LEOS Benelux Chapter, pages 127–130, Ghent, 2004.

[2] D. Taillaert. *Grating couplers as Interface between Optical Fibres and Nanophotonic Waveguides.* PhD thesis, Ghent University, 2004.

[3] J. V. Galan, P. Sanchis, J. Martí, S. Marx, H. Schroeder, B. Mukhopadhyay, T. Tekin, S. Selvaraja, W. Bogaerts, P. Dumon, and L. Zimmermann. *CMOS compatible silicon etched V-grooves integrated with a SOI fiber coupling technique for enhancing fiber-to-chip alignment.* In 6th IEEE International Conference on Group IV Photonics, pages 148–150, San Francisco, 2009.

[4] D. Vermeulen, S. Selvaraja, P. Verheyen, G. Lepage, W. Bogaerts, P. Absil, D. Van Thourhout, and G. Roelkens. *High-efficiency fiber-to-chip grating couplers realized using an advanced CMOS-compatible Silicon-On-Insulator platform.* Optics Express, 18(17):18278–18283, 2010.

[5] A. Sure, T. Dillon, J. Murakowski, C. Lin, D. Pustai, and D. W. Prather. *Fabrication and characterization of three-dimensional silicon tapers.* Optics Express, 11(26):3555–3561, 2003.

[6] S. J. McNab, N. Moll, and Y. A. Vlasov. *Ultra-low loss photonic integrated circuit with membrane-type photonic crystal waveguides.* Optics Express, 11(22):2927–2939, 2003.

[7] W. L. Bragg. *The Diffraction of Short Electromagnetic Waves by a Crystal.* Proceedings of the Cambridge Philosophical Society, 17:43–57, 1913.

[8] S. K. Selvaraja, S. Member, P. Jaenen, W. Bogaerts, D. V. Thourhout, P. Dumon, and R. Baets. *Fabrication of Photonic Wire and Crystal Circuits in Silicon-on-Insulator Using 193nm Optical Lithography.* Journal of Lightwave Technology, 27(18):4076–4083, 2009.

[9] F. Van Laere, G. Roelkens, M. Ayre, J. Schrauwen, D. Taillaert, D. Van Thourhout, T. F. Krauss, and R. Baets. *Compact and Highly Efficient Grating Couplers Between Optical Fiber and Nanophotonic Waveguides.* Journal of Lightwave Technology, 25(1):151–156, 2007.

[10] F. Van Laere, T. Claes, J. Schrauwen, S. Scheerlinck, W. Bogaerts, D. Taillaert, L. O'Faolain, D. Van Thourhout, and R. Baets. *Compact Focusing Grating Couplers for Silicon-on-Insulator Integrated Circuits.* IEEE Photonics Technology Letters, 19(23):1919–1921, 2007.

[11] M. Bass, C. DeCusatis, J. Enoch, V. Lakshminarayanan, G. Li, C. MacDonald, V. Mahajan, and E. Van Stryland. *Handbook of Optics Volume II.* McGraw-Hill Professional, 3 edition, 2009.

[12] K. W. Vogt, P. A. Kohl, W. B. Carter, R. A. Bell, and L. A. Bottomley. *Characterization of thin titanium oxide adhesion layers on gold: resistivity, morphology and composition.* Surface Science, 301(1-3):203–213, 1994.

[13] J. O. Tegenfeldt, A. A. Zakharov, M. Beck, R. Bunk, E. Forsen, and L. Montelius. *Fabrication and characterization of a molecular adhesive layer for micro- and nanofabricated electrochemical electrodes.* Microelectronic Engineering, 68:887–892, 2003.

[14] D. M. Mattox. *Handbook of Physical Vapor Deposition (PVD) Processing.* William Andrew, 2 edition, 2010.

[15] W. S. Zaoui, M. F. Rosa, W. Vogel, M. Berroth, J. Butschke, and F. Letzkus. *Cost-effective CMOS-compatible grating couplers with backside metal mirror and 69 % coupling efficiency.* Optics Express, 20(26):B238–243, 2012.

[16] F. Van Laere. *Photonic Integrated Circuits and Fibre Couplers Based on InP Bonded Membranes.* PhD thesis, Ghent University, 2008.

"Some cause happiness wherever they go; others whenever they go."

Oscar Wilde, Author, 1854-1900

7 Conclusions and perspectives

7.1 Conclusions

When we only rely on diffusion, the delivery time for low concentration analytes in some biosensors can exceed days or weeks. This can be improved by creating a laminar flow near the sensor surface so that biomolecules in the analyte get transported through convection. However, for certain cases, this flow scheme is not enough and more advanced solutions are required. One of the possibilities is directing the flow through the transducer. By applying a droplet of analyte on the sensor and exerting pressure on the liquid, the droplet can be pulled or pushed through the sensor membrane (depending on whether the pressure difference compared to atmospheric pressure is negative or positive).

We have seen that several basic photonic structures that are commonly used as biosensors, can also be adapted to direct the flow through the transducer. Next to the conventional sensing methods, we have proposed a novel sensing method using photonic crystals where measurements are performed in the angular spectrum instead of the more commonly used wavelength spectrum. The main advantage of this method that there is no need to implement a tunable wavelength source.

Nevertheless, we decided to focus on the more mature designs of ring resonators, Mach-Zehnder interferometers and photonic crystals. We developed a fabrication process to produce thin membranes with holes for Silicon-on-

Insulator. Using KOH we anisotropically etched the silicon substrate after which the buried silicon dioxide layer could be removed using HF (either in liquid or vapour phase). All relevant parameters and common pitfalls are mentioned for the reader wanting to reproduce this technique.

After a theoretical and short numerical study of the fluidic aspects of transporting a droplet through a membrane with holes, we used this fabrication process to produce the envisioned biosensors, making use of both photonic crystals and Mach-Zehnder interferometers. The measurements of photonic crystal biosensors did not produce any relevant results which was likely caused by the sensitivity of these periodic structures to deviations from the unit cell caused by a variety of factors. For the Mach-Zehnder-interferometer-based biosensors on the other hand, we were able to show an improvement of the detection time by at least a factor of 3 for Bovine Serum Albumin binding to silicon in a proof-of-principle experiment. Since no appropriate surface chemistry was available at the time, we could not perform experiments using other types of biomolecules and in particular low-concentration analytes.

Apart from fabricating biosensors based on a thin membrane with holes, we could also use the above-mentioned fabrication process and photonic structures to produce optical pressure sensors. We have seen that it is not straightforward to numerically predict the wavelength shift of spectral features of these devices in function of the applied pressure based on a few simplified simulations. We were however able to characterise three types of sensors (all based on different optical structures) where the Vernier effect ring resonator performed the best with a sensitivity of 8.24 nm over a pressure range of 100 kPa. This is roughly one order of magnitude better than other integrated optical pressure sensors described in literature.

A final application of the process to locally etch the silicon substrate is improving the efficiency of grating couplers. These structures, that are used to couple light between an optical fibre and a nanophotonic waveguide, generally exhibit a poor coupling efficiency, mainly due to the fact that part of the light is directed towards the substrate where it is lost. By etching the substrate under the grating couplers and applying a metallic mirror on the buried silicon dioxide layer, we are able to reflect this light back towards the coupling structure where it can add constructively to the already coupled portion of the light. An efficiency improvement of roughly a factor 2 has been demonstrated for both 1D and 2D grating couplers, corresponding to similar structures in literature fabricated, but our fabrication process is more simple.

7.2 Perspectives

Since the biosensor experiment in this work was a proof-of-principle, there is some room for improvement. First and foremost, the biosensor should be characterised using appropriate surface chemistry with low-concentration analytes. Only then can the complete potential of the proposed flow scheme be characterised. In future versions of the chip holder, a temperature sensor should be implemented so as to allow for a temperature feedback loop to compensate thermal drift that can interfere with the bio-measurements. From a design point-of-view, it should be investigated whether mechanically more robust photonic structures can be used as biosensors. Finally, the pump parameters used to transport the droplet in this work are the result of a short optimisation process and could be further improved.

In future generations of the improved efficiency grating couplers, the top silicon nitride should be removed to eliminate the extra induced losses. Although we have now used gold for the metallic mirror, the possibility of using a Distributed Bragg Reflector mirror should be investigated to ensure better process compatibility.

As for the novel sensing method that is proposed using the angular spectrum of photonic crystals, it should be interesting to find out if it is in practice feasible to employ such a sensing scheme.

Although the fabrication process proposed in this work is already the result of laborious optimisation, there is also here still room for improvement. Apart from the fine-tuning of several parameters, some more general changes to the process could greatly enhance yield and overall quality. Perhaps the most drastic change would be trading the wet KOH etch process for a dry etch process: not only is a dry etch process in general more easy to control but in our specific case, it would allow for much higher membrane density on a single chip. However, if wet etching is preferred, the key problem to be tackled is hard mask quality: introduction of Low-Pressure Chemical Vapour Deposited silicon nitride would make an extra protection layer (e.g. ProTEK®) obsolete and could decrease the amount of undercut, leading to better process control. Finally, an improvement of the alignment accuracy of the contact lithography tool would allow for a more closed design cycle where numerical calculations can be more accurately matched to measurements, e.g. in the case of pressure sensors, in order to eventually increase the performance of all three proposed devices.

Silicon membrane fabrication process flow

This Appendix gives a step-by-step process flow with all relevant parameters to create silicon membranes in our clean rooms, starting from a thinned Silicon-on-Insulator (SOI) die. For more information and in-depth explanations, we refer to Chapter 3. Note that many of these parameters are not the result of thorough optimisation but are simply chosen because of prior experiences in the group or information from data sheets.

- Rinse the die in acetone, isopropyl alcohol (IPA) and deionised (DI) water.
- Clean the die for 10 minutes in Piranha solution (3 parts H_2SO_4, 1 part H_2O_2). Rinse with DI water and dry sample using nitrogen gun.
- In case no top silicon dioxide is present, deposit 400 nm pressure-enhanced chemical vapour deposited (PECVD) silicon dioxide on top of the die.
- Prepare a KOH solution of 40 ml using 26 g of KOH pellets and heat up to 79°C. Dip the die in the solution for 1 minute. Rinse with DI water and dry sample using nitrogen gun.
- Deposit 400 nm PECVD silicon dioxide on the bottom side of the die and 400 nm PECVD silicon nitride on both sides.

- Spincoat AZ5214E for 40 s at 2000 rpm. Bake for 3 minutes at 100°C. Spincoat another layer with the same parameters. *Other, thicker photoresist could be used which could only require one layer to be spincoated.* Edge beads should be removed manually to prevent problems using the vacuum mode of the mask aligner further on.
- Use backside alignment in the contact lithography mask aligner and illuminate for 26 s.
- Bake the die for 2 minutes at 120°C.
- Perform flood exposure on the die for 80 s.
- Develop the die in AZ400 developer for 30 s. Dilution should be 1 part AZ400 and 3 parts DI water.
- Protect the top side of the die by applying a coating of AZ5214E and baking it for approx. 5 minutes at 100°C.
- In case edge beads were removed in prior steps, apply some resist to cover the corners once more using AZ5214E and bake for approx. 5 minutes at 100°C.
- Load the sample in the reactive ion etcher (RIE) and etch for 12 minutes using the standard silicon dioxide etch recipe in our tool.
- Remove resist using acetone, IPA and DI water.
- Clean the die for 10 minutes in Piranha solution (3 parts H_2SO_4, 1 part H_2O_2). Rinse with DI water and dry sample using nitrogen gun.
- Spincoat ProTEK® B3 Primer for 1 minute at 1500 rpm on the top of the die. Bake for 1 minute at 205°C.
- Spincoat ProTEK® B3 for 1 minute at 1500 rpm on the top of the die. Bake for 2 minutes at 120°C and subsequently 1 minute at 205 degree
- Add 25 g of KOH pellets to 100 ml DI water, stir and heat up to 79°C. Immerse the die in the solution for approximately 3 hours. *A quick way to determine whether the substrate has been fully etched is removing the die from the solution, rinsing it shortly with DI water and holding it against a light source. If the substrate is etched, small light spots will be visible on the die.*
- When etching is complete, rinse the die using DI water and dry carefully using either a nitrogen gun (blow the nitrogen over the die under a slanted angle) or a hot plate

- Leave the sample for one hour in ProTEK® Remover. Cover the back of the sample with a blank silicon wafer so the ProTEK® can not redeposit in the substrate holes

- Clean the die for 10 minutes in Piranha solution (3 parts H_2SO_4, 1 part H_2O_2). Rinse with DI water and dry sample using nitrogen gun.

- **Liquid HF**
  Set a hot plate to 120°C. Apply some purple Logitech thin film bonding wax from to a silicon carrier wafer on the plate. Bond the top side of the die to the wax area and let cool. Put the bonded die in 49% HF for about 4 minutes. Rinse thoroughly. Put a petridish of Ecoclear Debonding Fluid on the hot plate and place the die in the petridish. Wait until the die has debonded and rinse with acetone, IPA and DI water. To remove all organic residues, clean the die for 10 minutes in Piranha solution (3 parts H_2SO_4, 1 part H_2O_2). Rinse with DI water and dry sample using nitrogen gun.

- **Vapour HF**
  Put the die on the electromechanical holder. Set the temperature to 40°C and enable chucking. Once the temperature is reached, allow the HF to enter the reservoir and put the die holder over it for 30 to 60 minutes, depending on the top silicon dioxide thickness. 800 nm and 1900 nm correspond to 30 and 60 minutes respectively.
  Leave the die on a hot plate at 200°C for 15 minutes, until the residue is visibly gone.